Lehigh University
Lehigh Preserve

Theses and Dissertations

2018

Understanding DPF failure, Improving DPF maintenance technologies, and advancing particulate filter materials

Kun Yang
Lehigh University

Follow this and additional works at: https://preserve.lehigh.edu/etd

 Part of the Civil and Environmental Engineering Commons

Recommended Citation
Yang, Kun, "Understanding DPF failure, Improving DPF maintenance technologies, and advancing particulate filter materials" (2018). *Theses and Dissertations*. 4261.
https://preserve.lehigh.edu/etd/4261

This Dissertation is brought to you for free and open access by Lehigh Preserve. It has been accepted for inclusion in Theses and Dissertations by an authorized administrator of Lehigh Preserve. For more information, please contact preserve@lehigh.edu.

www.manaraa.com

Understanding DPF failure, Improving DPF maintenance technologies, and advancing particulate filter materials

by

Kun Yang

A Dissertation

Presented to the Graduate and Research Committee

of Lehigh University

in Candidacy for the Degree of

Doctor of Philosophy

in

Environmental Engineering

Lehigh University

May 2018

www.manaraa.com

© (2018) Copyright
(Kun Yang)

www.manaraa.com

Approved and recommended for acceptance as a dissertation in partial fulfillment of the requirements for the degree of Doctor of Philosophy

Kun Yang

Understanding DPF failure, Improving DPF maintenance technologies, and advancing particulate filter materials

3/29/2018

Defense Date

Dissertation Director
Dr. John T. Fox

Approved Date

Committee Members:

Dr. Derick G. Brown

Dr. Arup SenGupta

Dr. Kristen Jellison

Dr. Richard Vinci

www.manaraa.com

ACKNOWLEDGMENTS

The completion of this work could not be done without the support and mentoring from several people which I have been so blessed with over the past five years. First and most important, I would like to thank my research advisor, Dr. John T. Fox not only for his advices in my Ph.D dissertation, but also for his personality, intergrity altitude towards science. It has molded my professional development as a scientist, and as a person. During this past five years, we worked together inside the lab and outside the lab as friends and brothers. Without the many rich scientific discussions with him, I could not accomplish my Ph.D dissertation as herein. I would also like to thank all of the members in my Ph.D committee, Dr. Arup Sengupta, Dr. Derick Brown, Dr. Kristen Jellison and my external committee member Dr. Richard Vinci, whose humors personality impressed me a lot. All of my committee members provide insightful conversations and helpful suggestions on my courses and researches over the past five years. Besides, I would also like to mention Robert Hunsicker, founder of Hunsicker Emission Services, LLC. During the past five years, we have built up a strong relationship throughout the cooperation and he gives me numerous of useful guidance on my research project and in the field I am not familiar.

I also want to express my thanks to my parents, for their love and strongly support

www.manaraa.com

when I am study. I would like thankful to my friends, including those I have met in Lehigh. PhD study is a long term and sometimes boring period, especially for our international students, I spend a wonderful five years in Lehigh because of those friends.

Most importantly, I would like to thank my wife, Yanxin Lu, for everything she has done during the past 3 and half years. The way she understands me, tolerant me and support my academic career during this period. Her encourage push me forward and give me hope during my Ph.D study and future life. I am forever in debt. Thank you so much for always being there.

www.manaraa.com

TABLE OF CONTENTS

www.manaraa.com

LIST OF TABLES

www.manaraa.com

www.manaraa.com

LIST OF FIGURES

www.manaraa.com

www.manaraa.com

www.manaraa.com

www.manaraa.com

www.manaraa.com

www.manaraa.com

www.manaraa.com

Abstract

The dissertation mainly focused on the process development of Diesel emission after treatment system and these substrate materials including cordierite and silicon carbide. As mobile sources, including highway and non-road vehicles combined to be the second leading anthropogenic source of particulate matter (Both $PM_{2.5}$ and PM_{10}) in the US, the on road and off road vehicles have required to equipped diesel particulate filter (DPF) and diesel oxidation catalyst (DOC) in order to meet the ever more stringent environmental regulations. DPF are made from artificial ceramics, especially cordierite which accounts for over 90% of the market in US. However, the DPF premature failures have been observed and reported widely. And the currently DPF regeneration technologies suffer thermal damage due to excessive temperature peaks, which occur due to exothermic combustion of soot embedded in DPF. Thus, the focus of the work herein focuses on understanding fundamental science relate to DPF premature failure, developing novel regeneration technology to protect the DPF and material technology to advance the use of DPF.

The fundamentally understanding of DPF premature failure has been demonstrated with first appraise and classified the DPF premature by monitoring the

www.manaraa.com

exhausted DPF provided by Hunsicker Emission Services, LLC, Earlington, PA. The surface elemental analysis of these premature failure area has been conducted by XPS, SEM-EDS. Results indicated an extraordinary high concentration of Na, K, Zn, Ca and Fe around the area of premature failures. XRD analysis of the failed DPF section indicated complex crystalline phases which are different from the intact cordierite crystalline phase. In order to further understanding the failure mechanism, lab scale tests have been carried out to simulate the DPF premature failure process happened during the commercial use. Results indicated the alkaline metals Na, K in the ash compositions contribute most towards the premature failures, followed by Fe. Despite the concentrations in the DPF ash, the Ca and Zn are not the leading contaminants cause the vitrification of the substrate, further leading to the cracking failure. The corrosion pathway has been revealed through the temperature elevated tests and the corrosion mechanisms were demonstrated by XRD analysis.

In order to prolong the lifetime of DPF, a novel water based regeneration process has been developed. This water based regeneration process demonstrated significant higher regeneration efficiency by removing several times more soot and ash, reducing 50% more engine back pressure than the conventional calcination process. And this water based regeneration process can not only remove carbon soot, but also remove majority metallic

www.manaraa.com

ash embedded in the DPF channel. Long term observation by Hunsicker Emission Services (HES) give a good consistence on the wash process for both high and low soot, ash loading DPF.

Further, a highly purity silicon carbide nanowire matrix (SCNW) has been manufactured by environmental friendly precursors: guar gum and silicon powder. The SCNW has advantages of higher porosity, higher chemical resistance and low thermal expansion coefficient compared to cordierite. When using guar gum/silicon powder ratio of 10 to 3, the substrate gives the most SiC nanowires. Iron acted as catalyst by leading the growth of nanowire under temperature of 1400^{o}C. The nanowires generated with highly crystallized face center cubic structures followed by the growing direction of (112). And the nanowires have core/shell structures with SiC acted as core and covered by SiO_2. The nanowires have diameters around 40-60nm and could grow several micrometers in length. The Vicky hardness analysis indicated the SCNW matrix has much higher hardness 467 HV/kg compared to commercial cordierite substrate of 280 HV/kg. The SCNW matrix can be potential substrate materials for DPF and DOC in the future.

In addition, the highly porous carbon soot collected from the exhausted DPF could be employed to adsorb the heavy metals (Cu, Cr and Cd). The adsorption capacity of carbon soot was compared with a commercial activated carbon and results indicated much higher

www.manaraa.com

adsorption capacity due to the abundant of surface functional groups and larger surface area. The reuse of DPF soot can be a potential absorbent besides the widely used activated carbon.

www.manaraa.com

Chapter 1

General introduction

In recent years, mobile sources, namely highway and non-road vehicles combined to be the second leading anthropogenic source of particulate matter for both $PM_{2.5}$ and PM_{10} in the Unite States (USEPA. 2013). And $PM_{2.5}$ and PM_{10} are the main cause of several illnesses including irritation of the airways, coughing, decreased lung function, aggravated asthma, irregular heartbeat, nonfatal heart attacks, and premature death for people with heart or lung disease (USEPA 2009 Final Report). In the US, exposure to PM is responsible for 27,000 heart attacks, 15,000 emergency room visits for asthma, and 2.4 million lost work days (Clean air task Force, 2004). California classified diesel PM as a toxic air contaminant since 1998, as health risk assessment studies indicated that about 70% of all airborne cancers are attributed to diesel particulate matters (CARB, 2015). One-year air quality data from an urban site in Finland determined that around 14% of $PM_{2.5}$ was carbon soot derived from heavy duty vehicles and more than 90% of the carbon soot can be classified as $PM_{2.5}$ (Viidanoja 2002). This $PM_{2.5}$ pollution is more severe in other countries, for example China, which has high usage of coal and high density of vehicle use in urban areas (Street 2001).

www.manaraa.com

To compare, Diesel engines power railcars, trucks, and ships are account for 85% of the US Ton Miles of Freight (USDOT. 2017). Currently in the US, diesel engines are sued for a myriad of transportation and heavy equipment applications, due to efficiency and power output. There are over 24,000 Diesel Electric Locomotives (US International Trade Commission.2011), over 2,580,000 truck tractors (USDOT. 2012), over 1,500,000 Farm trucks (USDOT. 2012), over 5,800,000 diesel vans (USDOT. 2012) and other usage including numerous marine engines, non-road diesel engines require DPF equipment and replacement every 6 to 12 months without reclamation (USEPA. 2010). Overall, there are over 10 million medium duty and heavy-duty diesel engines that currently, or will eventually require DPFs. Since 2000, Europe and North American has legislated all the on-road diesel vehicles need to be equipped with a diesel particulate filter (DPF). Diesel particulate matter is formed from combustion of fuel and lubricating oil and results in ash and soot. Incomplete combustion of petrochemicals results in soot, which is the insoluble organic carbon component of particulate matter, and consists of agglomerates of various ranging from 0.5 to 5 μm (Liati A. 2013). Soot is typical large particle than ash. The soot is made of the resulting elemental carbon and highly polymerized organic compounds (Graskow B.R. 1998). There is also a minor component of soluble organic fraction (SOF) hydrocarbons with approximately 75% to 90% in the C_{14}-C_{27} alkane, and 3%-20% as

www.manaraa.com

aromatic hydrocarbons (Vojtisek-Lom. M., 2012). On the other hand, ash component is the inorganic noncombustible fraction, with typical size of 45-160 nm in diameter (Liati A. 2013). The ash is comprised of sulfates, phosphates, calcium, zinc, magnesium, and other metals- from additives in fuel and lubricating oils, etc (Liati A., 2012). Ash components are also consisted of trace iron, copper, chromium and aluminum which result from the corrosion of exhaust systems components prior to the DPF (Liati A., 2012). Due to the large surface area of carbon soot, it could adsorb numerous of ash particles on it to form a complex structure (Liati A. 2012). As required by EPA, via 40 CFR Parts 69, 80 and 86, medium and heavy-duty Diesel Engines and vehicles including non-road, locomotive, small cars and marine applications produced from the year of 2007 were required to meet PM emission standards of 0.01 grams per brake horse power/hour (USEPA 2000). To meet these rigid environmental standards, on road diesel engine exhaust systems require to equipped with diesel particulate filters (DPFs) and diesel oxidation catalyst (DOCs). According to EPA and CARB, Typical DPF can reduce more than 85-90% of particulate matter emission from diesel engines (USEPA. 2000, Cooper 1990, Kawamura 1997). And DPF coated with catalysts are effective to reduce hydrocarbon and CO emissions by more than 70% (Dettling J.C. 1992, Gorsmann C. 2005).

www.manaraa.com

DPF are designed to be different structures, among those designs, wall-flow Monoliths are the most common structure. Wall-flow Monolithic diesel filters consist of many small parallel channels, typically of square cross-section, running axially through the part. The most important parameter characterized a DPF is the porosity. The wall-flow monoliths have a distribution of fine pores with typical porosity between 45-50% or higher and the pore sizes range from 10 to 20 μm (Miwa S. 2001, adler J. 2005, Itoh A. 1993, Fukushima M. 2006, Ohno K. 2000, Eom J.H. 2013, Dey A. 2013). The cordierite substrate used in our study have a pore size distribution around 40%. There are other types of DPF including foam structure, ceramic fiber cartridge. In year of 1999, the world first DPF manufactured by SiC fiber has been developed by ISUZU, this is a nonwoven fabric made of silicon carbide ceramic fiber and formed cylindrical shape and hold by two metal wire cloths. This fiber DPF has advantages of higher soot and PM reduction efficiency, longer durability and lower material density (Sakaguchi 1999). Wall flow DPFs remove PM by forcing exhaust through porous walls separating adjacent channels in a monolithic substrate. DPFs are manufactured from artificial ceramics including cordierite, silicon carbide, aluminum titanate and mullite. Among these ceramics, cordierite is more commonly used which possesses a chemical composition of $2MgO\text{-}2Al_2O_3\text{-}5SiO_2$ (Yang K. 2016). After 6 or 12 months operation, the accumulation of soot and ash in the filter

www.manaraa.com

induces back pressure on the diesel engine, which can cause diesel vehicles to consume more fuel, lower power output, effect engine durability and under worse cause scenarios render the engine/vehicle un-operable (Yang K. 2016). For that reason, DPF are required to be temporarily removed from the vehicles, normally 6 to 12 months, at prescribed maintenance intervals, to clean out the accumulated ash and relieve engine back pressure (USEPA. 2010). Soot particulate matter is removed from DPFs via passive regeneration which stands for increasing exhaust temperature to burn out the soot, or when active on-board regeneration occurs with additional heat via injecting extra fuel into engine in order to improving its horsepower. However, the on-board regeneration cannot remove inorganic ash component of the particulate matter from the DPF. The ash cannot be removed unless the DPF is removed from the vehicle for cleaning as recommended per the engine manufacturer prescribed maintenance program. The author's study can be classified in three different aspects: fundamentally understanding the thermal and chemical conditions induce the premature failure; DPF cleaning technology; and advancing silicon carbide nanowire technology.

1.1 DPF premature failure-the cause and effect

DPFs were designed to last long time, especially for 800,000 miles. However, during the commercial application, the DPFs have been observed to fail early, by pinholing, cracking

www.manaraa.com

and melting failures, which compromising PM reduction efficiency (Yang K. 2016). There are three temperature profiles a DPF would experience. Engine exhausted gas has temperature around 200 to 300ºC, the temperature needed for 'passive' and 'active' regeneration ranges from 200-400ºC and 550-600ºC, respectively (Donaldson). Since the soot burning is an exothermic reaction, some area of the DPF could reach temperatures higher than 1200ºC, which is close to the cordierite melting point of 1470ºC (Perry D.L. 1995). Pinholes, melts, and cracks have been found within cordierite and silicon carbide substrate materials after exposure to uncontrolled regeneration conditions. While previous laboratory controlled studies have confirmed the corrosive impact of ash on DPFs, the underlying mechanisms responsible for DPF failure and the interaction between ash/substrate is not well understood. The DPF premature failure theory has been successfully modeled using catastrophe theory and diffeomorphism transformation considering flow resistance due to ash deposition (Zhang B. 2016). However, this model does not identify the specific failure mechanisms. Several hypotheses exist to explain DPF substrate failure, including that the interaction between substrate materials and alkali compounds significantly reduce the substrate melting point (Dario M.T. 1998, Maier N. 2010, Choi B. 2009). Recent findings provide information on ash compositions collected from DPF. The primary ash constituents included CaO (29-35 wt%), sulfate (35-39 wt%),

www.manaraa.com

MgO (5-11 wt%), phosphate (13-16 wt%) and ZnO (5-10 wt%), with a trace of Fe_2O_3 (<1 wt%) (Quigley M. 2002). With respect to specific compounds, interaction between substrate materials and alkali compounds in the presence of additional ash materials, including Ca, Mg, and Zn in phosphate sulfate oxide forms, was observed to act more aggressively on the substrate materials than the alkali metals alone (Maier N. 2010, Choi B. 2009). Some scenarios demonstrated that iron oxide tends to promote greater reaction between cordierite filter materials as well (Montanaro L. 1994). And further interactions between metal ash components and cordierite materials can induce transformation of the cordierite crystallinity and degrade the substrate structure. For example, sodium rich ash catalyzed melting of the cordierite substrate material at temperatures as low as 830°C (Maier N. 2010). Na_2CO_3 forms several crystalline phases that differ to cordierite after only 5min exposure under 1000°C (Montanaro L. 1994). Fe and Zn ash components interact with cordierite substrate at temperature well above 1000°C (Pomeroy M.J. 2012). The interaction between metal oxide and cordierite induces vitrification, the glass-like phases include high carnegieite, low carnegieite and nepheline at temperature range from 700-1000°C. Merkel demonstrates metal ash components can affect the microstructure of cordierite materials by sintering and eutectic reactions (Merkel G. 2001). Since the glass-like phases have different thermal expansion coefficient based on dilatometric tests, it

www.manaraa.com

might lead to the microcracks (Montanaro L. 1994). The reaction pathway follows staining, pitting, surface sintering, liquefaction, pinholes and bulk melting with increased temperature and time.

Based on the previous researches, the author conducts researches in order to reveal the underlying mechanism caused the DPF premature failures. The research hypothesis herein is states: During the high temperatures of on-board regeneration, chemical components of ash and soot can react with substrate materials, melting the substrate, cause premature failures. To investigate this hypothesis, we investigated the thermal and chemical conditions that occurs within a DPF during use and during on-board regeneration so as to understand premature failure of DPFs used for medium and heavy-duty diesel engines. Specifically, our researches seek to (1) fundamentally understanding the chemistry of the soot and ash captured within the DPF (2) understanding the thermal and chemical conditions leading to the DPF premature failures. (3) demonstrating a possible relationship between migration of individual ash components and the transformation of cordierite morphology and crystallinity.

1.2 Conventional DPF reclamation process

Soot and ash accumulated on DPF need to be removed to release the engine back pressure every 6-12 months. Conventional DPF reclamation process is based on pneumatic

www.manaraa.com

air/compressed air cleaning to remove the embedded ash and soot particle, followed by calcine the DPF under temperature range of 600-900ºC. Numerous of patents have been filed including the reclamation process and apparatus. International Truck Intellectial Property Company (2010) has patented a DPF cleaning method simply by transferring a pressure wave into the DPF to blow out the ash particulate from the filter (Ehlers M.S. 2010). General Motor Corporation (2007) developed a microwave regeneration process, especially generating heat by microwave to burn out the soot. The problem relate to this method is that the microwave may break the ceramic substrate and the heat cannot remove metallic ash embedded (Gregoire D.L. 2007). Currently the most widely used method is compressed air plus calcination, which the equipment is provided by FSX company. Our industrial cooperator, Hunsicker Emission Service, LLC has purchased several FSX equipment and find out the method can be potential harmful to the DPF, especially causing premature failures including melting, pinholing and cracking on the DPF.

There are some companies have already started to use wet washing process to clean the DPF. Corning (2008) patented one method use organic acid and inorganic acid (nitric acid or sulfuric acid) at pH=1 to wash the DPF by no more than 10mins. This could remove 50% or more metallic ash embedded in the DPF, however, the DPF still need to be blow first by compressed air with 300ft^3/min in order to remove soot (Bardhan P. 2008).

www.manaraa.com

Carlson Gaskey & Oil also filed a patent with back wash the DPF with tap water (Crawley W.H. 2005). And others use tap water mixed with commercial detergent to backwash the DPF at temperature around 60ºC (Miebach R. 2005). Delaware Capital Formation, lnc developed an ultrasonic filter regeneration apparatus to remove the blocked soot cake and ash embedded in the DPF (Davis S.J. 2001). Subramanian (2010) made applied of chelating agent ethylenediamine disuccinic acid to regeneration the three-way automobile catalysts (Subramanian B. 2010), while Lambrou (2005) use weak organic acids to reactivation the three-way catalysts and to remove various contaminants (P, Fe, Zn, Cr, Pb, Ni, and Cu) accumulated on the catalyst (Lambrou P.S. 2005). None of those methods provides an optimized way to remove both carbon soot and metallic ash at the same time. And the potential affection on Pd/Pt catalysts was not aware. As some of the patents use strong acid, low pH solution which might attack the catalyst coating. The author cooperates with Hunsicker Emission Service to successfully developed a water based cleaning process that can remove both carbon soot and metallic ash. And during our tests with industrial cooperator, this method has least affection on the coated catalyst. Till now, this method has been used for over two years, cleaning hundreds of exhausted DPF, DOC and SCR.

1.3 DPF substrate-Silicon carbide nanowire matrix (SCNW)

www.manaraa.com

DPFs are commonly produced from cordierite and from silicon carbide. Cordierite is the preferred material as it is easing to manufacture, low thermal expansion, and low cost. However, these cordierite DPFs have been observed to fail pre-maturely during vehicle use; In particular, when cordierite is exposed to ash components (alkalis and metals) at high temperatures, DPFs have been observed to fail via pinholing, cracking, and melting – compromising PM reduction efficacy and requiring DPF replacement (CARB 2015, Yang K. 2016).

Due to the early failure of common cordierite DPFs, silicon carbide offers promise as SiC provides advantages of having a higher melting point, more favorable thermal conductivity, and is more chemically resistant to ash components at high temperatures (Adler J. 2005, Itoh A. 1993, Fukushima M. 2006). Besides, SiC offers more chemical resistance to ash components than common cordierite DPFs, as this would result in more robust DPFs. Porous SiC is an excellent candidate for numerous materials, including high temperature air filtration, catalytic supports, separation membranes, acoustic and thermal insulators, high temperature structural materials, kiln equipment, thermoelectric energy conversion, water filtration, metallurgy, and electrical engineering (Eom J.H. 2013). Porous SiC ceramics are promising filtering media to control PM, but current SiC DPFs are more difficult, more expensive, and more energy intensive to manufacture than

www.manaraa.com

common cordierite (Adler J. 2005, Itoh A. 1993, Fukushim M. 2006, Eom J.H. 2013, Dey A. 2013). Especially the manufacture requires temperatures exceeding 2100-2200^{o}C, and yields porosity less than 40% (Adler J. 2005, Itoh A. 1993, Fukushim M. 2006, Eom J.H. 2013, Dey A.2013). Besides, manufactured silicon carbide DPFs are limited in shapability and size, which require preformed modules to be cemented together (Adler J. 2005, Fukushima M. 2006, Dey A. 2013, Pomeroy M.J. 2012, Warren Y.D. 2002, Fredrich W.T. 2010, Guo W.M. 2012, Ohgushi S.T. 1999, Zhu 2007, Agrafiotis C.C. 2007). The high energy SiC covalent bond results in the sintering of SiC ceramics requires very high temperatures, usually above 2000^{o}C, which limit the shaping and forming, compared to cordierite. As a result, conventional manufacturing of SiC takes a second leading place in the DPF market (Williams J.L. 2001). Therefore, lowering the processing temperature to form porous SiC is a critical technological advancement which would further SiC material use in porous applications. In addition, compared to cordierite, the SiC has average density of 3.1-3.2g/cm^3, higher than the cordierite, which has material density of 2.1g/cm^3. The higher density actually increases the cost to manufacture SiC DPFs because it requires more material to produce, which further deters the use of SiC (Adler J. 2005). The porosity and mean pore size of recrystallized SiC is also substantially lower than cordierite (Miwa S. 2001), as silicon carbide yields porosity less than 40% (Miwa S. 2001, Adler J. 2005,

www.manaraa.com

Itoh A. 1993, Fukushim M. 2006, Ohno 2000, Eom J.H 2013). Compared to SiC, the cordierite has higher thermal shock resistance due to higher porosity, which can stand sudden thermal condition changes (Williams J.L. 2001). In addition to lowered porosity hindering overall filtration capacity, this low porosity also lowers thermal shock resistance.

If silicon carbide DPF disadvantages related to manufacturability and resultant porosity are overcome SiC materials would be more thermally stable and chemically robust at high temperatures, as compared to common cordierite. Sakaguchi (1999) has first started to make application of SCNW in the field of DPF by fabricate the nonwoven SCNW into cylindrical shape. The DPF has robust filtration efficiency and thermal resistance compared to monolith DPF (Sakaguchi T. 1999).

Herein, the author provided an environmental friendly way to manufacture the silicon carbide nanowire matrix from solid precursors. The SCNW matrix has greater porosity, improved thermal resistance, enhanced filtration capacity towards the manufacture of SiC substrate. The SCNW matrix manufactured in lab has extraordinary mechanical strength and high porosity, which could facilitate its further use in filtration.

1.1 Hypothesis

www.manaraa.com

There are three general hypotheses relate to this work, based on the maintenance, material innovation of DPF which could improve the diesel after treatment system lifetime and developing more robust DPF. More specifically, the underlying hypotheses for this work are:

(1) The DPF metallic ash components can react with cordierite substrate and lower its melting point, results in the DPF premature failures.

(2) A water based chemicals could remove significantly more DPF carbon soot and metallic ash than conventional DPF cleaning process, lowing the engine back pressure.

(3) Manufacture a SCNW matrix which has much higher porosity and mechanical strength by environmental friendly organic precursor can be a potential robust material for DPF substrate.

1.2 Scope of work

This dissertation contains seven chapters and all the seven chapters are linked together by one core topic-DPF. **Chapter 1,** is the general introduction; **Chapter 2,** focused on the commercial observation and classification of DPF premature failure. During the work with Hunsicker Emission Service, LLC. We found out the DPF can happen premature failure and there is closely relationship between premature failure and DPF

www.manaraa.com

ash. This works has already been published in the Emission Control Science and Technology, which has been approved for use herein. Kun Yang is the first author, John Fox is the corresponding author and Robert Hunsicker is the co-author. **Chapter 3,** fundamentally understanding the thermal and chemical conditions that lead to premature failure via lab scale simulation test. The works has been published on two journals, one is on Journal of Materials Science, other one is Journal of Porous Materials. Both these two papers, Kun Yang is the first author, John Fox is the corresponding author and Robert Hunsicker is the co-author. **Chapter 4,** developing water based DPF cleaning process and demonstrate the process in both lab scale and industrial scale by cooperate with Hunsicker Emission Service (HES). The data has been approved by Hunsicker Emission Service, LLC. **Chapter 5,** focuses on in-situ grow of functional SCNW matrix through organic precursor, detailing manufacture methods and initial results. The work will be submitted to Materials and Design for peer review. Kun Yang is the first author, and John Fox is the corresponding author. **Chapter 6,** is focused on the waste reclamation process, reclamation the DPF soot and reuse it as high-quality sorbent which has extraordinary heavy metal adsorption ability. **Chapter 7** summarized this dissertation and provide some future thinking.

1.3 References

www.manaraa.com

Agrafiotis C.C., Mavroidis, I., Konstandopoulos, A., Hoffschmidt, B., Stobbe, P., Romero, M., (2007). "Evaluation of porous silicon carbide monolithic honeycombs as volumetric receivers/collectors of concentrated solar radiation." Solar energy materials and solar cells, 91:474-484.

Adler J. (2005). "Ceramic diesel particulate filters." International applied ceramic technology, 2(6): 429-439.

Bardhan P., Mian WG., Angele JJS., Stevens A. (2008). "Method and system for removing ash from a filter." US Patent, No.: US 2008/0083334 A1.

Crawley W.H. (2005). "Method and system for flushing ash from a diesel particulate filter." US Patent, No.: 2005/0011357.

Choi B., Jeong J.W. (2009). "Effects of hydrothermal aging on SiC-DPF with metal oxide ash and alkali metals." Journal of Industrial Engineering Chemistry, 15: 707-715.

Clean Air Task Force, C. Schneider, Editor, (2004). *Diesel Emissions: Particulate Matter-Related Health Damages*, 2004, Bethesda, MD.

California Air Resource Board, (2015). "Evaluation of Particulate Matter Filters in On-Road Heavy-Duty Diesel Vehicle Applications".
http://www.arb.ca.gov/msprog/onrdiesel/documents/DPFEval.pdf

Dario M.T., A, B. (1998). "Interaction of some pollutant oxides on durability of silicon carbide as a material for diesel vehicle filters." Journal of materials science. 33(1): 139-145.

Donaldson. Engine horsepower and exhaust flow guide. Donaldson, 2-8.

www.manaraa.com

Dey A., Kayal N., Chakrabarti O., Caldato R., Andre C., Innocentini D. (2013). "Permeability and nanoparticle filtration assessment of cordierite bonded porous SiC ceramics." Industrial and Engineering chemistry research, 52: 18362-18372.

Davis S.J., Hausermann D.M. (2001). "Ultrasonic filter regenerating appratatus and method." US Patent: US 6251294 B1.

Dai H.J., Wong, E., Lu, Y., Fan, S., Lieber, C., (1995). "Synthesis and characterization of carbide nanorods." Nature, 375: 769-772.

Du X.W., Zhao, X., Jia., S.L., Zhao, N.Q., (2007). "Direct synthesis of SiC nanowires by multiple reaction VS growth." Materials Science and Engineering: B, 136(1): 72-77.

Eom J.H., Kim Y.W., Raju S. (2013). "Processing and properties of microporous silicon carbide ceramics： a review." Journal of Asian ceramic societies. 1: 220-242.

Ehlers M.S. (2010). "Diesel particulate filter (DPF) in chassis cleaning method." US Patent: US7716922 B2.

Fukushima M., Zhou Y., Yoshizawa Y., Hirao K. (2006). "Preparation of mesoporous silicon carbide from nano-sized SiC particle and polycarbosilane." Journal of the ceramic society of japan, 114(6): 571-574.

Fredrich W.T., Wolff, T., Johannesen, L., Hajireza, S., (2010). "A new approach to design high porosity silicon carbide substrates." SAE International, 2010-01-0539.

www.manaraa.com

Graskow B.R., Kittelson D.B., Abdul-khalek I.S., Ahmadi M.R., Morris J.E. (1998). "Characterization of exhaust particulate emissions from a spark ignition engine." Fuel, 11-05.

Guigley M. and Seguelong T. (2002). "Series application of a diesel particulate filter with a Ceria-based fuel borne catalyst: preliminary conclusions after one year of service." SAE International, 2002-01-0436.

Gregoire D.J., Colbura J.S. (2007). "Diesel particulate filter using microwave regeneration." US Patent, No.: US7303602 B2.

Gundiah G., Madhav, G.V., Govindaraj, A., Seikh, M.M., Rao, C.N.R., (2002). "Synthesis and characterization of silicon carbide, silicon oxynitride and silicon nitride nanowires," Journal of material chemistry, 12: 1606-1611.

Guo W.M., Xiao, H., Xie, W., Hu, J., Li, Q., Goa, P., (2012). "A new design for preparation of high performance recrystallized silicon carbide." Ceramic International, 38: 2475-2481.

Ho G.W., Wong, A., Kang, D., Welland, M.E., (2004). "Three dimensional crystalline SiC nanowire flowers." Nanotechnology, 15: 996-999.

Hu J.Q., Lu., Q., Tang, K., Deng, B., Jiang, R.R., Qian, Y.T., Yu, W.C., Zhou, G.E., Liu, X.M., Wu, J.X., (2000). "Synthesis and characterization of SiC nanowires through a reduction carburization route." Journal of Physical chemistry B, 104:5251-5254.

Itoh A., Shimato K., Komori T., Okazoe H., Yamada T., Nimura K., Watanabe Y. (1993). "Study of SiC application to diesel particulate filter (part 1): material development." SAE International, 930360.

www.manaraa.com

Kang B.C., Lee S.B., Boo J.H. (2004). “Growth of SiC nanowires on Si(100) substrates by MOCVD using nickel as a catalyst.” Thin solid films, 464-465: 215-219.

Ko F., Gogotsi, Y., Ali, A., Naguib, N., Ye, H., Yang, G.L, Li, C., Willis, P., (2003). “Electrospinning of continuous carbon nanotube filled nanofiber yarns.” Advanced materials, 15(14): 1161-1165.

Liati A., et al. (2013). “Metal particle emissions in the exhaust stream of diesel engines: an electron microscope study.” Environmental Science and Technology, 47(24): 14495-14501.

Lambrou P.S., Christou S.Y., Fotopoulos A.P., Foti F.K., Angelidis T.N., Efstathiou A.M. (2005). “The effect of the use of weak organic acids on the improvement of oxygen storage and release properties of aged commercial three way catalysts,” applied catalysis, 59: 1-11.

Lee S.T., Wang N., Lee C.S. (2000). “Semiconductor nanowires: synthesis, structure and properties.” Materials Science and Engineering: A, 286(1): 16-23.

Miwa S., Abe, F., Hamanaka, T., Yamada, T., Miyairi, Y., (2001) “Diesel particulate Filters made of newly developed SiC”. SAE International. 2001-01-0192

Miebach R. (2005). “Method for cleaning a particular filter.” US Patent, No.: US6926760 B2.

Merkel G., Warren W.C. (2001). “Thermal durability of wall flow ceramic diesel particulate filters.” SAE International, 2001-01-0190.

Montanaro L. (1994). “Influence of some pollutants on the durability of cordierite filters for filter diesel cars.” Ceramic International, 20(3): 169-174.

www.manaraa.com

Maier N., et al. (2010). “Mechanisms and orientation dependence of the corrosion of single crystal cordierite by model diesel particulate ashes.” Journal of European Ceramic Society, 30(7): 1629-1640.

Ohgushi S.T., Sakaguchi, S., Suzuki, S., Kita, H., Ohsumi, K., Suzuki, T., Kawarmura, H., (1999). “Development of high durability diesel particulate filter by use SiC fiber.” SAE International, 1999-01-0463.

Perry D.L. (1995). Handbook of inorganic compounds. CRC press, Inc., New York, pp 234-235.

Pomeroy M.J., Sullivan O., Hampshire S., Murtagh M.J. (2012). “Degradation resistance of cordierite diesel particulate filters to diesel fuel ash deposits.” Journal of American ceramic society, 95(2): 746-752.

Pan Z.W., Lai, H., Au, F., Duan, X., Zhou, W., Shi, W., Wang, N., Lee, C., Wong, N., Lee, S., Xie, S., (2000). “Oriented silicon carbide nanowires: synthesis and field emission properties.” Advanced Materials, 12(16): 1186-1190.

Street D.G., Gupta S., Waldhoff S.T., ang M.Q., Bond T.C., Bo Y.J. (2001). “Black carbon emissions in China.” Atmospheric environment, 35(25): 4281-4296.

Sakaguchi T., Ohgushi A., Suzuki S., Kit H., Ohsumi K., Suzuki T., Kawamura H. (1999). “Development of high durability diesel particulate filter by using SiC fiber.” SAE International, 1999-01-0463.

Subramanian B., Christou S.Y., Efstathiou A.M., Namboodiri V., Dionysiou D.D. (2011). “Regeneration of three way automobile catalysts using biodegradable metal chelating

www.manaraa.com

agent-S,S,-ethylenediamine disuccinic acid (S,S-EDDS).” Journal of hazardous materials, 186: 999-1006.

Sun X.H., Li, C., Wong, W., Wong, N., Lee, C., Lee, S., Teo, B., (2002). “Formation of Silicon carbide nanotubes and nanowires via reaction of silicon (from disproportionation of silicon monoxide) with carbon nanotubes.” Journal of American chemistry society, 124: 14464-14471.

Shi W.S., Zheng, Y., Peng, H., Wang, N., Lee, C.S., Lee, S.T., (2000). “Laser ablation synthesis and optical characterization of silicon carbide nanowires.” Journal of American ceramic society, 83(12): 3228-3230.

U.S. Department of Transportation. “National Transportation Statistics”. Table 1-49: U.S. Ton-Miles of Freight. http://www.rita.dot.gov/bts/sites/rita.dot.gov.bts/files/publications/national_transportation_statistics/index.html

U.S. Environmental Protection Agency. (2010) “Technical Bulletin: Diesel Particulate Filter General Information”. EPA-420-F-10-029, May 2010.

US International Trade Commission, (2011) “Rolling Stock: Locomotives and Rail Cars”, Industry and Trade Summary. Office of Industries Publication, ITS-08. March 2011.

U.S. Department of Transportation, Federal Highway Admistriation, Office of Highway Policy Information: Highway Statistics Series. “Highway Statistics 2012: Truck and Truck-Tractor Registrations – 2012, Table MV-9.”

U.S. Environmental Protection Agency. (2013) “National Emissions Inventory (NEI) Air Pollutant Emissions Trends Data and Estimation Procedures”. 1970 - 2013 Average annual emissions, all criteria pollutants in MS Excel - December 2013. http://www.epa.gov/ttnchie1/trends/

www.manaraa.com

U.S. EPA. (2009) Final Report: Integrated Science Assessment for Particulate Matter. U.S. Environmental Protection Agency, Washington, DC, EPA/600/R-08/139F, 2009.

USEPA (2000): heavy duty engine and vehicle standards and highway diesel fuel sulfur control requirements. EPA 420-F-00-057.

Vojtisek-Lom M., Czerwinski J., Lenicek J., Sekyra M., Topinka J. (2012). "Polycyclic aromatic hydrocarbons (PAHs) in exhaust emissions from diesel engines powdered by rapeseed oil methylester and heater nonesterified rapeseed oil." Atmospheric Environment, 60: 253-261.

Viidanoja J., Silampaa M., Laakia J., Kerminen V.M., Hillamo R., Armio P., Koskentalo T. (2002). "Organic and black carbon in PM 2.5 and PM10: 1 year of data from an urban site in Helsinki, Finland." Atmospheric Environment, 36(19): 3183-3193.

Williams J.L. (2001). "Monolith structures, materials, properties and uses." Catalysis Today, 69:3-9.

Warren Y.D., Gadkaree C., Johannesen L. (2002). "Silicon carbide for Diesel particulate filter applications: material development and thermal design." SAE International, 2002-01-0324.

Xi G.C., Peng, Y., Wan, S., Li, T., Yu, W., Qian, Y., (2004). "Lithium assisted synthesis and characterization of crystalline 3C-SiC nanobelts", Journal of physical chemistry B, 108(52): 20102-20104.

www.manaraa.com

Yang K., Fox J.T., Hunsicker R. (2016). “Characterizing diesel particulate filter failure during commercial fleet use due to pinholes, melting, cracking and fouling.” Emission Control Science and Technology, 2: 145-155.

Ye H.H., Titchenal, N., Gogotsi, Y., Ko, F., (2005). “SiC nanowires synthesized from electrospun nanofiber templates.” Advanced materials. 17: 1531-1535.

Zhang Y.J., Wang, N., Gao, S., He, R., Miao, S., Liu, J., Zhu, J., Zhang, X., (2002). “A simple method to synthesize nanowires.” Chemistry of materials, 14(8): 3564-3568.

Zhou W.M., Yang, B., Yang, Z.X., Zhang, Y.F., (2006). “Large scale synthesis and characterization of SiC nanowires by high frequency induction heating.” Applied surface science, 252: 5143-5148.

Zhang B., Gong J.K.E.J.Q., Li Y. (2016). “Failure recognition of the diesel particulate filter based on catastrophe theory.” Can. J. Chem. Eng., 94: 596-602.

www.manaraa.com

Chapter 2

Characterizing Diesel Particulate Filter failure during commercial fleet use due to pinholes, melting, cracking and fouling

Abstract

In the previous chapter of introduction, the author demonstrates that Diesel Particulate Filters (DPFs) are essential particulate matter emission control devices, especially for the air pollution control. Some diesel particulate filters have been observed to fail during industrial-fleet vehicle use. DPFs that fail during vehicle use compromise particulate matter emission capture. Herein, failures in cordierite DPF substrates observed during Commercial Fleet use were characterized as, pinhole failure, melt failure, crack failure, and fouling failure. The observed failures were correlated to particulate matter chemical composition and physical changes in the cordierite substrate of the exhausted DPFs. The physical-chemical characteristics of pinhole failure, melt failure, crack failure, and fouling failure were determined by applying scanning electron microscopy-energy dispersive spectrometry (SEM-EDS), X-ray photoelectron spectroscopy (XPS) and X-ray diffraction (XRD). Results indicate that the chemical composition and crystalline structures of cordierite DPF substrate changed according to the failure characterization. The specific

www.manaraa.com

changes to the cordierite substrate during failure can contribute towards understanding fundamental DPF failure mechanisms.

2.1 Introduction

Diesel engine particulate matter (PM) is formed from combustion of fuel and lubricating oil, and results in ash and soot. Incomplete combustion of petrochemicals results in soot and ash, the soot typical has average particle size of 0.5-5 μm (Liati 2013). The inorganic ash component which are reportedly 45-160 nm in size.(Liati 2013).

The widely used materials to manufacture DPF are cordierite, silicon carbide, and aluminum titanate (Dario M.T., 1998). The exhausted DPF used in this study has a wall flow structure and made from cordierite. Wall-flow devices remove PM by forcing exhaust through porous walls separating adjacent channels in a monolithic substrate (Fino 2007, Maricq 2007). The substrate used herein for the experiment is a synthetic ceramic which possess a chemical composition of $2MgO\text{-}2Al_2O_3\text{-}5SiO_2$ (Maier 2010). DPF substrates made with each of these materials are characterized by very good filtration efficiency, with PM capture efficiency greater than 90% (Fino 2007, Maricq 2007). The DPF substrate is provided by Hunsicker Emission Service, LLC. These exhausted DPFs characterized are all collected from truck rental company, and truck dealers. However, the accumulation of

www.manaraa.com

soot and ash in the filter induces back-pressure on the diesel engine, which can cause diesel vehicles to consume more fuel, lower power output, effect engine durability, and under worse case scenarios render the engine/vehicle un-operable (Hardenberg 1979, Konstandopoulos 1989, Stamatelos 1997, Stratakis 2002, Aravelli 2007). As a result, the DPF should be remove to clean based on prescribed maintenance requirement.

Periodically regeneration of the DPF carried out by burning off the carbon soot embedded in the DPF. During this process, the incombustible ash remains in the DPF after regeneration and accumulates in the substrate channels and walls. (Aravelli 2007, Sappok 2009) The extra burning of the carbon soot release large amount of heat and DPF substrate may suffer the thermal damage.(Montanaro L. 1994, Dario M. T. 1998, Merkel G. 2001, Choi. B. 2009, Maier 2010). Hunsicker Emission Service, LLC observed pinholes, melts, and cracks within cordierite and silicon carbide substrate materials after exposure to uncontrolled regeneration conditions. Previous researchers have proposed several hypotheses to explain DPF substrate failure. Hunsicker Emission Service (HES) found out the premature failure happened at temperature lower than the cordierite substrate melting point. Some researchers pointed out the interaction between substrate materials and alkali compounds significantly reduced the melting point of the cordierite and silicon carbide,

www.manaraa.com

with average melt temperatures lowered to about 700-900ºC (Montanaro L. 1994, Dario M. T. 1998, Choi. B. 2009, Maier 2010)

Within those DPF ash chemical compositions, the interaction between sodium, potassium and substrate could cause the most severe damage to the substrate (Montanaro L. 1994, Dario M. T. 1998). Other researchers found out the presence of Ca, Mg and Zn in phosphate-sulfate-oxide forms could accelerate the alkali corrosion (Merkel G. 2001, Choi. B. 2009).

Failures of DPFs are most often attributed to single upstream engine component problems or failures, such as EGR failures or turbo failures, which results in Na, K contaminants on DPF (CARB 2015). As DPFs have now been in commercial use for several years, field observations suggest that aging and non-event linked DPF failures occur. In this chapter, the authors aim to: (1) classify four modes of DPF failure observed during commercial fleet use, and (2) seek to characterize the ash and cordierite substrate physical-chemical properties associated with DPF failure. Due to the complexity in fuel, lubricating oil, and engine operating conditions, consistent DPF failure mechanisms are difficult to ascertain. To date there is limited evidence from operational DPF failures which correlate the mechanics and PM chemistry to mode of failure. However, research to date appears to concur that alkaline ash components may harm DPF substrates via various

www.manaraa.com

pathways that are still under investigation. To investigate these issues, the authors analyzed ash chemistry in cordierite DPF substrates and simultaneously characterized DPF failure mode. Specifically, post-mortem analysis of cordierite diesel particulate filters was performed. Ash composition was appraised via acid treatment of exhausted DPF samples and subsequently analyzed for inorganic components via ICP-OES, the result was compared with the data from SEM-EDS. SEM was applied to characterize the micro-structures of the different modes of DPF failures, and the corresponding elemental distributions were measured by EDS. XPS-AES was utilized to determine the surface chemical composition and the atomic state of DPF substrate surface which experienced different modes of failure. The authors utilized XRD to determine the crystalline structure of DPF samples, which specifically aimed to detect vitrification as DPF cordierite substrate become more amorphous from melting failure. The authors utilized SEM-EDS to determine ash morphology and chemical composition.

www.manaraa.com

2 .2Materials and Methods

2.2.1 DPF Ash and EGR Coolant Leak Derived Ash Analysis

Diesel Particulate Filters

The DPF substrates used herein were provided by Hunsicker Emission Services LLC. All substrates used are exhausted OEM DPFs from heavy duty diesel powered vehicles belonging to commercial fleets. The DPF substrate failures characterized as pinhole failure, melt failure, and crack failure were observed in DPF's used in urban transit bus driving application. These substrate failures were irreversible. The DPF substrate failure characterized as fouling failure was observed in a DPF used in highway driving application. The vehicle had operated with an unnoticed EGR coolant leak for an extended period of time.

Typical soot loadings and typical ash loadings in the exhausted urban transit bus DPF's were measured at 4-5 grams soot/Liter substrate and 25-30 grams ash/Liter substrate, respectively. These are moderately high soot and ash loadings for a DPF, but within the DPF substrate design parameters. (Aravelli 2007, McCormick W. A. 2011) Volumetric parameters of the DPFs are depicted in Table 2.1, and a cross-section photograph of an exhausted urban transit bus DPF is shown in Figure 2.1. This figure

www.manaraa.com

demonstrates an exhausted DPF which shows the dark colored DPF soot appears to be deposited on the inlet.

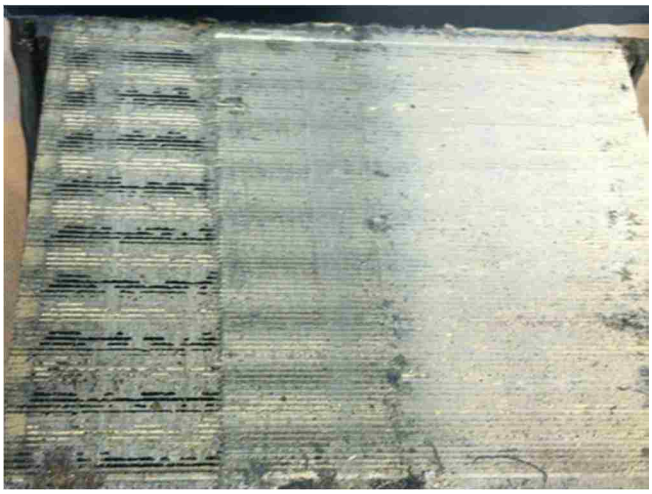

Figure 2.1. Cross-Section of a DPF, showing inlet (left-side), and outlet (right-side).

Table 2.1 Exhausted DPF characteristics from an urban transit bus fleet vehicle.

Parameters	Data
Substrate Composition	Cordierite
Length (cm)	30.5
Diameter (cm)	30.5
DPF Volume (L)	22.2
Cell density (cpsi)	200
DPF weight, as received (kg)	18.5
Weight loss, combustibles (soot) (g soot/L substrate)	4.5
Weight loss, non-combustibles (ash) (g ash/L substrate)	26.6

www.manaraa.com

2.1.2 ICP analysis of DPF Ash and EGR coolant leak derived ash

The inlet half and the outlet half of an exhausted urban bus transit fleet DPF were crushed separately and stored separately prior to chemical analysis. Figure 2.2(d) shows a DPF with inlet plugged by EGR coolant leak derived ash. Exhaust gas recirculation (EGR) cooler failure can cause coolant to leak into the exhaust after treatment system (Jesus Y.M.LD. 2012). The chemical components of ash are determined experimentally via strong acid treatment to dissolve ash components. The specific procedure includes: the inlet half and outlet half of a DPF entire substrate were cut apart, crushed into powder and stored separately. Next, 1.0 g of crushed inlet or outlet powder was dissolved separately into 0.1 L aqua regia solution with molar concentrations of 1.0 and 4.0 for hydrochloric acid and nitric acid, respectively. Reactions were carried out for 1 week on a magnetic stir plate with a stirring speed of 100 rpm. The solution was filtered to remove the insoluble components, which include cordierite. The leachate was then diluted by deionized water and analyzed for calcium, iron, zinc, sodium, potassium, sulfur and phosphorus using ICP-OES (PerkinElmer Optima 2100DV, US). A control test was performed on unused cordierite substrate and EGR coolant leak derived ash, using the same procedure.

www.manaraa.com

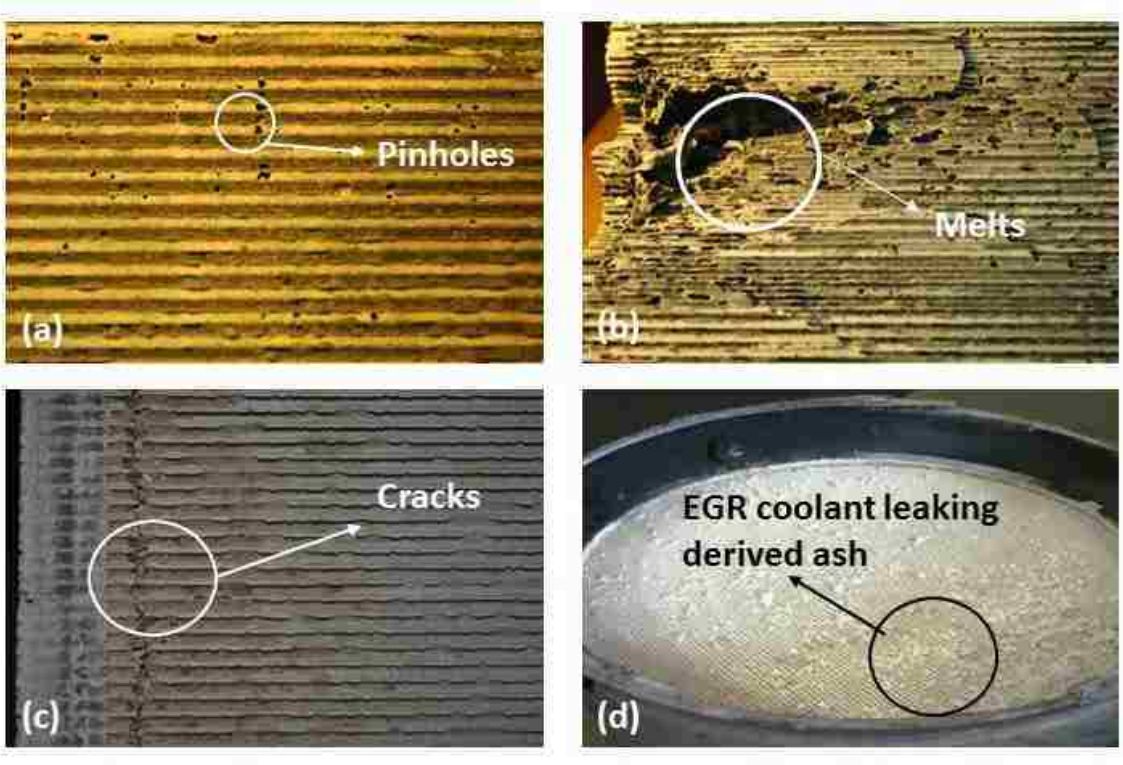

Figure 2.2. Photographs of a DPF which experiences; (a) Pinholes, (b) Melts, (c) Cracks and (d) EGR failure.

DPF ash from an exhausted urban bus transit fleet DPF was collected from DPF inlet channel surfaces. The agglomeration of small ash particles forms large size particles range from 45-160 nm. Micro-structures and elemental maps of ash particles were determined by Scanning Electron Microscopy Energy Dispersive Spectrometer (SEM-EDS).

Exhaust gas recirculation (EGR) coolant failures or coolant leaks form unique ash particles in the exhaust which agglomerate on the DPF inlet face. The larger agglomerated

www.manaraa.com

EGR coolant leak derived ash is different from lubricating oil derived ash in both morphology and chemical compositions due to the difference in formation pathway. The EGR coolant leak derived ash was collected off the surface of the DPF substrate inlet face. Scanning Electron Microscopy Energy Dispersive Spectrometer (SEM-EDS) (HITACHI, TM-1000) was applied to determine the physico-chemical characteristics of EGR coolant leak derived ash.

2.2 Pinhole, Melt and Crack Failure Analysis

The elemental composition of DPF pinholes, melts, and cracks were compared with new DPF samples. For each DPF failure, three parallel experiments were carried out on three different samples; each sample was analyzed with, SEM-EDS, XRD, and XPS. XPS and SEM-EDS samples were removed from DPF samples of interest (melt, crack, pinhole areas) via tweezers. Samples were then rinsed with deionized water and dried in an 110^{o}C oven for 24 hours, prior to analysis.

The SEM-EDS analysis was carried out to characterize the micro-structures of new DPF, pinholes, cracked areas and melted areas to reveal the physic-chemical changes.

www.manaraa.com

The EDS signal was obtained from the depth of 2-10μm according to the accelerating voltage. XPS signal was obtained from the depth around 3nm.

Samples for XRD analysis were prepared by crushing melted, cracked or pinholed area into a fine powered with a mortar and pestle. The crushed sample was rinsed with deionized water and dried in an 110°C oven for 24 hours, prior to analyses. X-ray Diffraction (XRD) was applied to characterize the physico-chemical properties of cordierite by determining crystalline phase change before and after DPF melting and vitrification. The X-ray Diffraction (XRD) (MiniFlex, Rigaku) analysis were carried out under electric voltage/current of 30 kV/15 mA. The scanning angle ranges from 10° to 90° with continous scanning and the scanning step was 0.02°.

DPF samples were analyzed by X-ray Photoelectron and Auger electron Spectroscopies (XPS-AES). The XPS-AES analysis was carried out with PHI Veraprobe 5000 XPS equipped with Monochromated AlK alpha source. The signal was obtained from the top 10nm of the sample with an analysis area of 100μm×1400μm. The composition and chemical state were investigated on the basis of areas and binding energies of Ca 2p, Mg 2s, Al 2p, Si 2p, C 1s, O 1s, Zn 2p, Na 1s and Fe 2p photoelectron peaks. The XPS-AES could provide intrinsic information of the surface chemical composition and their valences via electron detection with Kinetic energies between 10 and 2000 electron volts.

www.manaraa.com

2.3 Results and Discussion

2.3.1 Classification of Failures

Four specific modes of failure were observed for compromised DPFs provided by Hunsicker Emissions Services LLC. Figure 1.2 illustrates the mode of failure for four separate DPFs. The authors have characterized the failure mechanisms based on the visual appearance by which the DPF failed. Specifically, the figure demonstrates failure by pinholes (a), melting (b), cracking (c) and EGR coolant leak derived ash (d). Pinholes were observed when DPFs were cut in half and 0.1-10 mm holes between channels were observed by the authors. Melting failures were observed for DPFs where significant volume of the DPF melted and left a void. Cracking failures were observed on cross-sections of DPFs, where a crack continued through the entire cross-section of a DPF. The crack was located within one inch of the DPF outlet face, but its presence was not observable prior to cutting the DPF and exposing the cross section. The crack pattern is most likely attributed to the difference of the thermal expansions among these crystalline phases (Merkel G. 2001, O'Sullivan 2004, Choi. B. 2009, Maier 2010). Fouling failures were observed with layers of agglomerated ash on the inlet face that the DPF no longer

www.manaraa.com

was permeable via exhaust. These samples were sacrificially utilized for ash chemical appraisal, XRD analysis, XPS analysis, and SEM characterization, which are detailed herein.

2.3.2 Crushed DPF Substrate Ash and EGR coolant leak derived ash Chemical Compositions

DPF Ash composition varies between vehicles, but it can be generally stated that ash samples from light-duty and heavy-duty vehicles will contain oxides of calcium, zinc, magnesium, sulfur and phosphorus from lubricating oil, and a lesser amount of metal oxides from engine wear (Sappok A.S.M. 2009, Merkel G.C.W. 2001). In the present study, ash chemical compositions are appraised by either ICP-OES or SEM-EDS. The authors focused on seven components, specifically, Ca, Zn, Fe, Na, K, S and P. Results of ash composition analysis of a crushed DPF substrate based on ICP-OES are depicted in Table 2.2 and Figure 2.3. Corresponding SEM-EDS photograph and spectra are shown in Figure 2.4.

The total ash loading found in the separately crushed inlet and outlet substrate halves of an urban transit fleet DPF, were consistent with ash deposition results reported by others (Aravelli 2007, Sappok 2009). Figure 2.3 plots the inlet and outlet concentration

www.manaraa.com

by chemical species. Considering the chemical composition distributions in Figure 2.3, Ca composed the majority of ash with a concentration of 5.2 mg/g and 2.6 mg/g for the inlet and the outlet. Other compounds S, P, Na, Zn and Fe are found in the range of 1.25 mg/g to 4.6 mg/g. Potassium was found as trace levels in both the inlet and outlet, with concentrations of 0.15 mg/g for the inlet and 0.01mg/g for the outlet.

These results are in consensus with observations made by others, which show primary ash constituents include CaO (21-30 wt. %), sulfate (10-39 wt.%), MgO (5-7 wt.%), phosphate (11-16 wt. %), and ZnO (10-14 wt.%), with Na and K observed trace levels (< 1 wt.%), and varying levels of Fe_2O_3 (<1% to 25%) dependent on engine and exhaust system corrosion. (Merkel G. 2001, Givens W. 2003)

The detection of sodium and iron at relatively high concentrations in the crushed substrate of the exhausted DPF, as shown in Table 2.2, lends possible support to the laboratory controlled studies that observed corrosive interaction of sodium with substrate materials, and the role of iron in increasing the aggressiveness of this interaction.

ICP results of new cordierite are provided in Table 2.2 and Figure 2.3. By using the total amount of DPF ash provided in Table 2.2 with the DPF substrate density of 1.2kg/L can yield 21.2 grams of ash/L of substrate for the DPF inlet and 12.25 grams of ash/ L of substrate for the DPF outlet. Table 2.3 compares the composition of DPF ash

www.manaraa.com

(engine wear/lubricant) and EGR coolant leak failure ash. These two ash types have similar chemical compositions, with high concentration of Ca, Zn, S and P.

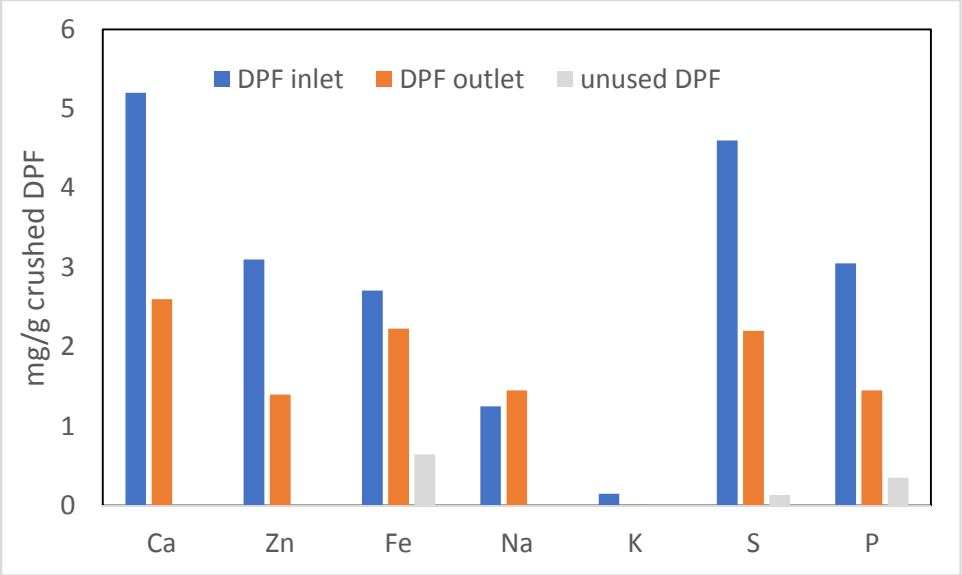

Figure 2.3. Commercial fleet DPF ash chemical components (mg ash components/ gram of DPF substrate).

www.manaraa.com

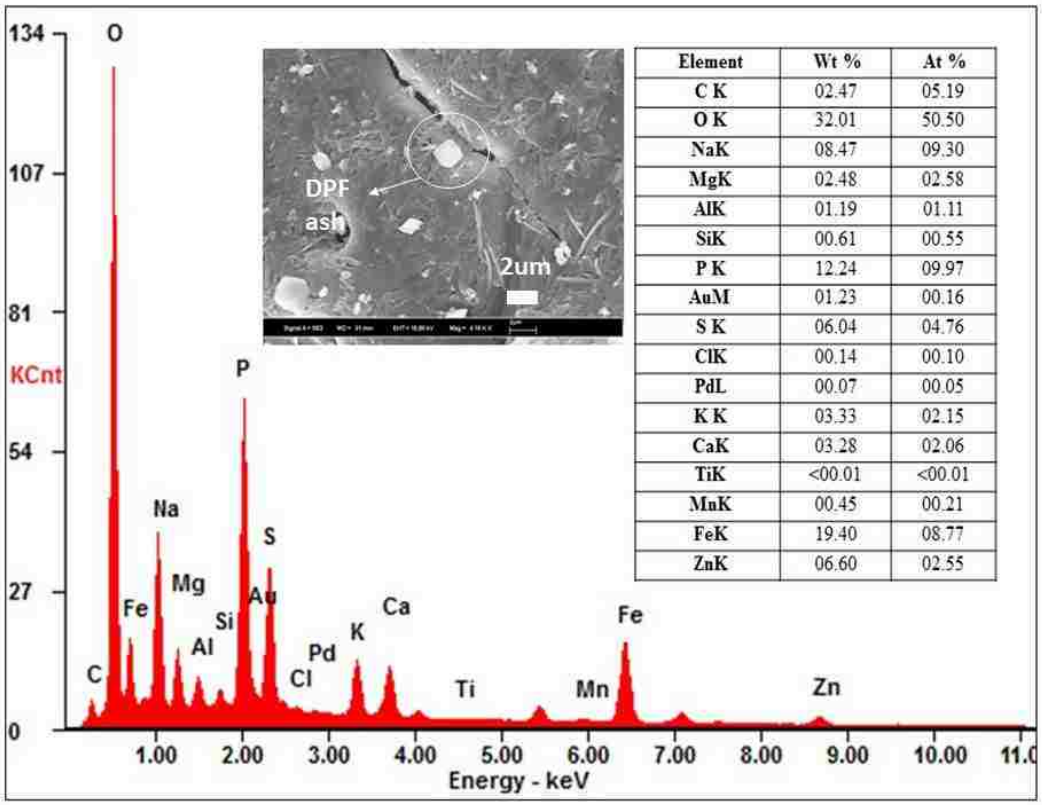

Figure 2.4. SEM-EDS spectra of DPF ash particle (coated by Au/Pd).

Table 2.2 DPF Inlet and Outlet ash chemical compositions

Component	mg component/g DPF substrate							
	Ca	Zn	Fe	Na	K	S	P	Total
Average Inlet Ash	5.200	3.100	2.710	1.250	0.150	4.600	3.050	20.060
Average Outlet Ash	2.600	1.400	2.230	1.450	0.010	2.200	1.450	11.340
Unused DPF	0.002	0	0.645	0.001	0	0.134	0.349	1.131

www.manaraa.com

Table 2.3 Comparison of chemical compositions between DPF ash and EGR coolant leak ash

Component	%							
	Ca	Zn	Fe	Na	K	S	P	Total
Average Inlet Ash	27.460	16.376	10.909	6.598	0.792	23.593	14.269	100
Average Outlet Ash	25.448	13.713	15.525	14.193	0.097	20.237	10.784	100
EGR	22.943	21.225	3.870	11.871	2.274	24.835	12.982	100

2.3.3 Characterizations of Pinholes, Melting, Cracking sections and EGR Failure Ash

2.3.3.1 Characterizing an Unused DPF Substrate

Figure 2.5 depicts the XRD analysis profile of a new unused DPF substrate without pinholes, melting, or cracks. The XRD analysis was performed by scanning angle range from $\theta=10^{o}$ to $\theta=90^{o}$ under a wavelength of 1.5406Å. XRD analysis indicates that the original unused DPF substrate possessed two crystalline structures. These two crystalline phases, include $Mg_2Al_4Si_5O_{18}$ (a) and minor phase of $(Mg,Fe)_2Al_4Si_5O_{18}$ show strong correlation with the XRD peaks, as they form the major chemical composition of cordierite. The average crystallinity of both phases, for the unused DPF, based on calculating the

www.manaraa.com

crystal area, are 97% for $Mg_2Al_4Si_5O_{18}$ (a) and 99% for $(Mg,Fe)_2Al_4Si_5O_{18}$, – indicating a high degree of crystallinity for the unused DPF.

The XPS analysis in Figure 2.7(a) compares the spectra of the unused DPF peaks with three figures (pinhole surface, melted surface, and cracked surface). Chemical components of the surface of the unused DPF lack ash components (Na, Ca, Fe, Zn) discovered in other samples. Therefore, these findings suggest that ash composition may play an important role in DPF failure. SEM photographs in Figure 2.6 compare the micro-structures of unused DPF with melted DPF, pinholes and cracking. It is obviously that unused DPF shows regular shape with layer structures. And this structure changes as those layers combine with each other through vitrification. As observed in Figure 2.8, Ca, Zn, K, Fe were not observed on the unused DPF.

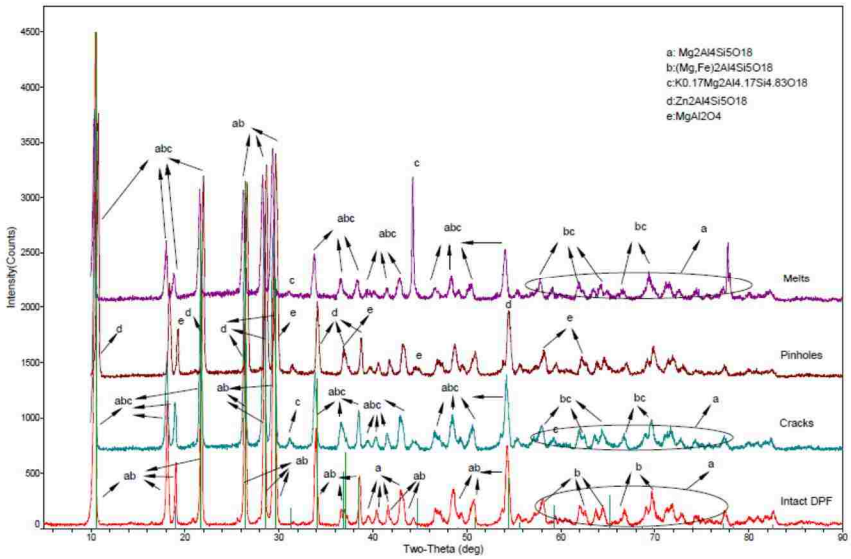

Figure 2.5 XRD patterns from unused DPF, Pinholes, Melts and Cracks samples.

www.manaraa.com

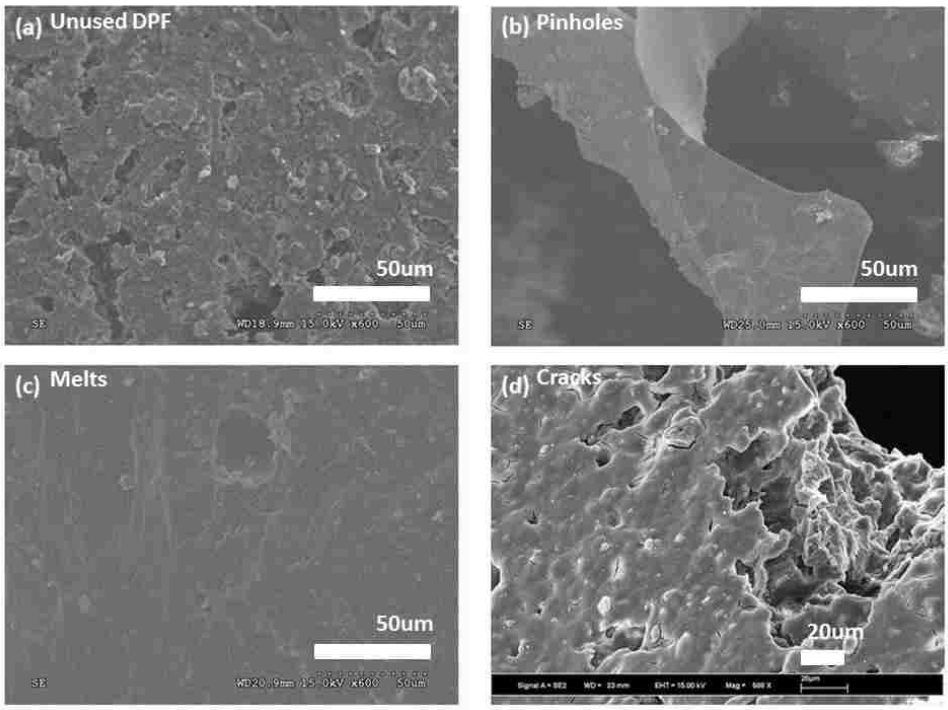

Figure 2.6 SEM photographs of unused cordierite (a), Pinholes (b), Melts (c) and cracks (d)

www.manaraa.com

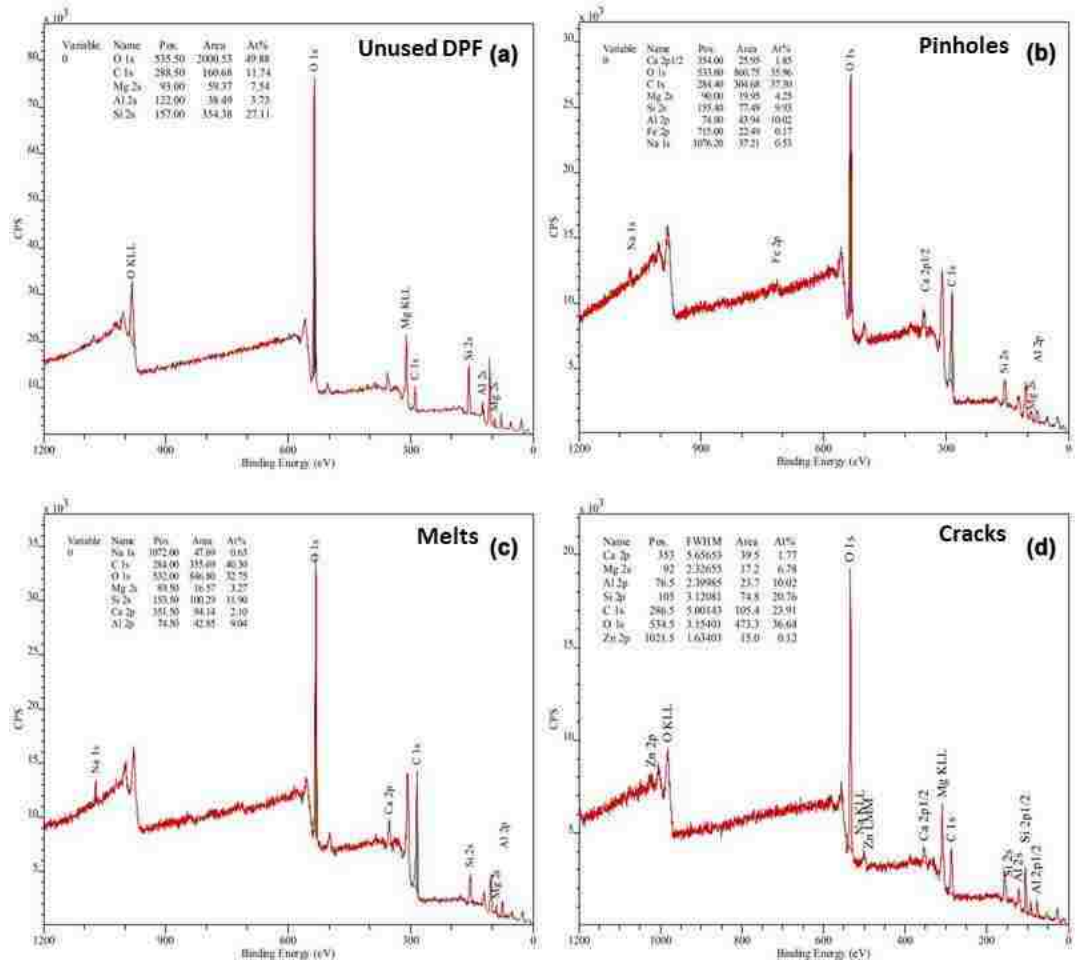

Figure 2.7 XPS scanning survey spectra of unused DPF (a), Pinholes (b), Melts (c) and Cracks (d)

2.3.3.2 Characterizing Failure by Pinholes

The XRD analysis of pinhole areas shown in Figure 2.5 found two unique crystalline phases (not found within the unused DPF). The major crystalline phase $Zn_2Al_4Si_5O_{18}$ (d) and minor crystalline phases of $MgAl_2O_4$ (e) were observed. Compared with the XRD pattern of unused DPF, the appearance of unused crystalline phases confirms the potential

www.manaraa.com

for chemical reactions between cordierite substrate and ash. The disappearance of $Mg_2Al_4Si_5O_{18}$ after pinholing might be due to prolonged heating, as the inclusion of zinc in the observed crystalline phase may facilitate the phase change from $Mg_2Al_4Si_5O_{18}$ to $Zn_2Al_4Si_5O_{18}$. Further, the observed peak intensity of phase (e) in pinholes is low compared with the unused DPF, which suggests the pinhole areas display less perfect crystal orientation and more amorphous phases. Further, the DPF pinholes area calculated crystallinity are 99% and 89% for (d) and (e) respectively.

According to the XPS data, in Figure 2.7(b) and Table 2.3, the surfaces of pinholes contain several components including Na, Ca, and Fe which belong to the ash. The corresponding chemical partition shown in Figure 2.7(b) with typical Ca 2p comprised of 1.85%, followed by Na 1s with 0.53% and Fe 2p in trace amounts of 0.17%. Compared with unused DPF, the appearance of Na 1s, Ca 2p, and Fe 2p demonstrate the presence of Na, Ca and Fe might have impact on the cordierite substrate (Figure 2.7). Since the XPS has a nano-scale penetrating depth (10 nm), the disappearance of Zn peak in XPS spectrum may reveal that Zn has penetrate deeper into the substrate.

The SEM-EDS spectra in Figure 2.8d of pinholes indicate the presence of Zn, Fe, P, Na, Ca, S and. The EDS data acquired the information through the selected SEM area shows zinc was detected at the highest concentrations surrounding the pinholes. This

www.manaraa.com

observation suggests that zinc may be an important element in the formation of pinholes, as XRD data indicates the presence of $Zn_2Al_4Si_5O_{18}$ to be the major phase in Figure 2.5.

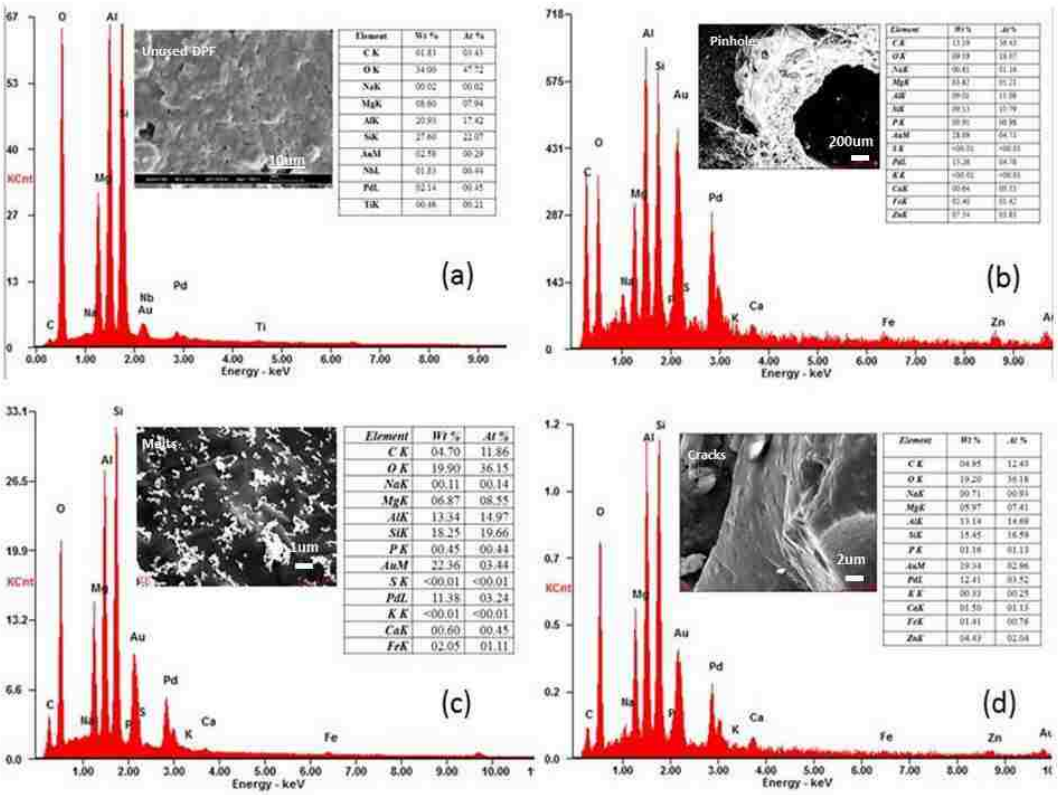

Figure 2.8. SEM-EDS photographs and spectra of Unused DPF(a), Pinholes (b), Melts (c) and cracks (d) (material coated with Au/Pd).

2.3.3.3 Characterizing Failure by Melting

XRD spectra of DPF melts observed three unique crystalline phases, with major crystalline phases of $Mg_2Al_4Si_5O_{18}$(a), $(Mg, Fe)_2Al_4Si_5O_{18}$ (b), and one minor crystalline phase of

www.manaraa.com

$K_{0.17}Mg_2Al_{4.17}Si_{4.83}O_{18}$ (c). The crystallinity of $Mg_2Al_4Si_5O_{18}$ (a), $(Mg,Fe)_2Al_4Si_5O_{18}$ (b) and $K_{0.17}Mg_2Al_{4.17}Si_{4.83}O_{18}$ (c) are 77%, 82% and 85% respectively, which are much less than the crystallinity of these phases in the unused DPF. This indicates that these two phases are less crystalline due to a shift into a more amorphous, or glass-like structure – which demonstrates that DPF melting failure observed in the field, can be confirmed via XRD.

The corresponding XPS spectrum of the melted DPF in Figure 2.7 (c) shows the melted surface contains peaks of sodium and calcium -which are not present on unused DPF spectra. The presence of these compounds suggest that they are present during the interaction of ash and cordierite in melting failure.

The SEM-EDS spectra of melts are shown in Figure 2.8c. From the spectra, it seems iron may play an important role in the DPF melting, as iron is detected at the highest levels, followed by Ca, P, Na, S and K.

2.3.3.4 Characterizing Failure by Cracking

The XRD analysis of the cracked DPF observed the same phases as the melted sample, which includes; $Mg_2Al_4Si_5O_{18}$ (a), $(Mg,Fe)_2Al_4Si_5O_{18}$ (b) and $K_{0.17}Mg_2Al_{4.17}Si_{4.83}O_{18}$ (c). The respective crystallinity for the two major phases are 91% for $Mg_2Al_4Si_5O_{18}$ (a) and

www.manaraa.com

93% for $(Mg,Fe)_2Al_4Si_5O_{18}$ (b). For the minor trace phase, the crystallinity was determined to be 88% for $K_{0.17}Mg_2Al_{4.17}Si_{4.83}O_{18}$ (c).

Figure 2.7(d) shows the XPS spectrum of surface chemical composition of DPF cracks. Interestingly, the relatively major element (with respect to ash composition) of calcium and trace element of zinc appeared with their composition indicated in Figure 2.7(d) and Table 2.3. Compared with pinhole failures, the zinc accumulated on the cracked area with higher concentration, as Zn did not appear on major chemical composition in Figure 2.7(b). These higher Zinc peaks confirm the findings of Maier et al.(2010), of zinc concentrations surrounding cracks (Maier 2010). However, the underlying mechanisms are not yet understood as to why zinc concentrations are prevalent near cracks. In the chapter 3, the author demonstrated details why the Zn tend to form cracking of the DPF and the underlying mechanisms (Chapter 3). Besides, calcium peaks have been found in pinholes, melts and cracks with different concentrations according to the Figure 2.7(b, c and d).

The XPS data was confirmed by SEM-EDS spectra of cracking area, which shows zinc accumulation in the area of cracking failure. Species of Ca, Fe, P, Na, K were also observed at lower levels than zinc surrounding the area of cracking. It should be pointed out that Ca, Fe, P and Na have been found in all the three kinds of DPF failures, although the specific mechanism of each ash species in failure is not well understood.

www.manaraa.com

2.3.3.5 Fouling from EGR Coolant Leak Derived Ash Particles

Various pathways are possible for engine fluids to come in contact with the DPF substrate. Coolant leaks from high temperature exhaust gas recirculation (EGR) failure (Jesus Y.M.LD. 2012). excess lubricant from engine failure, and fuel from incomplete combustion all possess the capability to enter the exhaust stream and to contaminate the DPF. The white ash substance shown layered on the DPF inlet face, are clusters of ash as large as 1/8-1/4 inch in diameter. The ash clusters formed when the vehicle was driven with an unnoticed EGR coolant leak failure for an extended period of time. As coolant passes through the engine's combustion chamber, the increased % moisture in the exhaust produces steam. The ash agglomerates formed in these conditions are larger, and different in morphology, from typical engine-lube derived ash, causing them to load differently in the DPF channels. The larger ash agglomerates can also bridge more easily across the DPF inlet face channels than typical DPF ash, creating a layer of ash / soot on the DPF face. This can result in relatively high engine backpressure at relatively low DPF ash loadings, increasing the frequency required for DPF maintenance.

Scanning Electron Microscopy (HITACHI, TM1000) of the EGR coolant derived ash particles, illustrated in Figure 2.9, shows the white ash substance on the DPF

www.manaraa.com

inlet face are comprised of 5-10 μm sized ash agglomerates. The agglomerates are loosely packed, and can act as an adsorbent for smaller soot or ash particles in the exhaust gas. An elemental spectrum of the white ash substance was acquired using EDS under accelerating voltage of 15 keV. The result shows the observed EGR coolant leak derived ash is composed of similar chemical compounds as typical DPF lube ash, although at different elemental distributions. The EDS results show no detected zinc or magnesium, and much higher levels of potassium and sodium. High levels of potassium are indicative of a coolant leak, as fully formulated HDD coolants may contain significant quantities of S (sulfur), P(phosphorus), Na (sodium) and K (potassium) (Jesus Y.M.LD. 2012).

While analyzing the chemical composition of EGR failure ash, the authors observed shinny spots on the particle surface (Figure 2.10). EDS analysis confirms that 48.9% of weight of these white ash particles are iron. Merkel (2001) indicated the iron in DPF ash is mainly attributed to rusting of exhaust component upstream. (Merkel G. 2001) Therefore, the EGR coolant failure could contribute to exhaust system corrosion and transport iron particles within the DPF.

The presence of high levels of alkalis (Na, K) in the EGR Coolant leak derived ash can compromise the durability of the DPF. The alkalis have been observed to poison the catalyst coatings in the Diesel Oxidation Catalysts and Diesel Particulate Filters with

www.manaraa.com

respect to NO oxidation, or NO_2 make (Jesus Y.M.LD. 2012). The reduction of the NO oxidation performance of the DOC and DPF can compromise the soot regeneration process in the DPF during normal vehicle operating conditions, resulting in higher soot loads in the DPF. When the soot does light off, the increased exotherm from the higher soot loads can generate excessive temperatures in the DPF, leading to the severe operating conditions at which the alkalis and iron have been observed to interact with cordierite and silicon carbide substrate materials, resulting in pinhole, melt, and crack (Merkel G. 2001). This emphasizes the importance of regular cooling system maintenance by the vehicle operator to protect the particulate matter emission capture and useful life of the DPF.

www.manaraa.com

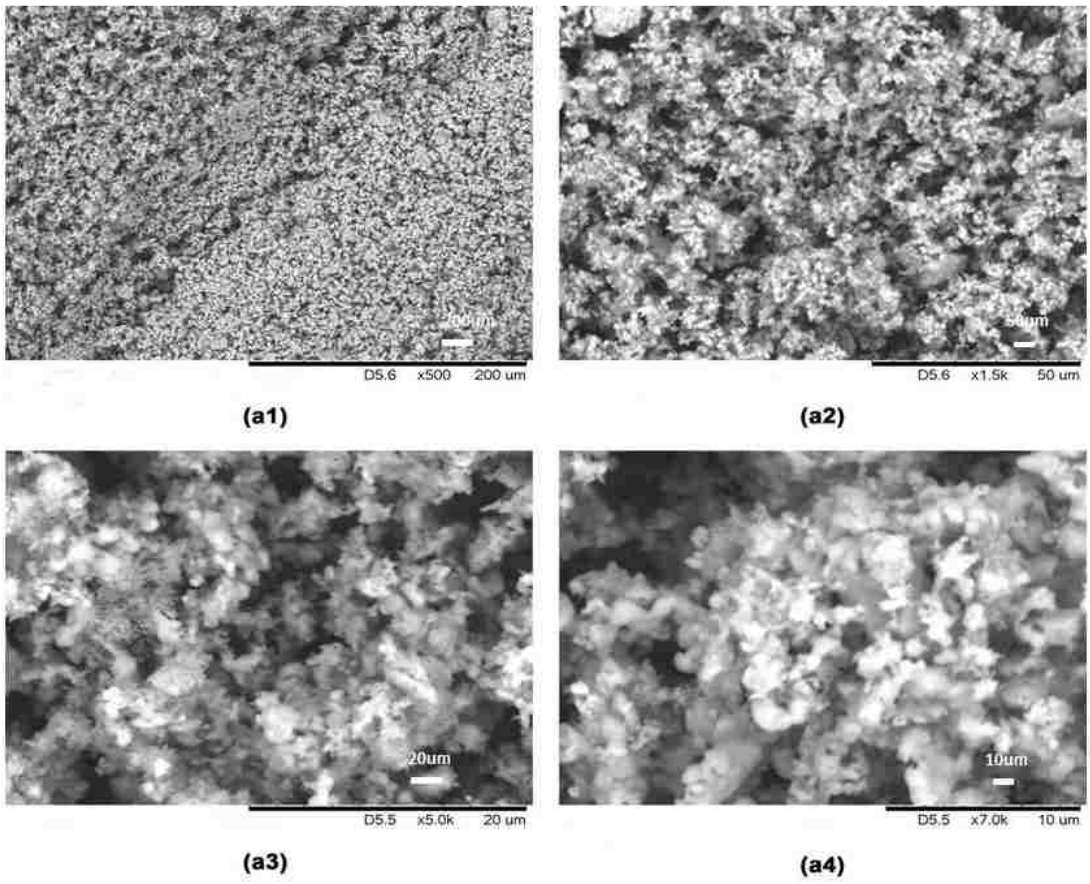

Figure 2.9. SEM images at 15.0 kv, showing surface structures of EGR Coolant Leak Derived Ash Particulate under different magnifications range from 500 to 10K. (a1 to a4).

www.manaraa.com

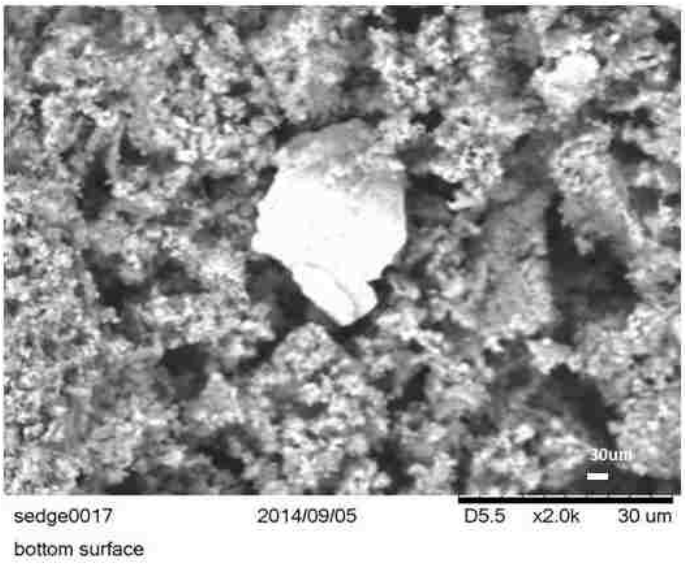

Figure 2.10. SEM image showing an iron particle embedded within an EGR Coolant Leak Derived Ash Particulate.

www.manaraa.com

Table 2.4 Surface elemental partition according to XPS scanning spectra

	Concentration At%			
	New DPF	Pinhole Failure	Melting Failure	Cracking Failure
O 1s	31.05	35.96	32.75	36.64
C 1s	41.16	37.3	40.3	23.91
Mg 2s	6.76	4.25	3.27	6.78
Si 2p	13.09	9.93	11.9	20.76
Al 2p	7.94	10.02	9.04	10.02
Fe 2p	-	0.17	-	-
Na 1s	-	0.53	0.63	-
Zn 2p	-	-	-	0.12
Ca 2p1/2	-	1.85	-	-
Ca 2p	-	-	2.1	1.77

www.manaraa.com

Table 2.5 Chemical distribution according to SEM-EDS spectra

	Concentration Wt%			
	New DPF	**Pinhole failure**	Melting Failure	**Cracking Failure**
O K	34	**9.19**	19.9	**19.2**
C K	1.83	**13.19**	4.7	**4.95**
Mg K	8.6	**3.82**	6.87	**5.97**
Si K	27.6	**9.13**	18.25	**15.45**
Al K	20.93	**9.01**	13.34	**13.34**
Na K	0.02	**0.81**	0.11	**0.71**
P K		**0.91**	0.45	**1.16**
S K		**<0.01**	<0.01	
K K		**<0.01**	<0.01	**0.33**
Ca K		**0.64**	0.6	**1.5**
Fe K		**2.4**	2.05	**1.41**
Au M	2.58	**28.09**	22.36	**19.34**
Pd L	2.14	**15.26**	11.38	**12.41**
Zn K		**7.54**		**4.43**
Nb L	1.83			
Ti K	0.46			

www.manaraa.com

2.4 Summary/Conclusions

The results presented herein characterized observed failures of cordierite DPFs during commercial fleet use, and classified the failures as; pinhole failure, melt failure, crack failure, and fouling failure. The detailed analysis of DPF ash confirmed the varying levels of Ca, Fe, S, P, Na, K and Zn as ash species. XRD analysis on cordierite substrate indicates significant crystalline phase changes following pinhole failure and melt failure. Specifically, the crystallinity of cordierite substrate phases decreased from 97% and 99% for the new DPF to only 77%, 82% and 85% for melt failure samples. Specifically, zinc is uniquely observed in the crystalline phases surrounding a crack failure – suggesting the zinc ash species may play a fundamental role in cracking. Further, the SEM-EDS observed iron at elevated levels within melted sections. Additionally, pinhole areas measured elevated levels of zinc and iron, as compared to other ash chemical species. EDS analysis determined chemical composition of EGR coolant leak derived ash agglomerate is composed of sodium, phosphorus, sulfur, potassium, calcium and iron, similar to the composition of typical DPF ash, but with higher than normal level of alkalis Na and K. These EGR Coolant leak ash agglomerates are also larger than typical DPF ash agglomerates, different in morphology, and can shield the DPF's inlet face such that DPFs become impenetrable to exhaust, rendering vehicles temporarily un-operable. Analysis of

www.manaraa.com

commercial fleet DPFs support that ash chemical compositions are consistent between different failure modes of pinholes, cracks and melts. Field observations reported herein of cordierite DPF failure during commercial fleet use, offers support to previous laboratory controlled research observations that suggest ash components, specifically high levels of alkalis, influence monolithic cordierite DPF substrate failure.

Acknowledgements

This work is supported by the Lehigh University and Hunsicker Emissions Services LLC through Research for Advanced Manufacturing in Pennsylvania Program (RAMP) Project and Pennsylvania Infrastructure Technology Alliance (PITA).

2.5 References

Aravelli, K. a. H., A. (2007). "Improved Lifetime Pressure Drop Management for Robust Cordierite (RC) Filters with Asymmetric Cell Technology (ACT)." SAE International. Paper #: 2007-01-0920

C.A.R.B. (2015). "Evaluation of particulate matter filters in on road heavy duty diesel vehicle applications."

www.manaraa.com

Choi. B., L. B., Jeong J.W. (2009). "Effects of hydrothermal aging on SiC-DPF with metal oxide ash and alkali metals." Journal of Industrial and Engineering Chemistry **15**: 707-715.

Dario M. T., B. A. (1998). "Interaction of some pollutant oxides on durability of silicon carbide as a material for diesel vehicle filters." Journal of Materials science **33**: 139-145.

Fino (2007). "Diesel Emission Control: Catalytic filters for particulate removal." Science and Technology of Advanced Materials **8**: 93-100.

Givens W., e. a. (2003). "Lube formulation effects on transfer of elements to exhaust aftertreatment system components." SAE International **2003-01-3109**.

Hardenberg, H. O., and F. W. Hase (1979). "An empirical formula for computing the pressure rise delay of a fuel from its cetane number and from the relevant parameters of direct-injection diesel engines." SAE International. Paper #: 790493

Lopez De Jesus, Y.M., et al (2012). "Effect of coolant exposure on diesel exhaust aftertreatment performance." SAE International. Paper #:2012-01-1091

Konstandopoulos, A., and Johnson J.H. (1989). "Wall-Flow Diesel Particulate Filters their Pressure Drop and Collection Efficiency." SAE International. Paper #:890405

Liati, A., et al (2013). "Metal Particle Emissions in the Exhaust Stream of Diesel Engines: An Electron Microscope Study." Environmental Science & Technology **47**(24): 14495-14501.

www.manaraa.com

Maier, N., et al (2010). "Mechanisms and orientation dependence of the corrosion of single crystal cordierite by model diesel particulate ashes." Journal of European Ceramic Society **30**(7): 1629-1640.

Maricq, M. M. (2007). "Chemical characterization of particulate emissions from diesel engines: A review." Journal of Aerosol Science **38**(11): 1079-1118.

McCormick W. A., e. a. (2011). "Impact of biodiesel impurities on the performance and durability of DOC, DPF and SCR technologies." SAE International Paper #:**2011-01-1136**.

Merkel G., C. W., and Warren C. (2001). "Thermal Durability of Wall-Flow Ceramic Diesel Particulate Filters." SAE International. Paper #: 2001-01-0190

Montanaro L., B. A. (1994). "Influence of some pollutants on the durability of cordierite filters for diesel cars." Ceramics International **20**(3): 169-174.

O'Sullivan, D., et al. (2004). "Degradation resistance of silicon carbide diesel particulate filters to diesel fuel ash deposits." Journal of Materials Research **19**(10): 2913-2921.

Sappok, A., S. M., Vianna, T., and Wong, V. (2009). "Characteristics and Effects of Ash Accumulation on Diesel Particulate Filter Performance: Rapidly Aged and Field Aged Results." SAE International.Paper #:2009-01-1086

Stamatelos, A. M. (1997). "A review of the effect of particulate traps on the efficiency of vehicle diesel engines." Energy conversion and management **38**(1): 83-89.

www.manaraa.com

Stratakis, G. A., Psarianos, D.L. and Stamatelos, A.M. (2002). "Experimental investigation of the pressure drop in porous ceramic diesel particulate filters." Proceedings of the Institution of Mechanical Engineers, Part D: Journal of Automobile Engineering **216**(9): 773-784.

www.manaraa.com

Chapter 3

Fundamentally understanding the thermal chemical conditions leading to the DPF premature failures

Abstract

The effects of ash components of Na, K, Fe, Zn and Ca with porous cordierite were investigated at elevated temperatures. Samples of unused diesel particulate filter cordierite substrate were doped with those contaminants separately. The doped samples were heated in a thermal gravimetric analyzer to 300, 500, 900, and 1100°C and treated under different time profile that simulate the DPF regeneration process. The resulting interactions were analyzed with scanning electron microscopy (SEM), Electron Probe Microscopy Analysis (EPMA) and x-ray diffraction (XRD). The alkalis and iron induced corrosion and degradation to the cordierite substrate at temperatures lower than pristine cordierite substrate samples. The alkali metal Na and K have the most severe affection on the cordierite, followed by Fe and Zn, Ca appeared to have lowest effect on the substrate. The degradation of the cordierite substrate can lower the porosity of the substrate by melting the surface, further result in cracking. The corrosion and degradation pathway followed the porous structure as observed with EPMA.

www.manaraa.com

3.1 Introduction

In this chapter, the author is trying to understand the fundamental thermal and chemical conditions that leads to the premature failure of the substrate by lab scale simulate tests. Compared to silicon carbide, the cordierite ceramics are widely used due to low thermal expansion coefficient, low dielectric constant, high resistance to thermal shock and high refractoriness. In the previous chapter, the author analyzed the exhausted DPF and give some hints that these metal ash components may attack the cordierite substrate. But how does this happen? And what is the corrosive mechanism? Which ash components have the greatest affect?

The individual metal ash components and the respective concentrations that accumulate in the DPFs depends on variation in diesel engine operating conditions, different additives in fuel and lubricants, as well as upstream engine failure events. Based on the previous tests, the DPF ashes are composed of Fe, Zn, S, P, Ca, Na, and K (Yang K. 2016, Givens W.A. 2003, Sappok A. 2011, Bachiorrini A. 1996). Jesus (2012) demonstrated that Exhaust Gas Recirculation (EGR) coolant leaking into the engine exhaust can result in high concentrations of Na and K in DPF ash (Jesus Y.M.L.D. 2012). Na and K concentrations can also increase by wide spreading use of bio-diesel, as concentrations can reach 20 mg of Na per liter of biofuel. This can further increase the

www.manaraa.com

corrosion risk of cordierite substrate (Williams A. 2011). Among the ash components, Zn, Ca, S, and P are mainly derived from the lubricating oil additives. Iron found in the accumulated DPF ash is most likely derived from wear and corrosion of upstream engine and the exhaust (Merkel G.A. 2001). The composition of metal ash components that accumulate in the DPF is generally in the oxide state or combined with phosphorus, sulfur to form salts.

Past researches indicated the interactions between metal ash components and cordierite materials at temperature lower than melting temperature of pristine cordierite (1470^{o}C) have been well documented in controlled laboratory studies (Bachiorrini A. 1996, Dario M.T. 1998, Montanaro L. 1994, Rohan P. 2004). Some previous studies have shown that metal ash components can induce transformation of the cordierite crystallinity and degrade the structure (Bachiorrini A. 1996, Dario M.T. 1998, Montanaro L. 1994). For example, sodium can melt the substrate by react with it at temperature of 830^{o}C and alter the cordierite substrate after only 5 minutes at 1000^{o}C (Montanaro L. 1994, Maier N. 2010). However, Fe and Zn ash components interact with cordierite substrate need temperature well above 1000^{o}C (Pomeroy M.J. 2012). The previous hypothesis of reactions procedure between iron and cordierite include staining, pitting, surface sintering, liquefaction, pinholes and bulk melting with increased temperature and time (Merkel G.A.

www.manaraa.com

2001). Zinc dialkyldithiophosphate (ZDDP), found in lubricating oil contains; phosphorous, sulfur, and zinc can react with the cordierite to form a 'glaze' on cordierite. The glaze could mask the porous surface of cordierite (Bunting B.G. 2005). Zinc derived from lubricating oil reacts with the cordierite substrate producing new crystalline phases ($ZnAl_2O_4$ and $ZnSiO_4$) at 1000°C (Scardi P. 1994). Although the zinc-cordierite interaction has already been observed, the underlying mechanisms of the glaze-like surface formation is not clear. When calcium doped cordierite was treated at 1050°C for 10 minutes in simulation experiments, the crystalline phase containining calcium (stanfieldite) was detected after thermal treatment (Maier N. 2010). Specifically, the reaction between cordierite and CaO produces melilite at 1000°C after 1 hour of exposure. In addition, at 700°C calcium doped cordierite can produce trace amounts of both α-carnegieite and β-carnegieite after 5 minutes at 700°C to 1000°C (Montanaro L. 1994). Further, Ibrahim (2011) indicated that cordierite sintered with calcium at 900°C to form the minor crystalline phase of anorthite (Ibrahim N. 2011). The 1% of calcium oxide is detected as the cordierite crystalline phase, with the anorthite crystalline phase detected at up to 5% of calcium oxide (Ibrahim N. 2011).

www.manaraa.com

The author has observed the premature failure in the previous chapter and in the chapter herein, the author is mainly focused on providing insight understanding of the premature failures. Many of the previous studies have investigated the interaction of cordierite powders with chemical powders. However, in the present study manufactured cordierite substrates were utilized. Additionally, the laboratory controlled studies to date have focused on narrow temperature ranges, when compared with the temperature conditions that a DPF is exposed to in commercial diesel engine exhaust application (Montanaro L. 1994, Negro A. 1993, Scardi P. 1994, Maier N. 2010, Takahashi J. 1998, Pomeroy M.J. 2012). This chapter illustrates how individual metal ash components visually disperse within cordierite substrate materials at a wide range of exhaust temperature conditions. Moreover, this chapter focus on the investigation of the morphology (glazing, melting, cracking) and physical structure of the same cordierite materials to determine a possible relationship between migration of individual ash components and the transformation of cordierite morphology and crystallinity.

Herein, experiments were carried out to simulate the cordierite DPF substrate reactions with single ash components including sodium carbonate, potassium phosphate, and iron sulfate.

www.manaraa.com

The ash loading for Na, K, Fe, Zn and Ca are 5wt%, 5wt%, 10wt%, 10wt% and 20wt% (respectively) based on the element composition. The ash layer thickness can reach 0.13 mm for a loading of 42 g/L for a vehicle operating approximately 200,000 miles (Sappok A. 2011). The iron ash loadings were selected to correlate with the estimated ash accumulation in a DPF after 1200-1500 hours of vehicle operation (Givens W.A. 2003, Kimura K. 2006). The sodium and potassium loadings were selected to correlate to DPFs impacted by upstream EGR cooler failure events, resulting in coolant loss into the engine exhaust and high sodium and potassium loading in the emission control systems (Jesus Y.M.L.D. 2012). The calcium concentration is around 12%, by mass of ash, and zinc concentration around 10%, by mass of ash, for DPFs utilized for 160,000 miles (Kimura K. 2006). Since the Ca and Zn exist in the DPF at such high concentrations, herein, the authors selected the ash loading for cordierite substrate of 20% by mass for Ca and 10% by mass for Zn, corresponding to 0.1 kg of Ca/L substrate and 0.05 kg of Zn/L substrate.

The two key heat treatment parameters of temperature and exposure time are selected based on diesel engine exhaust temperature profiles. The exhaust gas temperatures range between 300ºC to 600ºC, depending on engine and operating parameters (Donaldson). The design temperature for DPF active regeneration is in the range of 600ºC, but can spike as high as 900ºC (Chen K. 2010). The combustion of soot during active

www.manaraa.com

regeneration is highly exothermic reaction, and if uncontrolled, can cause DPF temperatures to reach above 1000ºC (Law M.C. 2004). Due to these variations in DPF temperature conditions, this paper widens the temperature ranges investigated, with temperatures investigated from 300ºC to 1100ºC. The specified exposure time at elevated temperatures is 0.5 hour, 1 hour and 3 hour. Due to the much more rigid reaction conditions Ca and Zn need to react with the substrate, the author prolong the thermal treatment time of 10 hours at 300ºC for these two elements in order to simulate several cycles of regeneration. The short heat treatment times were chosen to reflect the estimated time that a diesel particulate filter would experience at elevated temperature during one to five active regenerations which was in accordance with previous research (Ogunwumi R.S. 2007).

The surface microstructure changes of cordierite under different time at temperature conditions are characterized by SEM. The single ash penetration, dispersion, and reaction pathways are revealed by element mapping with EPMA. The bulk crystalline phase changes were investigated with XRD.

3.2. Materials and Methods

3.2.1 Cordierite Substrate Sample Preparation

www.manaraa.com

An uncoated commercial, 400 cpsi cordierite substrate (NGK, Japan) was used to prepare cordierite substrate samples. The 4inch (10.16cm) length x 3.5 inch (8.89cm) diameter round substrate was cut between channel walls to form a rectangular substrate sample. The individual cordierite substrate samples were 10 cm long, 1.6 cm wide, and 0.7 cm thick. Each sample was approximately 14 channel widths wide, and 5 channel widths thick, with estimated wall thickness of 10 mils. The target mass of each sample was 5 grams. The prepared cordierite samples were rinsed with deionized water to remove any dust or debris from the cutting process, and then dried in an 105°C oven for 24 hours. Each sample was weighed and recorded.

3.2.2Deposition of Na_2CO_3, K_2PO_4, $FeSO_4$ on the Cordierite Substrate Sample

Water based solutions containing $5gL^{-1}$ of Na_2CO_3, $FeSO_4$ and K_3PO_4 were prepared in 1 L beakers as three separate solutions. And 20 g/L of calcium acetate and zinc phosphate were prepared in 1 L beakers as two separate solutions on the other hand. Two dried rectangular, cordierite substrate samples were then placed into the 1 L beaker containing one of the solutions. The sample was completely submerged in solution. The samples were exposed to the solution for one week. The samples were removed from the beakers and dried in an 105°C oven for 24 hours. The cordierite substrate samples were

www.manaraa.com

then cleaned with dehydrated ethanol solution. The samples soaked in the solution under ultrasonic treatment for 5 minutes to remove unreacted, residual crystals from the sodium, iron, potassium, zinc and calcium solutions. The samples were removed from the ethanol solution and dried in an 105°C oven for 24 hours. The mass of each sample was recorded, and the weight difference for each sample was calculated. As detailed in Table 1, the target mass loading was 5% for sodium, 10% for iron, 5% for potassium, 10% for zinc and 20% for calcium. If the target mass loading was not achieved, the same procedure was repeated to obtain the target mass loading of each substrate sample.

Table 3.1. Sample preparation and treatment description: ash mass loading (% dry weight), thermal treatment temperature (°C) and thermal exposure time (hour).

Ash-substrate Composition		Temperature (°C) and Time (hour) of Thermal Exposure							
Ash component	Ash Loading (% as Na, Fe or K)	Unheated	300°C	500°C	900°C			1100°C	
Na-substrate (Na_2CO_3)	5%	0	1	1	0.5	1	3	1	3
Fe-substrate ($FeSO_4$)	10%	0	1	1	0.5	1	3	1	3
K-substrate (K_3PO_4)	5%	0	1	1	0.5	1	3	1	3
Pristine substrate (blank)	0%		1	1		1		1	

Table 3.2 Sample preparation and treatment description corresponding for Zn and Ca doped substrate

Ash-substrate composition		Temperature (°C) and time (hr) of thermal exposure							
Ash component	Ash loading (% as Ca or Zn)	300°C		500°C		900°C		1100°C	
Zn-substrate	10%	1	10	1	3	1	3	1	3
Ca-substrate	20%	1	10	1	3	1	3	1	3

www.manaraa.com

3.2.3 In-situ Lab simulation of DPF thermal conditions

The heat treatment of the prepared cordierite substrate samples was carried out under temperatures ranging from 300-1100ºC. A section of sample was cut from each doped cordierite substrate sample. A section of substrate was also cut from a clean, undoped (blank) cordierite substrate sample. The sections of cut substrate were approximately 3 channels by 3 channels (0.4 cm by 0.4 cm) in size, and weighed approximately 0.5grams. The sample was heated in a thermogravimetric analyzer (TG209, NETZCH) to hold temperatures of 300ºC, 500ºC, 900ºC, and 1100ºC. The TGA heating rate was 25K min^{-1} in an atmosphere of high purity nitrogen, which was set to a flow rate of 25 ml min^{-1}.

Once the TGA cooled down to room temperature, the sample was removed and rinsed by dehydrated ethanol in an ultrasonic bath. This additional step of dehydrated ethanol and ultrasonic cleaning was intended to remove any residual chemicals which did not react with the cordierite surface. Once removed from the ethanol, the samples were dried in an oven at a temperature of 105ºC for 24 hours. It should be noted that a separate cordierite sample was used for each temperature condition and time of exposure. Therefore, with one pristine sample and three different chemical solutions (sodium

www.manaraa.com

carbonate, iron sulfate, and potassium phosphate), four different temperature conditions (300ºC, 500ºC, 900ºC and 1100ºC).

3.2.4 SEM, WDS and XRD analysis of Cordierite substrate aging samples

3.2.4.1 SEM analysis of cordierite substrate aging samples

The surface microstructures of the thermal-chemically treated cordierite samples were characterized by a Hitachi 4300 SEM. Prior to SEM analysis, the samples were coated with iridium and palladium. Samples were placed on a metal stand and anchored to the stand by double sided carbon tape. The surface microstructures of thermal-chemically treated samples were compared to pristine cordierite samples.

3.2.4.2 Element Distribution by EPMA

Each cordierite sample was placed standing vertically (channel walls running vertically) then embedded into an epoxy resin. The epoxy resin was allowed to cure for 24 hours. After curing, the epoxy resin bound sample was then ground and polished with 6 µm and 3 µm diamond paste coated polishing pads. An additional fine polish process was carried out utilizing a 1 µm polishing pad with aluminum oxide paste. The aluminum oxide powder was first dispersed in dehydrated ethanol, prior to use in the fine polishing process. The cross-sectional distribution of elements was appraised with WDS (JXA-8900, Japan). The cordierite porosity was calculated via adjusting the threshold color of the BSE images using

www.manaraa.com

Image J2X (National Institutions of Health, US). Select one area on the BSE images and the contrast of the original image is automatically enhanced and black pixels after adjustment indicate the porosity. The equation is shown as:

$$Porosity\ (\%) = S_p / S_T \quad (1)$$

S_p: *Porous area*

S_T: *Total area*

The average cross-section element concentrations were calculated by converting the entire scanning area element concentration including the pore area, which were read directly from the WDS, to cordierite cross-section element concentration based on J2X. The equation is shown as:

$$Concentration\ (\%) = C_1 / \mu \quad (2)$$

$\mu = S_c / S_s$

C1: element concentration read from WDS

μ: *cordierite substrate area fraction based on J2X*

S_c: *cordierite substrate area*

S_s: *entire scanning area*

3.2.4.3 XRD analysis of cordierite substrate aging samples

www.manaraa.com

XRD was utilized to characterize the physico-chemical properties of doped and pristine cordierite substrate samples to reveal the crystalline phases change before and after the thermal-chemical treatment. Samples for XRD analysis were prepared by grinding the TGA thermal-chemical treated cordierite samples using a mortar and pestle. The ground powder samples were appraised via x-ray diffraction (MiniFlex, Rigaku). The XRD analyses were carried out under electric voltage/current of 30kV/15 mA. The scanning angle ranges from 10-90^{o} with the scanning step of 0.01^{o}.

3.3. Results and Discussions

3.3.1 SEM cordierite substrate characterization after thermal-chemical exposure

SEM images of undoped (pristine) cordierite substrate heat treated for 1 hour at elevated temperatures are shown in Figure 3.1. Cordierite substrate doped with iron, sodium, and potassium heat treated for 1 hour at elevated temperatures are shown in Figures 3.2, 3.3, and 3.4. Substrate doped with Ca and Zn are shown in Figure 3.8, 3.9, 3.10, 3.11. Doped cordierite samples exposed to increased time of exposure are shown in Figures 3.5, 3.6, and 3.7. The pristine cordierite samples shown in Figure 3.1 did not show melting, cracking lines, even when exposed to 1100^{o}C. The cordierite original layer structures did not disappear until 900^{o}C, and the small cordierite pieces started to melt together at 1100^{o}C.

www.manaraa.com

The cordierite substrate exposed to iron does not show any melting after exposure to 300ºC, as the cordierite surface contains the same layer structures, as shown in Figure 3.2. After exposure at 500ºC, when exposed to iron, the cordierite surface begins to melt. Iron oxide particles only appear to begin to bind with the cordierite, but have not yet fully started to melt at 500ºC. At 900ºC, the iron oxide particles have started to sinter the cordierite substrate and change the layer structure into a glaze-like surface. Previous studies indicate iron catalyzed melting of cordierite at temperatures of 1200ºC (Scardi P. 1994). The inconsistence with the results herein and with previous studies is due to the ash components utilized. The Scardi study used $FeCl_3$ as the iron source, herein the authors used $FeSO_4$ which decomposes at 300ºC, which is much lower than the melting point for Fe_3O_4 at 1597ºC (Perry D.L. 1995). The thermal expansion coefficient for cordierite substrate is 0.7x 10^{-6}ºC^{-1} at room temperature and 2.5x 10^{-6}ºC^{-1} at 650ºC whereas the iron-reacted substrate, which forms spinel (See XRD discussion), is 8.8x 10^{-6} ºC^{-1} (Lachmann I.M. 1981, Perry D.L. 1995). The difference of thermal expansion coefficients between the glaze-like surface and the surrounding un-reacted substrate leads to cracking (Dario M.T. 1998, Montanaro L. 1994). At 1100ºC, nearly the entire substrate surface reacts with iron to produce a glaze-like surface. At this stage, the substrate has also lost its permeability. If this cordierite substrate were to be in autocatalyst application, the lack of open pores inside

www.manaraa.com

the monolith channel would increase the restriction of exhaust gas passing through the substrate walls. Figure 3.5 shows when the iron doped cordierite substrate is heated to 900ºC, after 30 minutes of exposure slight melting of the cordierite surface begins. The iron doped cordierite surface shows more melting after 1 hour and 3 hour exposure, when compared to only 30 minutes of exposure at 900ºC.

Figure 3.3 shows the cordierite substrate doped with potassium was susceptible to catalyzed formation of a glaze-like structure at 300ºC. When the potassium doped substrates was exposed to 900ºC and 1100ºC, there was cracking distributed throughout the entire substrate area. Figure 6 shows when varying the time of heat treatment at 900ºC, the potassium doped cordierite held at 900ºC for 30 minutes did not appear to produce any melting or cracking. However, when exposed to 900ºC for 1 hour or 3 hours, the surface of the potassium doped cordierite shows both melting and cracking.

Figure 3.4 shows the cordierite substrate doped with sodium started forming a glaze-like structure after 1 hour at 300ºC. This is a similar result to the potassium doped substrate as shown in Figure 3.3. The degradation of sodium doped cordierite initiating at temperatures of 300ºC, reported herein, is lower than the 500ºC reported in a previous study – but 500ºC was the lowest temperature investigated in a previous study (Bachiorrini A. 1996). After heat treating the cordierite for 1 hour at both 900ºC and 1100ºC, the sodium

www.manaraa.com

doped cordierite substrate showed cracking. At 1100ºC the cracking appeared to be more severe than at 900ºC, as individual cracks were larger. Figure 3.7 shows when exposed to 900ºC for 30 minutes, the presence of sodium altered the cordierite structure and severe cracking is visible. After exposure for 3 hours, the cracked area has grown to be a large void space in the cordierite substrate.

Figure 3.8, 3.9 shows that the Zn and cordierite degradation occurs at temperatures above 900ºC. When Zn treated cordierite was exposed to 300ºC and 500ºC, the layer structures of cordierite substrate were covered by zinc phosphate, as indicated by EDS spectrum, which clearly show the zinc phosphate peaks (Figure 8). At 300ºC and 500ºC, the reaction between zinc phosphate and cordierite substrate does not create noticeable changes to the structure of the porous substrate. However, at 1100ºC, the cordierite surface has undergone changes which have increased the porosity and induced localized cracking (Figure 3.8). The chemical reaction process begins when ZnO first attaches to the surface and induces localized surface melting. The stresses induced by melting further changes the cordierite substrate and create cracking lines as indicated in Figure 3.8. The EDS spectrum indicated the area around cracks show ZnO peaks, which suggest that ZnO catalyzes localized cracking at 1100ºC.

www.manaraa.com

With respect to the time of thermal treatment, the authors assessed Zn doped cordierite treated at 1 hour and 10 hours at 300°C (Figure 3.9). There appears to be no changes to the surface or microstructure of the cordierite, with respect to time at 300°C as indicated in Figure 3.3. Prolonged thermal treatment (3 hours), has a significant impact on the cordierite surface structure as zinc phosphate react with cordierite substrate to form glaze-like structure, when compared to treatment at 900°C for 1 hour. In addition, the glaze like structures were likely to crack due to the difference in thermal expansion coefficient of cordierite ($2.5x10^{-6}$/°C) and spinel ($0.9x10^{-6}$/°C) as indicated by XRD profiles (Perry D.L. 1995). With further increased temperatures to 1100°C, the cracking lines tend to break apart, amplifying void space between the cordierite (Figure 3.9). The EDS spectrum confirmed the reaction between cordierite and zinc phosphate, indicating the presence of Zn at melting and cracked locations.

Cordierite samples doped with calcium oxide were thermally treated and the cordierite showed no change until 1100°C (Figures 10 and 11). Specifically, the layer structure of cordierite surface showed slightly glaze-like structure at 1100°C. Despite the glaze-like structure, the cordierite substrate exposed to calcium did not show any cracking, melting, or structural changes when exposed to 1100°C for 1 hour. Further, the corresponding EDS spectrum indicates the surface is covered by CaO, suggesting that the

www.manaraa.com

chemical reaction between CaO and cordierite possesses much slower kinetics, when compared to zinc. When exposed to 300ºC for 10 hours the cordierite did not show any changes. However, when exposed to 500ºC for 3 hours, the cordierite surface started to produce slight melting structure. The effects of melting became more severe from 500ºC to 1100ºC as indicated in Figure 3.5. Negro's research confirmed the results herein, in that calcium doped cordierite substrate showed fused areas above 1000ºC (Negro A. 1993). Furthermore, the cordierite substrate tends to possess lower porosity at temperatures of 1100ºC as cordierite further reacts with CaO, fusing the layers structure together (Figure 3.11).

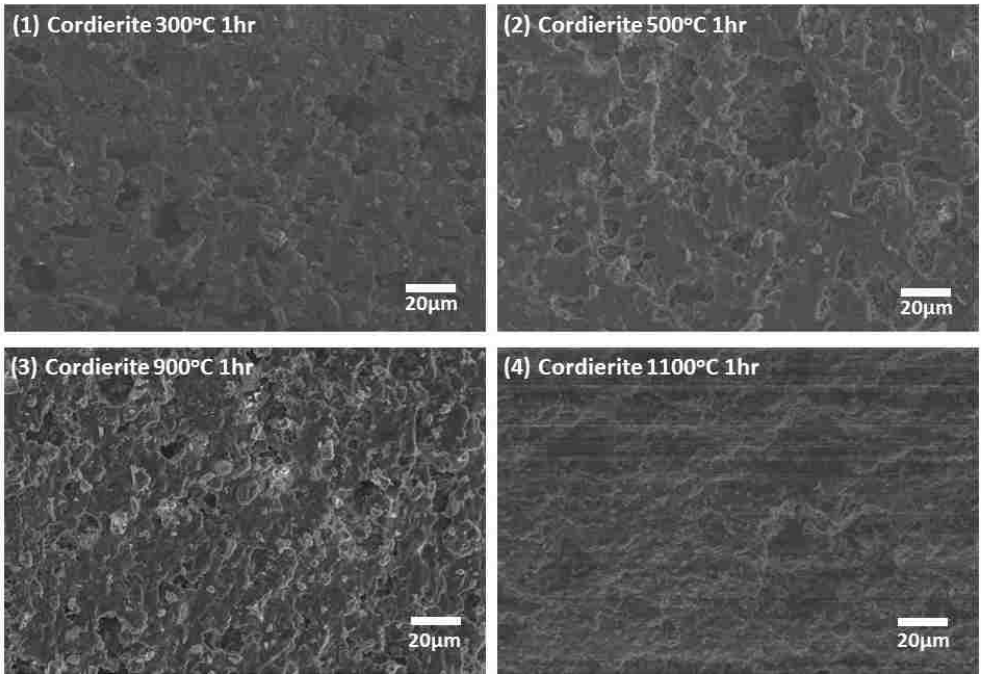

Figure 3.1 Pristine (blank) cordierite substrate heat treated for 1 hr. with increase temperature (300ºC, 500ºC, 900ºC and 1100ºC)

www.manaraa.com

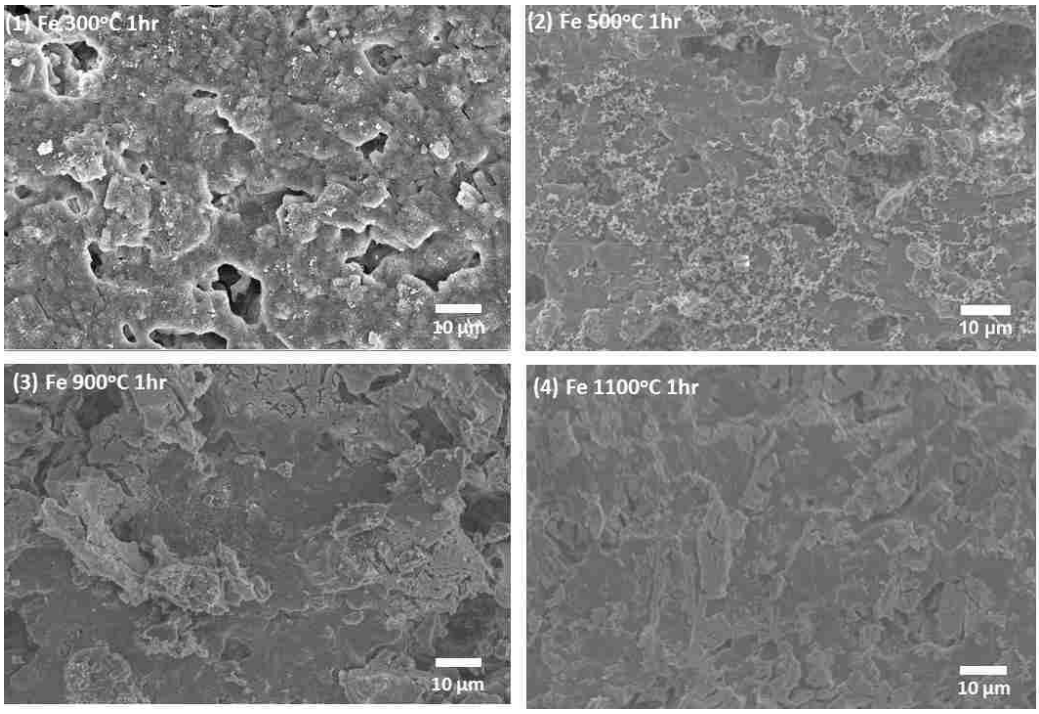

Figure 3.2. Iron doped cordierite substrate heat treated for 1 hr with increase temperature (300°C, 500°C, 900°C and 1100°C

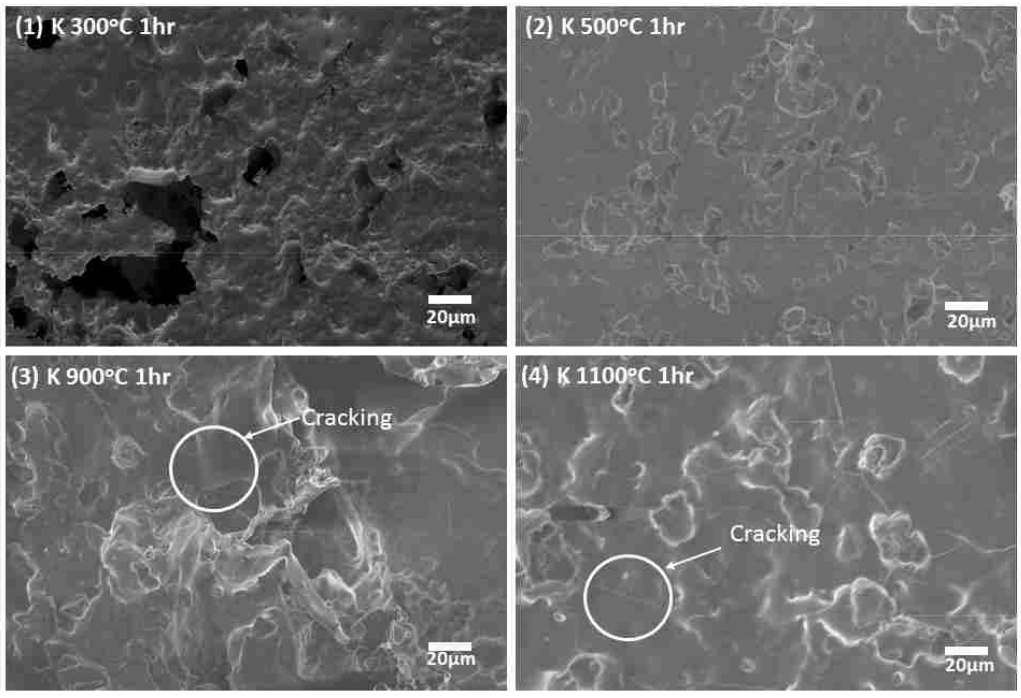

Figure 3.3. Potassium doped cordierite substrate heat treated for 1 hr with increase temperature (300°C, 500°C, 900°C and 1100°C)

www.manaraa.com

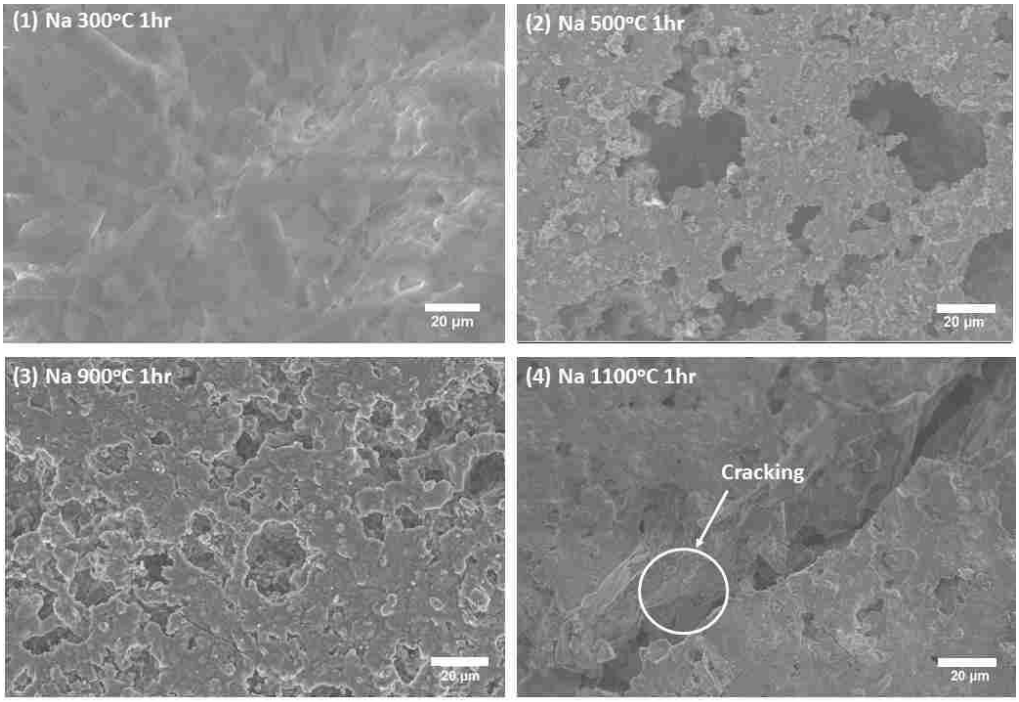

Figure 3.4. Sodium doped cordierite substrate heat treated for 1 hr with increase temperature (300°C, 500°C, 900°C and 1100°C)

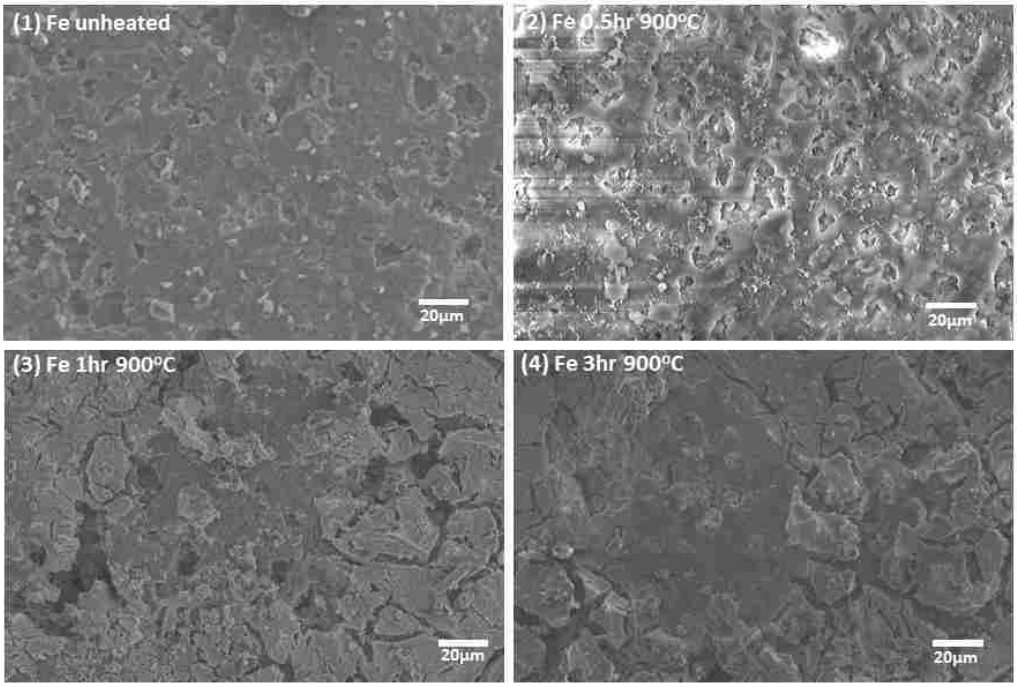

Figure 3.5. Iron doped cordierite substrate heat treated at 900°C with increase aging time (0, 30min, 1 hr, 3hr)

www.manaraa.com

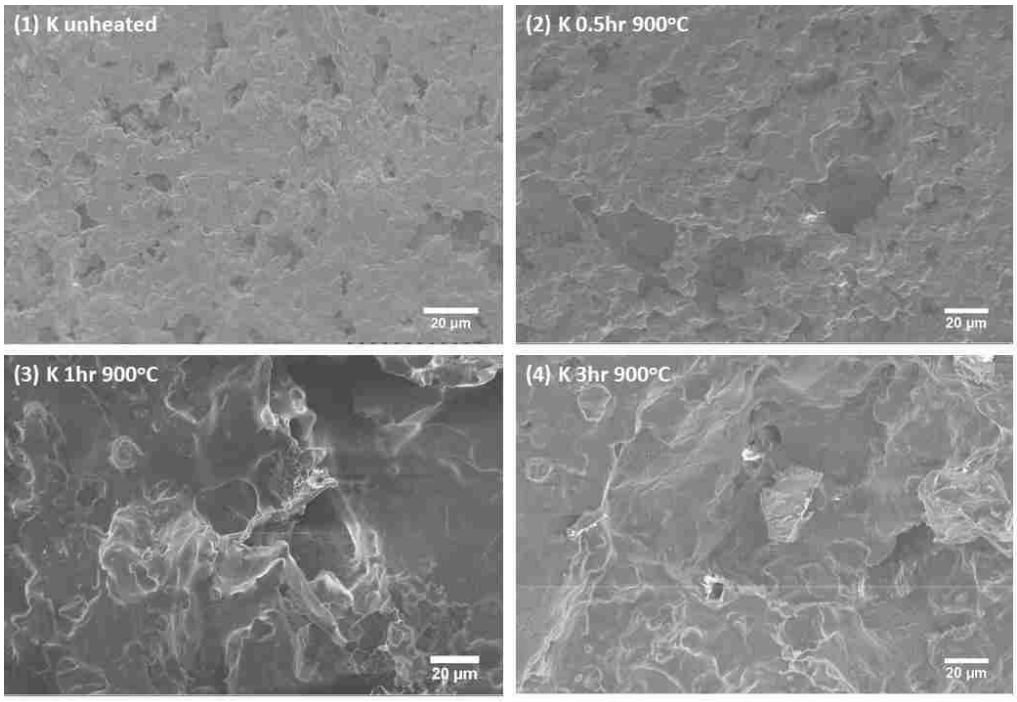

Figure 3.6. Potassium doped cordierite substrate heat treated at 900°C with increase aging time (0, 30 min, 1 hr, 3hr)

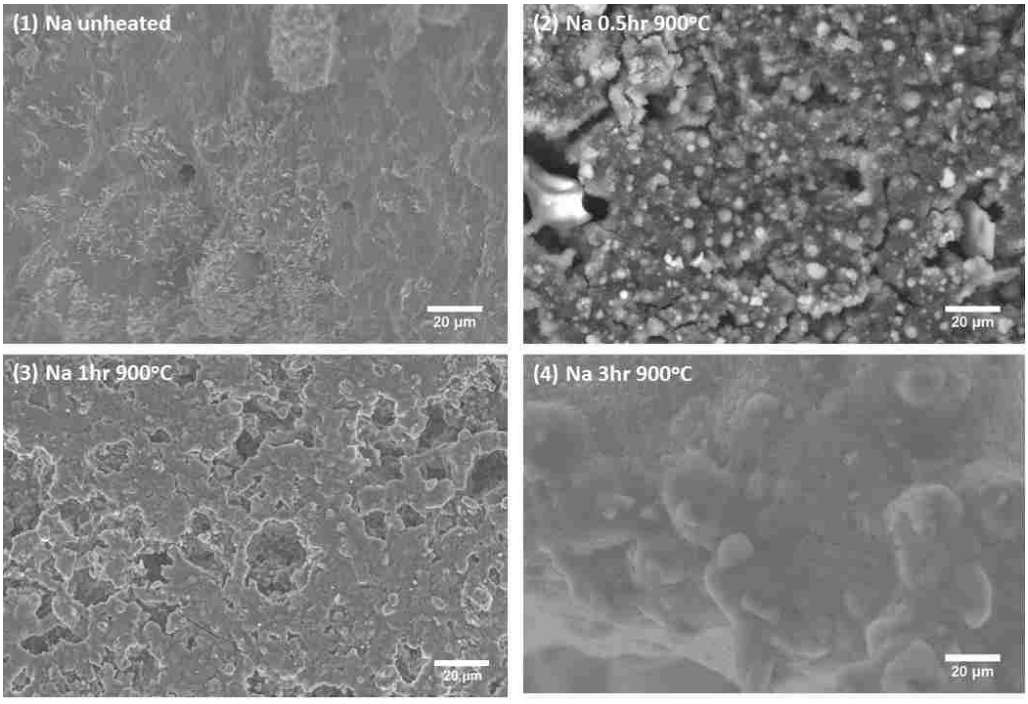

Figure 3.7. Sodium doped cordierite substrate heat treated at 900°C with increase aging time (0, 30 min, 1 hr, 3hr)

www.manaraa.com

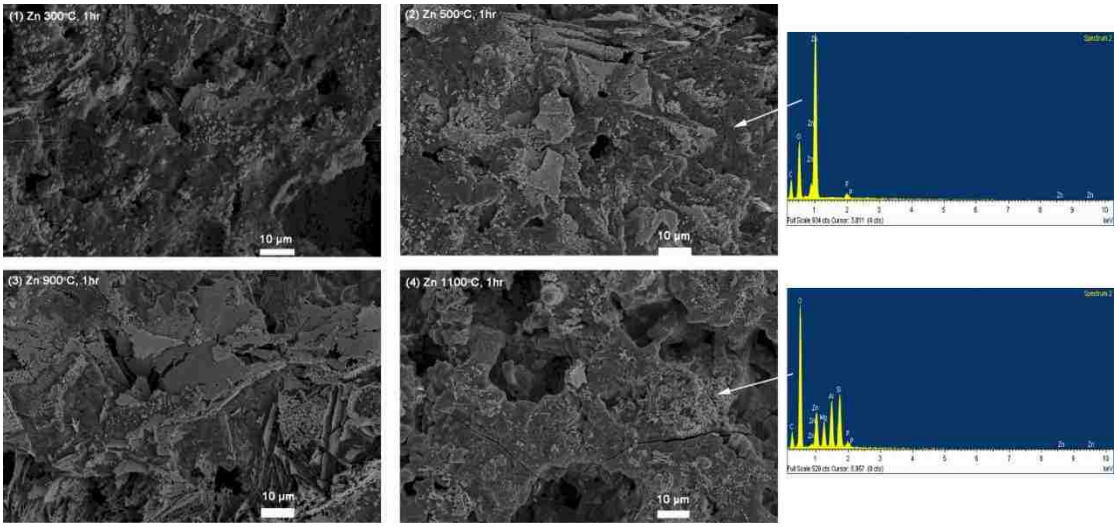

Figure 3.8. SEM-EDS analysis of Zn doped cordierite under variable temperatures for 1 hour (300ºC, 500ºC, 900ºC and 1100ºC).

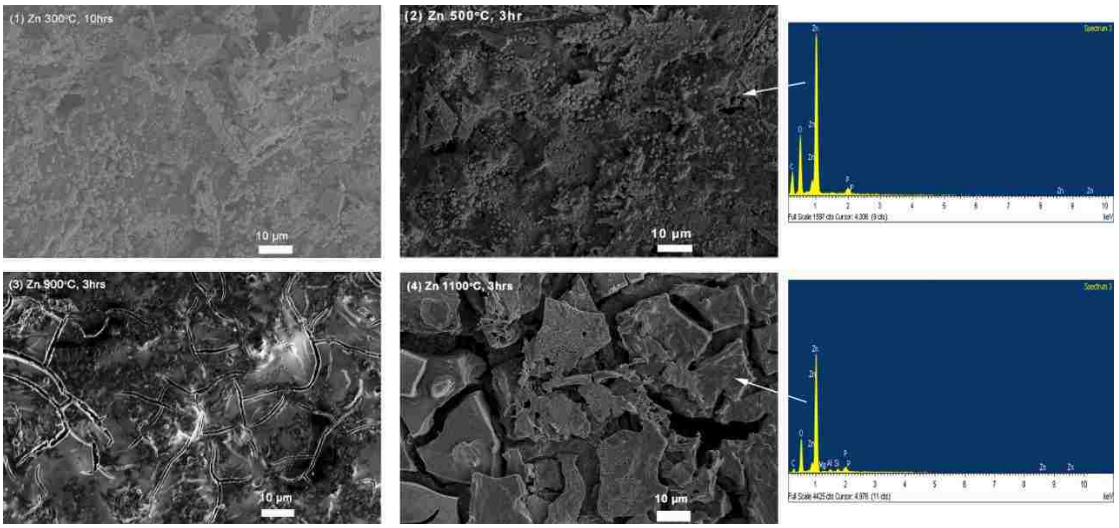

Figure 3.9. SEM-EDS analysis of Zn doped cordierite under variable temperatures (300ºC, 500ºC, 900ºC and 1100ºC) with extended time of exposure (3 hours and 10 hours).

www.manaraa.com

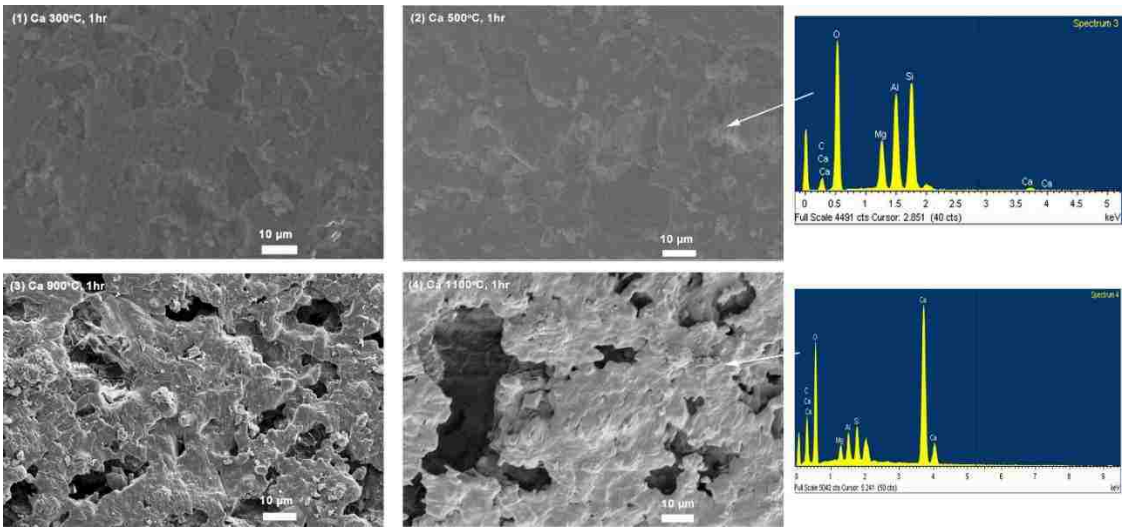

Figure 3.10. SEM-EDS analysis of Ca doped cordierite under variable temperatures for 1 hour (300°C, 500°C, 900°C and 1100°C).

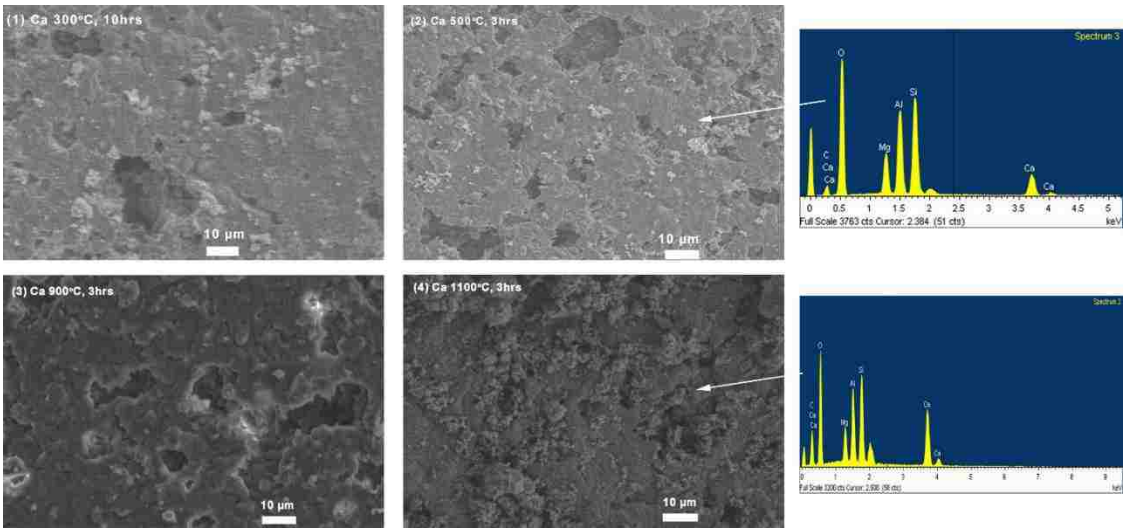

Figure 3.11. SEM-EDS analysis of Ca doped cordierite under variable temperatures (300°C, 500°C, 900°C and 1100°C) at with extended time of exposure (3 hours and 10 hours)

3.3.2 EPMA Analysis of the Accumulation and Corrosion Pathways

3.3.2.1 Iron Migration and Corrosion

www.manaraa.com

The migration and corrosive pathway for Na, K, Fe, Zn and Ca ash in cordierite substrate was investigated through analyzing the distribution of ash chemicals within cordierite substrate cross-sections using EPMA. Figure 3.12a-e shows the cross section of Fe-doped cordierite samples. Figure 3.13a-e shows the cross section of Na-doped cordierite samples. Figure 3.14a-e shows the cross section of K-doped cordierite samples. Figure 3.15a-e shows the cross section of Zn-doped cordierite samples. Figure 3.16a-e shows the cross section of Ca-doped cordierite samples. The color bar indicates the difference in element concentration with the blue color indicating the lowest concentration of background and white color indicates the highest concentration.

The porosity of each treated substrate was estimated by selecting three area from the image and adjusting the color threshold of BSE images with Image J2X. Then the porosity was calculated by equation 1. The average porosity of the five elements are presented in Figure 3.19 and 3.20.

Figure 3.12 demonstrates that Fe migration in cordierite substrate increases as a function of temperature. As observed through elemental mapping in Figures 3.12a and 3.12b, the Fe first attaches to the cordierite substrate surface under low temperatures of 300ºC and 500ºC without migrating into the cordierite substrate inner structure. At these low temperatures, the migration of Fe is limited to the surface of the cordierite substrate.

www.manaraa.com

Figure 3.12c shows that as the heat treatment temperature is raised to 900ºC, the Fe migrates into the cordierite substrate through pores. Figure 3.8d shows that as the heat treatment temperature increased to 1100ºC, the concentration of migration into the pores also increased.

At temperatures above 900ºC, iron becomes well distributed in the cordierite substrate. The Fe migration and corrosion process becomes more intense with temperatures higher than 900ºC. These temperatures can be reached during uncontrolled regeneration in a diesel particulate filter. The lines formed on the surface of the cordierite, indicate cracking, which is likely due to the difference in thermal expansion coefficients, between cordierite substrate and other crystalline phases, more specifically $0.7x10^{-6o}C^{-1}$ for cordierite and ($8.8x10^{-6}$ ºC^{-1}) for spinel (Lachmann I.M. 1981).

To confirm the corrosive procedure, the substrate slice was held at 1100ºC for 3 hours. The results are provided in Figure 3.12e and show the iron doped substrates held at 1100ºC for 1 hour and 3 hours do not have a significant difference in Fe distribution. The average concentration of Fe within the cordierite substrate increases with temperature, specifically; 0.078% for 300ºC, 1.08% for 500ºC, 1.33% for 900ºC and 3.24% for 1100ºC 1hr and 1.62% for 1100ºC 3hrs (Figure 3.19). The increased iron concentration confirms that elevated temperatures can facilitate the corrosive process. When studying the back-

www.manaraa.com

scattering images in Figure 3.12a-e, there is only minor cracking that occurs within the cordierite substrate cross-section sample. The porosity of iron doped cordierite in Figure 3.17 appears first to increase with temperature, peak at 900ºC, and then decrease with temperature. This was suggested in previous research by Negro (1993) that the cordierite first occurred cracking, increase porosity and then melting decreases porosity (Negro A. 1993).

www.manaraa.com

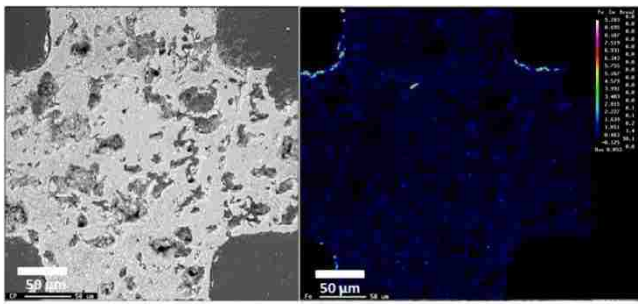

12a. Fe intensity in cordierite substrate heat treated at 300oC for 1hr.

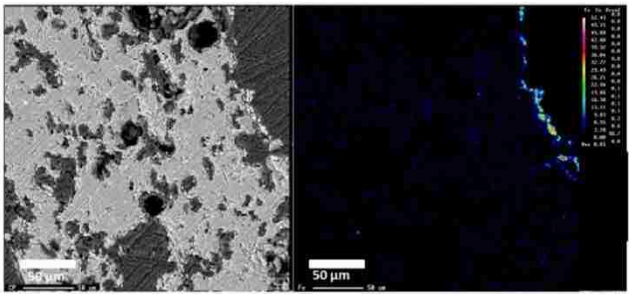

12b. Fe intensity in cordierite substrate heat treated at 500oC for 1hr.

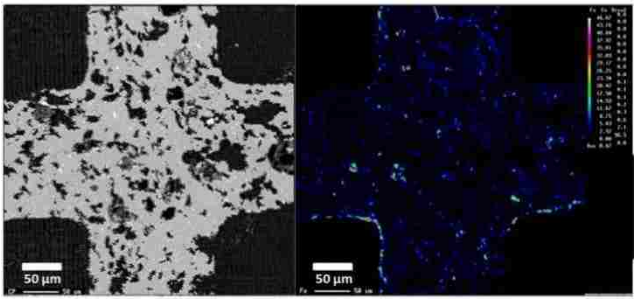

12c. Fe intensity in cordierite substrate heat treated at 900°C for 1hr.

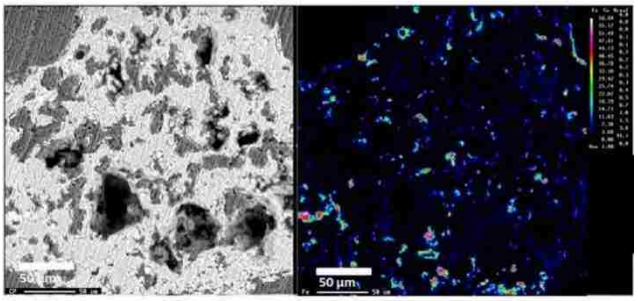

12d. Fe intensity in cordierite DPF heat treated at 1100°C for 1 hr.

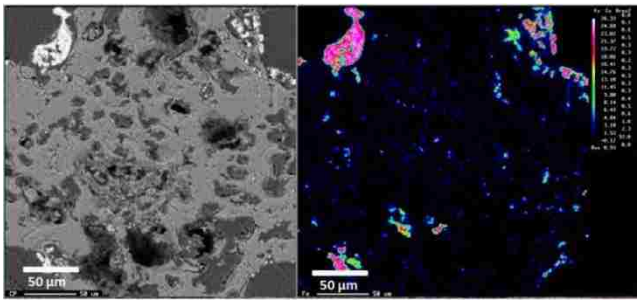

12e. Fe intensity in cordierite substrate heat treated at 1100°C for 3 hrs.

Figure 3.12a-e. EPMA mapping of Iron intensity in cordierite substrate

www.manaraa.com

3.3.2.2. Sodium Migration and Corrosion

Figure 3.13a-e illustrates the pathway of Na migration and corrosion in the cordierite substrate. Figure 3.13a shows there appears to be no negative effects on the cordierite after heat treating the Na doped substrate for 1 hour at 300ºC, as Na stays on surface of substrate without migrating inwards. However, Figure 3.13b shows that when heat treating the sodium doped substrate at 500ºC, the Na begins to migrate and corrode the substrate. Figure 3.13c shows that at increased temperatures above 900ºC, it appears that Na followed the cordierite porous structure, penetrating into the substrate. The specific corrosion phenomena are confirmed by XRD patterns in Figure 3.16, as the substrate crystalline phase shifts to sodium spinel ($NaAl_5O_8$) at 900ºC. Figure 3.9d shows that when heat treating the doped substrate for 1 hour at 1100ºC, the Na concentration and corrosion process intensifies as reactions lead to several new crystalline phases including nepheline. This is also shown in Figure 3.17 (see discussion in Section 3.3). The average Na concentration in the samples are; 0.19% at 300ºC, 1.39% at 500ºC, 2.04% at 900ºC, 4.86% at 1100ºC for 1hr and 4.98% at 1100ºC for 3hrs. Therefore, the Na migration and corrosion intensifies after the temperature reached 900ºC (Figure 3.19).

In addition, Figures 3.13c and 3.13d show the sodium induces cracks in the cordierite at both 900ºC and 1100ºC. The cross-section area covered by Na was increased

www.manaraa.com

which means the Na migration and corrosion increased between 300ºC and 500ºC, and intensified as the heat treatment temperature reached above 900ºC. Compared to the SEM photographs shown in Figure 1, the presence of Na leads to cracking of the cordierite substrate not only on the surface, but also within the substrate.

Herein, we found substrate cracking beginning at 900ºC. This heat treatment temperature result is lower than previous reported studies which indicate cracking started at 1000ºC (Bianco R. 1989). Figure 3.13d and 3.13e shows the Na migration and corrosion pathway, as after 3 hours of heat treatment at 1100ºC the Na follows the porous structure of the substrate through the majority of the cross-section compared to just 1 hour of exposure at 1100ºC. Therefore, when considering sodium, both temperature and time have significant impact on Na migration and corrosion of the cordierite substrate.

Figure 3.17 shows that porosity of the sodium doped cordierite decreases with the increase of thermal treatment temperature. These results suggest that compared to Fe doped cordierite, sodium doped cordierite corroded with a higher intensity, result in melting of the cordierite substrate and starting at lower temperature.

www.manaraa.com

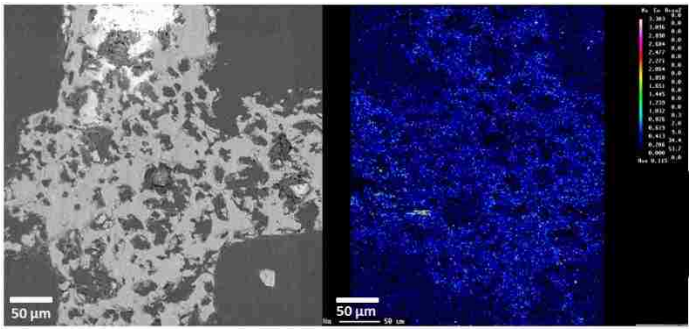

13a. Na intensity in cordierite substrate heat treated at 300°C for 1 hr.

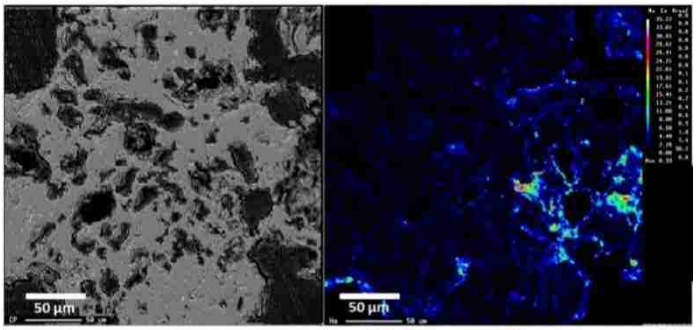

13b. Na intensity in cordierite substrate heat treated at 500°C for 1 hr.

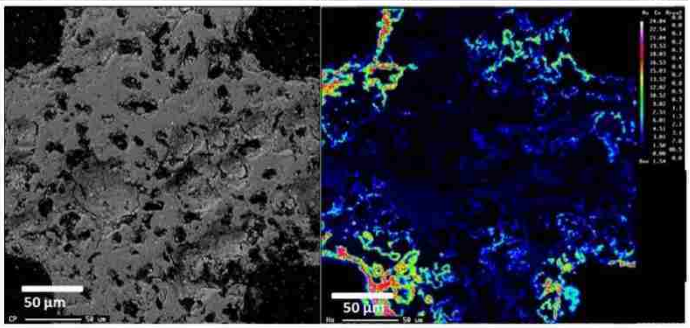

13c. Na intensity in cordierite substrate heat treated at 900°C for 1 hour.

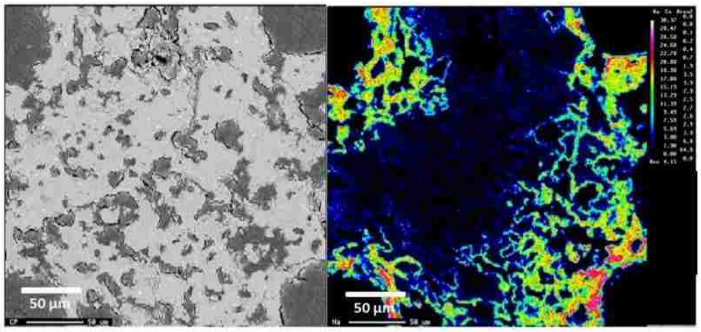

13d. Na intensity in cordierite substrate heat treated at 1100°C for 1 hr.

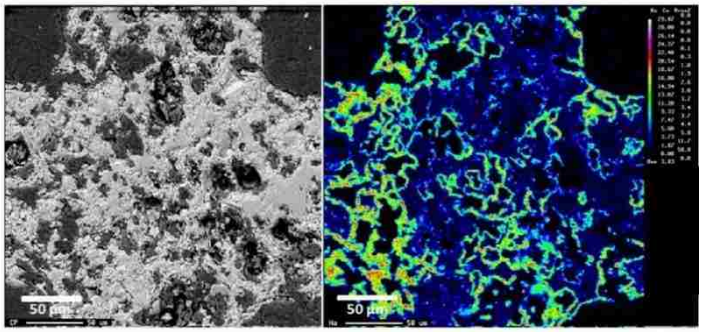

13e. Na intensity in cordierite substrate heat treated at 1100°C for 3 hrs.

Figure 3.13a-e. EPMA mapping of sodium intensity in cordierite substrate.

www.manaraa.com

3.3.2.3. Potassium Migration and Corrosion

The potassium interaction with the cordierite substrate at increasing temperature and time is illustrated in Figures 3.14a through 3.14e. Figure 3.14a shows that after heat treating the K doped cordierite for 1 hour at 300ºC, the K attached to the edge of the substrate. Figure 3.14b shows the K migrated into the cordierite substrate starting at temperatures of 500ºC, by following the porous structural network. This is similar to the Na migration, as shown in Figure 3.13b. As the temperature of exposure increased to 900ºC, the area of substrate corroded by potassium increased. When exposed to 1100ºC, as shown in Figure 3.14d, the potassium was distributed throughout the entire cross-sectional area, with the concentration of 3.83%. Additionally, the potassium saturated area begins in isolated areas, and as the temperature increases these isolated areas begin to link to each other, eventually covering the entire substrate cross-section. The concentration of K on the samples are measured as; 0.81% at 300ºC, 1.65% at 500ºC, 1.48% at 900ºC, 3.83% at 1100ºC for 1hr and 4.92% at 1100ºC for 3hrs (Figure 19).

The back-scattering images in Figure 3.14a-e show the K saturated areas were distinguished as white phases on the substrate in the image shown in the left frame of Figure

www.manaraa.com

3.14e, which corresponded to the high concentration areas of K in the WDS image in the right frame of Figure 3.14e.

Figure 3.14d shows the potassium doped substrate tends to corrode by melting instead of cracking when exposed for 1 hour at 1100°C. The XRD patterns for the heat-treated K doped substrate, further confirmed the WDS results indicate potassium catalyzed melting, as cordierite XRD peak intensities reduced under 1100°C. This indicates less amorphous structures due to melting (see discussion in Section 3.3). Overall, both Na and K behaved similarly, by inducing corrosion not only on the substrate surface, but also migrating into and throughout the entire substrate channel wall. Potassium doped cordierite porosity results in Figure 3.17 show the same tendency to decrease porosity as Na, with increased thermal treatment temperature, the cordierite tends to melt together to form large glaze-like pieces, further reducing the porosity.

www.manaraa.com

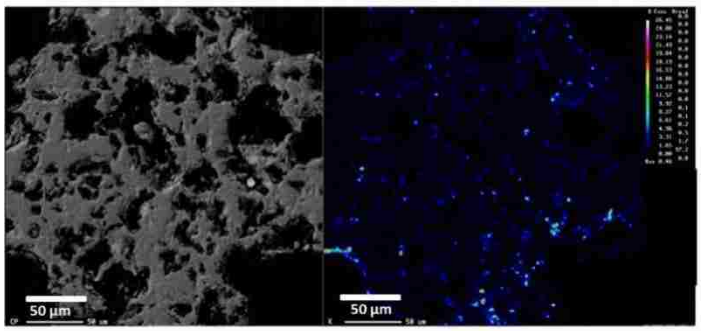

14a. K intensity in cordierite substrate heat treated at 300oC for 1 hr.

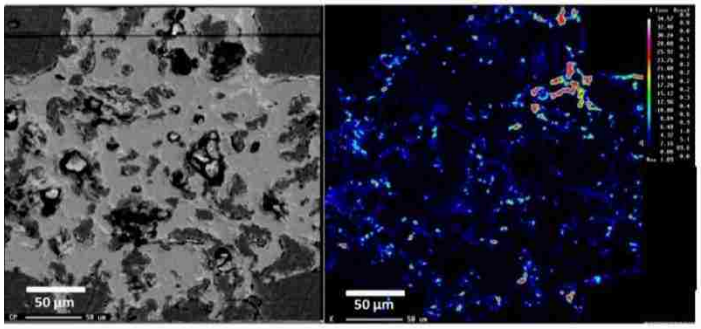

14b. K intensity in cordierite substrate heat treated at 500°C for 1 hr.

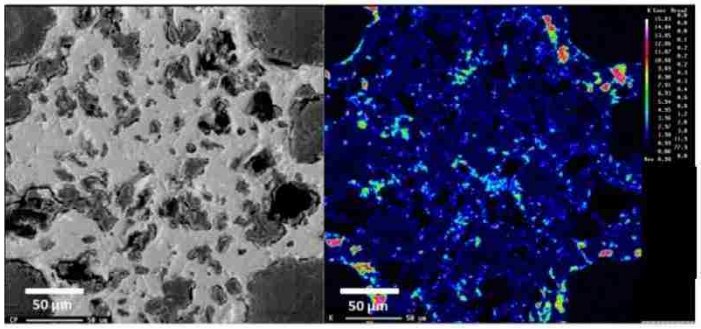

14c. K intensity in cordierite substrate heat treated at 900°C for 1 hr.

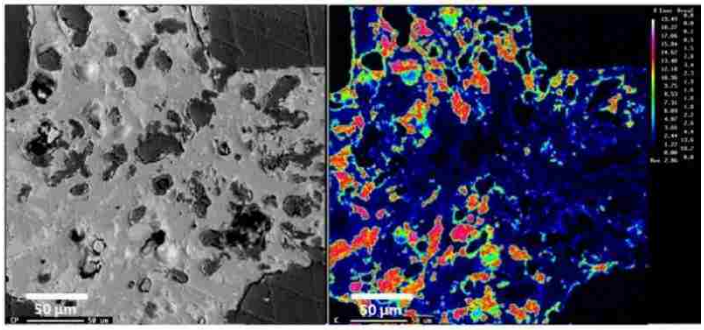

14d. K intensity in cordierite substrate heat treated at 1100°C for 1 hr.

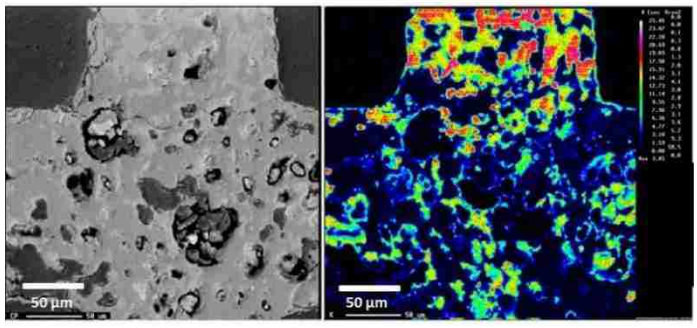

14e. K intensity in cordierite substrate heat treated at 1100°C for 3 hrs.

Figure 3.14a-e. EPMA mapping of potassium intensity in cordierite substrate.

www.manaraa.com

3.3.2.4 Zinc migration and corrosion

As observed through elemental mapping, zinc first accumulated on the surface of the porous cordierite substrate under lower temperature of 300ºC, Figure 3.15a. With increased exposure to 500ºC, the zinc diffused into the internal pores of the cordierite as it reacted (Figure 3.15b). However, considering the BSE image, high concentrations of zinc still accumulated only on the edge of the porous structure with much lower concentration of zinc detected in the bulk cordierite, than was observed at 500ºC and 900ºC. At 1100ºC, the zinc that accumulated on cordierite surface was well distributed within the cross-section and the bulk cordierite, which suggested that zinc-cordierite reaction became more intense (Figure 3.15d). Further, the zinc corrosion pathway follows the pores of the cordierite.

The BSE images of the zinc doped cordierite substrate shows a decrease in porosity with increasing in temperature, which indicates the reaction between cordierite and zinc results in melting and consolidation of the cordierite substrate (Figures 3.15a-d). Further, the porosity was quantified in reducing from 30% to 12%, at 300ºC and 1100ºC, respectively (Figure 3.18). Additionally, the quantified averages of cross-sectional zinc concentrations are presented in Figure 3.20. The zinc concentrations increase with

www.manaraa.com

temperature from 0.71% Zn, 0.977% Zn, 1.022% Zn, and 1.072% Zn; for 300°C, 500°C, 900°C and 1100°C, respectively. The increased zinc concentration confirms that elevated temperatures can facilitate the corrosive process, specifically melting and consolidation of cordierite occurs. In addition, it appears that at 1100°C the cracking process has occurred in the BSE image.

www.manaraa.com

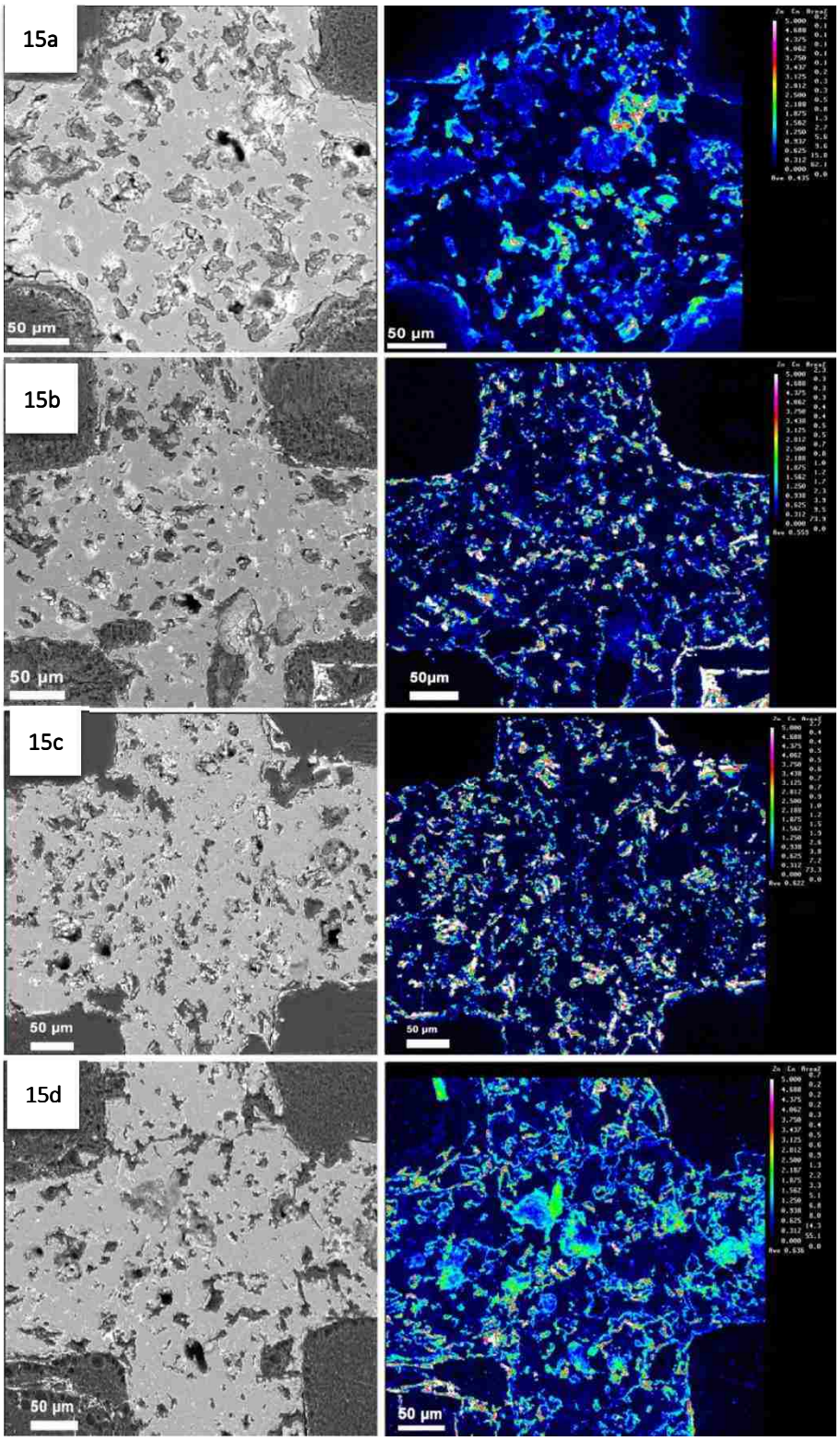

Figure 3.15. EPMA mapping analysis of cordierite cross-section doped by zinc phosphate at elevated temperature 3.15a-d for 300°C, 500°C, 900°C and 1100°C under 1hour.

www.manaraa.com

3.3.2.5Calcium migration and corrosion

The interaction of calcium accumulation and cordierite are illustrated in Figures 3.16a-d. In these figures, the white spots of calcium remain on the cordierite substrate, and do not appear to intermingle with the cordierite cross-section. This is quite different than zinc, as the zinc comingled with the cordierite and was colorimetrically ubiquitous in the cross-section. It appears that the observed calcium concentration shows a very slight increase with increasing temperature from 500ºC to 1100ºC (Figure 3.16b-d). Even at 1100ºC, the calcium is still accumulated on the surface without penetrating into the depth of the substrate – suggesting that the calcium and cordierite interactions are minor. Considering the high concentration of calcium in DPF ash the cordierite does not show significant signs of degradation from calcium during vehicle operating conditions or regeneration (Ibrahim N. 2011). However, the thermal expansion coefficient does show significant change as temperature increase to 500ºC (Johnson R. 2003). However, other alkaline metals such as Na and K accumulate on cordierite substrate at much lower concentrations, and these alkalis could lead to melting and cracking based on previous research (Montanaro L. 1994). Further, the cross-section porosity remains stable in the presence of calcium from 300ºC to 900ºC, and only appears to very slightly decrease at 1100ºC (Figure 3.18). In addition,

www.manaraa.com

the average elemental concentration of calcium is stable in the presence of cordierite, as indicated in Figure 3.20. The average cross-sectional calcium concentration is 0.246%, 0.26%, 0.24% and 0.298% for the entire temperature range of 300ºC to 1100ºC (Figure 3.20), which suggests that the calcium does not comingle with cordierite to the extent that Zn does.

www.manaraa.com

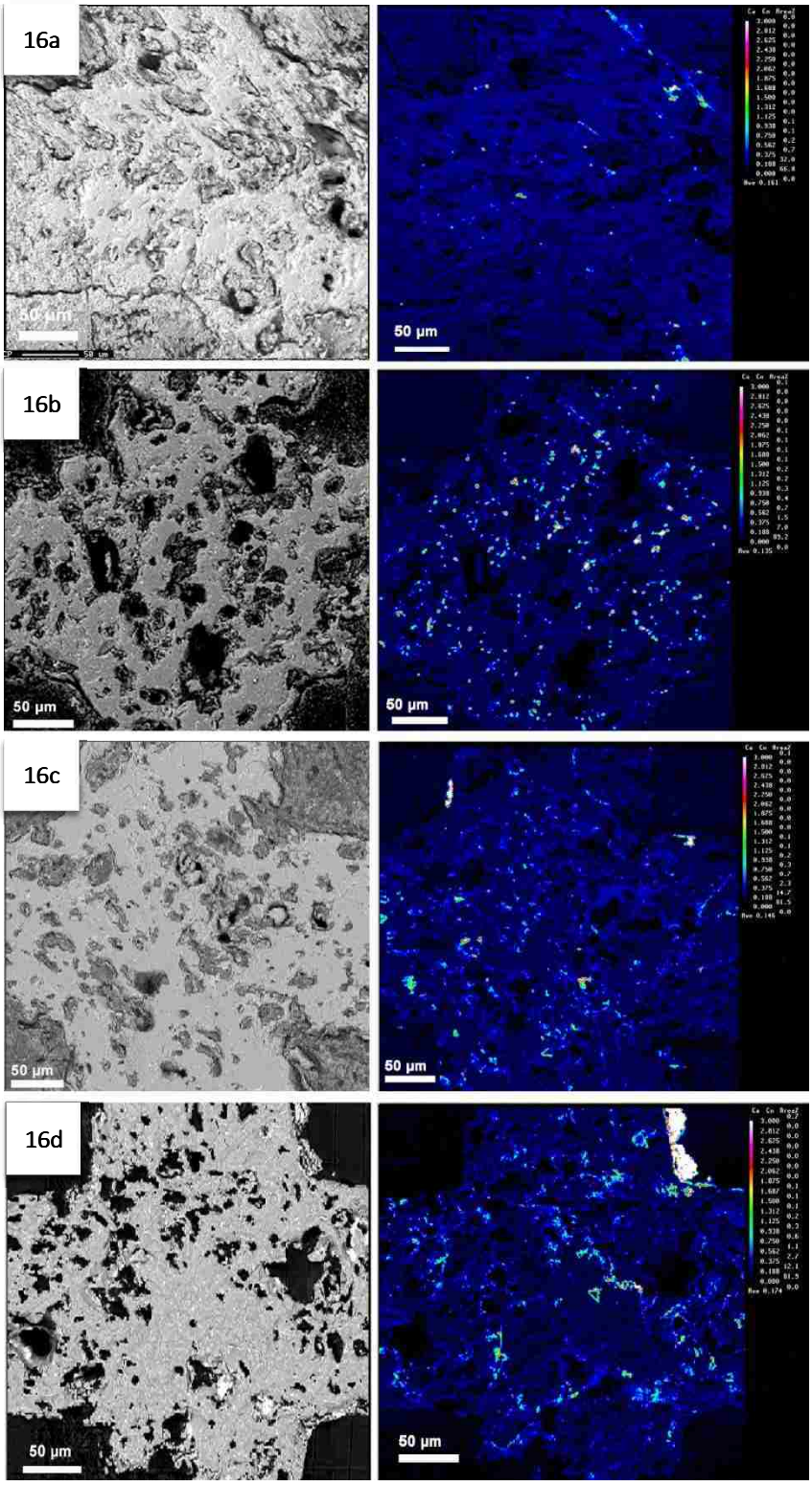

Figure 3.16. EPMA mapping analysis of cordierite cross-section doped by calcium acetate at elevated temperature 3.16a-d for 300°C, 500°C, 900°C and 1100°C under 1hour.

www.manaraa.com

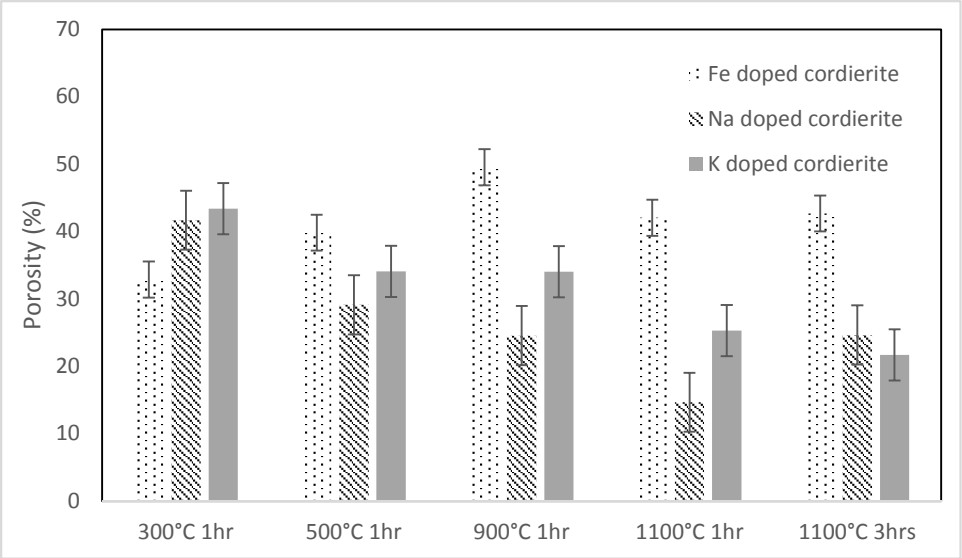

Figure 3.17 porosity of Iron, sodium and potassium doped cordierite substrate treated with increasing temperature (300ºC, 500ºC, 900ºC and 1100ºC)

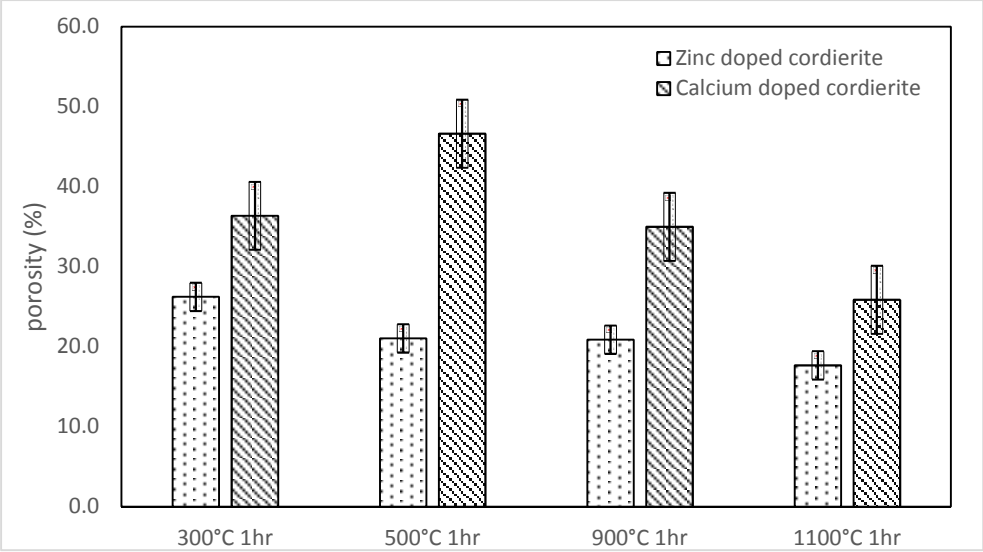

Figure 3.18. Porosity of cordierite substrate doped with Zn and Ca under elevated temperature (300ºC, 500ºC, 900ºC and 1100ºC for 1 hour).

www.manaraa.com

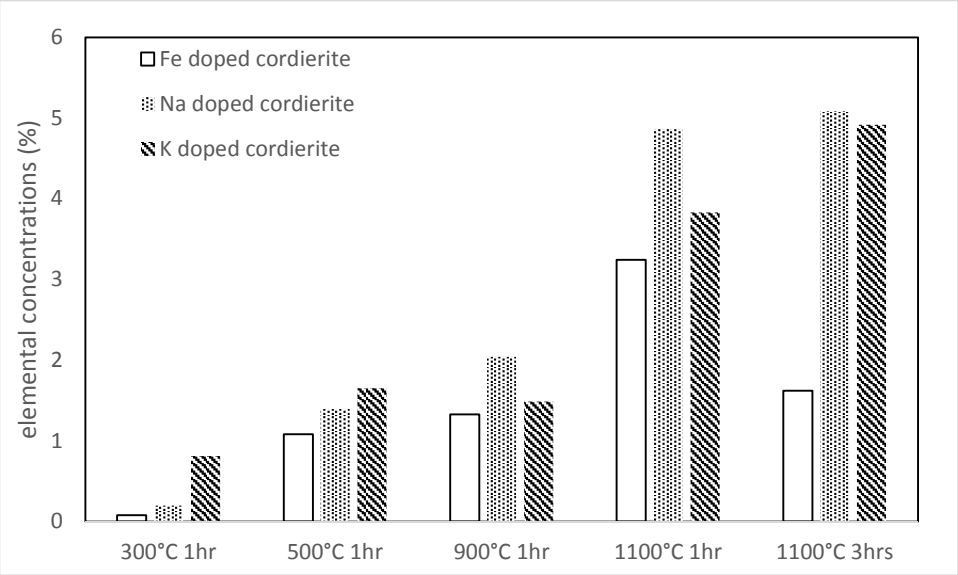

Figure 3.19 average Iron, sodium and potassium concentration on the cross-section of cordierite substrate with increasing temperature (300ºC, 500ºC, 900ºC and 1100ºC) based on EPMA

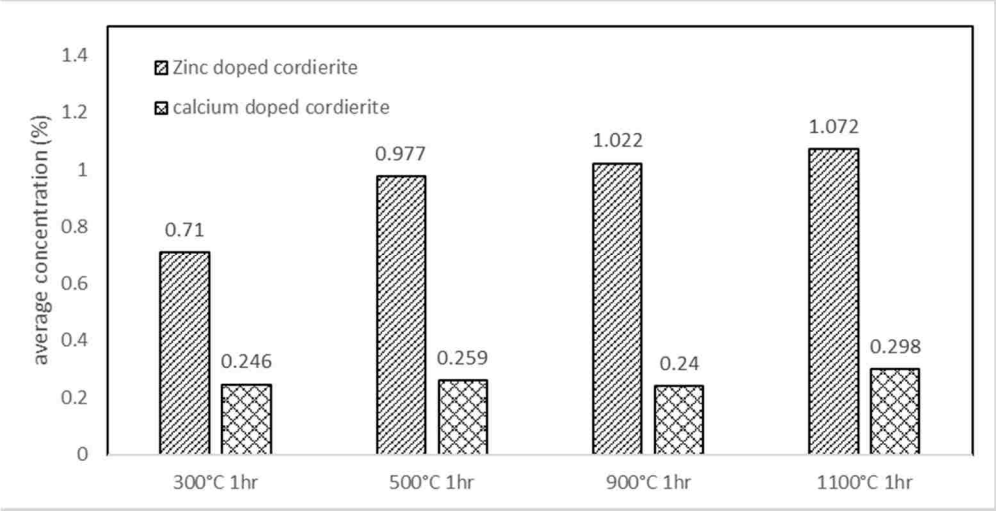

Figure 3.20. Average concentration of Zn and Ca on cordierite substrate after exposure to elevated temperature (300ºC, 500ºC, 900ºC and 1100ºC for 1 hour), samples were doped with Zn and Ca.

www.manaraa.com

3.3.3 XRD analysis of cordierite substrate under different thermal chemical conditions

3.3.3.1. Iron Exposed cordierite substrate

XRD was utilized to characterize the crystalline phase changes of the cordierite substrate samples before and after thermal-chemical treatment with iron, sodium and potassium dopants. Figure 3.21s shows XRD images for pristine cordierite substrate samples thermally treated for 1 hour with increasing temperature. Cordierite substrates doped with iron, sodium, potassium, Zinc and Calcium were heat treated for 1 hour at elevated temperatures, and results are shown in Figure 3.22s, 3.24s, 3.26s, 3.28s and 3.30s. exposure time affection results are shown in Figure 3.23s, 3.25s, 3.27s, 3.29s and 3.31s (supplementary information). The tabulated crystalline phase changes are indicated in Table 3.3, 3.4 and 3.5.

Figure 3.21s shows the major crystalline phase of pristine cordierite substrate has not been altered even when exposed to 1100^{o}C. The X-ray peak intensity remains the same which indicates the cordierite substrate maintains original crystallinity without undergoing vitrification. However, the minor crystalline phase of α-Al_2O_3 were detected with exposed to temperatures higher than 500^{o}C, which means the cordierite substrate started to decompose and alter its original crystalline phase above 500^{o}C. Figure 3.22s and

www.manaraa.com

Table 3.3 show the XRD results for the iron doped cordierite samples. These results show the crystalline phases of cordierite is altered after heat treatment of 300ºC, as the Fe substituted for Mg to form iron-spinel ($Fe_2Al_4Si_5O_{18}$). Additionally, there were minor crystalline phases of spinel ($MgAl_2O_4$) with thermal expansion coefficient 0.18^oC^{-1} at 100ºC or $3.24\ ^oC^{-1}$ at 1200ºC, α-Al_2O_3 and trace crystalline phases of $Al_{4.5}FeSi$. The minor phase formed the trace phase, by Si diffusion away from the cordierite substrate and reacted with Fe to form $Al_{4.5}FeSi$. The peak intensity of the crystalline phases of spinel ($MgAl_2O_4$) decreases with increasing temperature. Since $Al_{4.5}FeSi$ is detected as a trace crystalline phase at 1100ºC, continued thermal treatment with higher temperatures could result in more of this crystalline phase. The peak intensity for $Fe_2Al_4Si_5O_{18}$ remained the same from 300ºC to 900ºC, and only decreased slightly after thermal treatment of 1100ºC. This indicates that Fe substitution begins at 300ºC and becomes more amorphous with increasing temperature.

Figure 3.23s and Table 3.4 show XRD results for iron doped cordierite substrate unheated, and heat treated at 900ºC with increasing time. These results show that the major crystalline phases are iron-spinel ($Fe_2Al_4Si_5O_{18}$), followed by minor crystalline phases of spinel ($MgAl_2O_4$), α-Al_2O_3 and trace amount of $Al_{4.5}FeSi$. The peak intensity of these crystalline phases are extremely low for the iron doped unheated sample. When not

www.manaraa.com

heated, the Fe exists as an amorphous structure or has been rinsed out by the dehydrated ethanol. The peak intensity of $Fe_2Al_4Si_5O_{18}$ increases with exposure time, demonstrating that the $Fe_2Al_4Si_5O_{18}$ crystalline growth increases with time. $Al_{4.5}FeSi$ peak intensity first increases with exposure time then decreases, which indicates that the $Al_{4.5}FeSi$ crystalline phase tends to be amorphous and form a glaze-like structure.

3.3.3.2 Sodium Exposed cordierite substrate

Figure 3.24s and Table 3.3 shows the XRD results of the sodium doped substrate exposed to increasing heat treatment temperatures. When the cordierite substrate was exposed to sodium, the major cordierite crystalline phase was not changed after exposure to temperatures of 300ºC and 500ºC. This can be ascertained by the fact that other crystalline phases are still in trace amounts. When exposed the sodium doped substrate sample was exposed to 900ºC, the cordierite crystalline phase shifted from $Mg_2Al_4Si_5O_{18}$ to Na-spinel ($NaAl_5O_8$). This suggests the corrosion process first generates carnegieite then transfers to nepheline which is detected as Mg-Al spinel (Montanaro L. 1994). In these corrosion processes, sodium substitutes with Mg and Si in the cordierite and generates the new crystalline phases. When exposed to 1100ºC, there is substantial alteration of the substrate crystalline phases. Specifically, the cordierite reacted with sodium through Mg and Si substitution forming variations of sodium silicate at 1100ºC. These silicate phases were

www.manaraa.com

also confirmed by Dario (1998) as $Na_2Si_2O_5$ or Na_2SiO_3 at near 800°C (Dario M.T. 1998). The peak intensities decreased with increasing temperature. Specifically, the cordierite peaks decreased sharply after 900°C, which indicates the cordierite substrate became more amorphous. The sodium nepheline attacks the cordierite by dissolving it, enriching the melt in Mg and Al (Maier N. 2010).

With regard to the exposure time at 900°C, Figure 3.23s and Table 3.4 shows the substrate crystalline phase was not changed after 30 minutes. When exposed to 900°C for 1 hour and 3 hours, sodium nepheline ($NaAlO_2$) was formed. Therefore, if the uncontrolled regeneration in a diesel particulate filters occurs for a collective time of 1 hour at 900°C, the substrate could experience Na corrosion. In the case of coolant leaks, the sodium concentration can be extremely high, and the increased concentration at high temperatures could facilitate the corrosion (Jesus Y.M.L.D. 2012).

3.3.3.3 Potassium Exposed cordierite substrate

The crystalline phase changes of the potassium doped cordierite substrate after heat treatment illustrated are presented in Figures 3.26s and 3.27s. Figure 3.26s and Table 3.3 show the crystalline phase of kaliophilite ($KAlSiO_4$) first appears after 1 hour of heat treatment at 900°C, but diminishes after 1 hour of exposure at 1100°C. This result indicates

www.manaraa.com

the crystalline phase becomes amorphous at 1100ºC. This was confirmed by Takahashi, who pointed out the similar transition (Takahashi J. 1998). After 1 hour of heat treatment at 300ºC and 500ºC, the $Mg_2Al_4Si_5O_{18}$ is unchanged. One study reports that kaliophilite was not detected below temperature of 1000ºC (Takahashi J. 1998). However, in the current study, we demonstrated the kaliophilite can be formed after exposure to 900ºC. Similar to sodium, the potassium corrosion pathway is through substitution with Mg in the substrate. Figure 3.27s and Table 3.4 show the potassium treated, yet unheated, cordierite substrate sample detected K_3PO_4, which is residual K_3PO_4 from treatment. When the cordierite substrate was exposed to 900ºC for 30 minutes, the crystalline phase of $KAlSiO_4$ appeared. However, after 1 hour of heat treatment at 300ºC and 500ºC, the substrate remained stable under potassium exposure. The XRD patterns in Figure 3.26s, suggest that 900ºC is necessary for K to form $KAlSiO_4$. Further, Figure 3.27s shows the $Mg_2Al_4Si_5O_{18}$ peak intensity decreased with respect to exposure time, which indicates cordierite becomes more amorphous with increasing thermal exposure.

3.3.3.1 Zinc Exposed Cordierite Substrate

The zinc doped cordierite was observed to experience both crystalline phase changes and crystallinity changes, during thermal treatment as appraised by X-ray diffraction (Figures

www.manaraa.com

3.28s and 3.29s in supplemental information). The tabulated XRD crystalline phases are indicated in Table 3.3 and 3.5. The major crystalline phase of cordierite ($Mg_2Al_4Si_5O_{18}$) did not change even when exposed to 1100°C in the presence of zinc (Figure 3.28s and table 3.3). However, the cordierite peak intensity decreased with increased temperatures as depicted in Figure 3.28s, which means the crystallinity of cordierite decreases as the temperature increases, confirming the melting of the cordierite. The zinc was detected as ZnO, which was the major crystalline phase of zinc, as appraised by XRD. The ZnO peaks increase significantly with increasing the temperature, which means the zinc phosphate decomposed to ZnO. The minor crystalline phase of spinel ($MgAl_2O_4$) was detected at temperatures of 300°C, 500°C and 900°C. The trace crystalline phase of Zn_2SiO_4 was only detected at temperatures of 1100°C. This crystalline phase (Zn_2SiO_4) was created via the double substitution of both Mg and Al with Zn. This phase change was confirmed by Eaton (2006) which occurred only after zinc poisoning (Eaton S.J. 2006). Pomeroy (2012) reported that liquid phosphate dissolves cordierite, leading to the formation of zinc aluminum spinel at 900°C (Pomeroy M.J. 2012).

When considering the increased thermal treatment time, there is not a significant difference in the crystalline phases, but a slight change in the peak intensity (table 3.5). Specifically, for ZnO, the peak intensity increases from 300°C to 900°C, but

www.manaraa.com

decreases from 900ºC to 1100ºC. The increasing presence is due to zinc phosphate converting to zinc oxide. Yet further increasing the temperature to 1100ºC and time 3 hours, the ZnO begins to comingle with the cordierite. Overall, the Zn-cordierite reaction is more dependent on temperature than time as the sample treated at 300ºC for 10hrs did not exhibit changes to crystalline phases or peak intensity.

3.3.3.2 Calcium Exposed Cordierite Substrate

The crystallinity and crystalline phases of cordierite substrate exposed to calcium during thermal treatment are shown in Figure 3.30s and 3.31s. The major crystalline phase of cordierite was unchanged from 300ºC to 1100ºC. However, when exposed to Ca at 1100ºC, the cordierite tested positive for the trace crystalline phases of $CaMg_2$, Ca_2SiO_4. This finding is confirmed with what Montanaro (1994) observed with the formation of melilite at 1100ºC for 1 hour (Montanaro L. 1994). This reaction occurs when the Mg and Al in cordierite are substituted with Ca and the Mg diffused away to react with Ca to produce $CaMg_2$, which is shown in Figures 3.30s and 3.31s. The cordierite crystallinity remained stable at 91.71% to 91.74% for exposure at 300ºC and 1100ºC, which indicates that the Ca-cordierite interaction is stable at temperatures experienced by DPFs (table 3.3). With regard to the time of thermal treatment, even with prolonged reaction times up to 10 hours,

www.manaraa.com

the crystalline phase remains stable, as does the peak intensity. Therefore, the Ca-cordierite interaction is stable at the temperatures that the cordierite substrate would experience in DPF applications. These findings are confirmed by Pomeroy (2012) which observed no obvious crystalline phases change for Ca-cordierite even when exposed to 1250ºC for 30 minutes (Pomeroy M.J. 2012).

www.manaraa.com

Table 3.3 XRD results: Principal phases formed by reaction between Fe, Na, K and cordierite as function of temperature

	Temperature (°C)			
	300	500	900	1100
Pristine cordierite	$Mg_2Al_4Si_5O_{18}$(h)	$Mg_2Al_4Si_5O_{18}$(h) Al_2O_3(m)	$Mg_2Al_4Si_5O_{18}$(h) Al_2O_3(m)	$Mg_2Al_4Si_5O_{18}$(h) Al_2O_3(m)
Fe Doped	$Mg_2Al_4Si_5O_{18}$(h) $Fe_2Al_4Si_5O_{18}$(h)	$Mg_2Al_4Si_5O_{18}$(h) $Fe_2Al_4Si_5O_{18}$(h) Al_2O_3(m)	$Mg_2Al_4Si_5O_{18}$(h) $Fe_2Al_4Si_5O_{18}$(h) Al_2O_3(m) $MgAl_2O_4$(m)	$Mg_2Al_4Si_5O_{18}$(h) $Fe_2Al_4Si_5O_{18}$(h) Al_2O_3(m) $MgAl_2O_4$(m) $Al_{4.5}FeSi$(l)
Na Doped	$Mg_2Al_4Si_5O_{18}$(h)	$Mg_2Al_4Si_5O_{18}$(h)	$Mg_2Al_4Si_5O_{18}$(h) $NaAl_5O_8$(m)	$Mg_2Al_4Si_5O_{18}$(h) $Na_2Si_2O_5$(m) $Na_2Si_3O_7$(m) $NaAlO_2$(m)
K Doped	$Mg_2Al_4Si_5O_{18}$(h) $MgAl_2O_4$(m)	$Mg_2Al_4Si_5O_{18}$(h) $MgAl_2O_4$(m)	$Mg_2Al_4Si_5O_{18}$(h) $MgAl_2O_4$(m) $KAlSiO_4$(l)	$Mg_2Al_4Si_5O_{18}$(h) $MgAl_2O_4$(m)
Zn-Doped	$Mg_2Al_4Si_5O_{18}$(h) ZnO(h) $MgAl_2O_4$(m)	$Mg_2Al_4Si_5O_{18}$(h) ZnO(h) $MgAl_2O_4$(m)	$Mg_2Al_4Si_5O_{18}$(h) ZnO(h) $MgAl_2O_4$(m)	$Mg_2Al_4Si_5O_{18}$(h) ZnO(h) $MgAl_2O_4$(m) Zn_2SiO_4(l)
Ca-Doped	$Mg_2Al_4Si_5O_{18}$(h) $MgAl_2O_4$(m)	$Mg_2Al_4Si_5O_{18}$(h) $MgAl_2O_4$(m)	$Mg_2Al_4Si_5O_{18}$(h)	$Mg_2Al_4Si_5O_{18}$(h) $CaMg_2$(l) Ca_2SiO_4(l)

(h)=high; (m)=minor; (l)=low

www.manaraa.com

Table 3.4 XRD results: Principal phases formed by reaction between Fe, Na, K and cordierite as function of time

	900°C Thermal treatment time (hour)			
	0	0.5	1	3
Fe Doped	$Mg_2Al_4Si_5O_{18}$(h)	$Mg_2Al_4Si_5O_{18}$(h) $Fe_2Al_4Si_5O_{18}$(m) $MgAl_2O_4$(m) Al_2O_3(m) $Al_{4.5}FeSi$(l)	$Mg_2Al_4Si_5O_{18}$(h) $Fe_2Al_4Si_5O_{18}$(m) $MgAl_2O_4$(m) Al_2O_3(m)	$Mg_2Al_4Si_5O_{18}$(h) $Fe_2Al_4Si_5O_{18}$(m) $MgAl_2O_4$(m) Al_2O_3(m) $Al_{4.5}FeSi$(l)
Na Doped	$Mg_2Al_4Si_5O_{18}$(h)	$Mg_2Al_4Si_5O_{18}$(h)	$Mg_2Al_4Si_5O_{18}$(h) $NaAl_5O_8$(m)	$Mg_2Al_4Si_5O_{18}$(h) $NaAl_5O_8$(m) $NaAlSiO_4$(m)
K Doped	$Mg_2Al_4Si_5O_{18}$(h) K_3PO_4(m)	$Mg_2Al_4Si_5O_{18}$(h) $MgAl_2O_4$(l) $KAlSiO_4$(l) K_3PO_4(m)	$Mg_2Al_4Si_5O_{18}$(h) $MgAl_2O_4$(m) $KAlSiO_4$(l)	$Mg_2Al_4Si_5O_{18}$(h) $MgAl_2O_4$(m) $KAlSiO_4$(l) K_3PO_4(l)

(h)=high; (m)=minor; (l)=low

Table 3.5 XRD results: crystalline phases formed between Zn, Ca, and cordierite at elevated temperatures with respect to treatment time

	300°C	500°C	900°C	1100°C
	10hr	3hr	3hr	3hr
Zn-Doped	$Mg_2Al_4Si_5O_{18}$(h) ZnO(h) $MgAl_2O_4$(m)	$Mg_2Al_4Si_5O_{18}$(h) ZnO(h) $MgAl_2O_4$(m)	$Mg_2Al_4Si_5O_{18}$(h) ZnO(h) $MgAl_2O_4$(m)	$Mg_2Al_4Si_5O_{18}$(h) ZnO(h) $MgAl_2O_4$(m) Zn_2SiO_4
Ca-Doped	$Mg_2Al_4Si_5O_{18}$(h) $MgAl_2O_4$(m)	$Mg_2Al_4Si_5O_{18}$(h) $MgAl_2O_4$(m)	$Mg_2Al_4Si_5O_{18}$(h)	$Mg_2Al_4Si_5O_{18}$(h) $CaMg_2$(l) Ca_2SiO_4(l)

h high, m minor, l low

www.manaraa.com

3.4. Conclusions

Herein, laboratory controlled studies treated cordierite substrate samples with metal ash components, consisting of sodium, potassium, and iron. The temperatures selected (300°C – 1100°C) were identified to represent various DPF thermal regimes experienced during diesel engine operation and DPF regeneration. Results indicate that Fe, Na, K, Ca and Zn each have the capability to impact the physical chemical properties of the cordierite substrate. Among these three ash components Na_2CO_3 and K_3PO_4 reacted more aggressively than $FeSO_4$ and ZnO with the cordierite substrate. Calcium has the least affection on the cordierite under normal DPF running and regeneration condition although it has highest concentration in the DPF ash.

The SEM micrographs of iron doped cordierite show cracking after 1 hour of heat treatment at 900°C and 1100°C. While sodium doped cordierite appears to develop cracking after 500°C and potassium doped cordierite first initiated melting at 300°C. zinc phosphate reacted with cordierite, and melted areas covered the substrate surface, after exposure to 900°C and 1100°C for 1 hour. When prolonged thermal treatment was appraised, glaze-like surfaces and large areas of cracking were observed after treatment at 900°C and 1100°C for 3 hours. The interaction of calcium-cordierite is perhaps best

www.manaraa.com

described as stable, as no observable changes to the cordierite structure were made with SEM, even after treatment at 1100ºC. Both the cracking and fusing of cordierite substrate became severe with increase thermal treatment temperatures and time for iron, sodium and potassium doped cordierite.

The WDS results show migration and dispersion effects of $FeSO_4$ on cordierite were only identified after exposure at 900ºC. XRD results of the iron doped cordierite show that after heat treatment for one hour at both 900ºC and 1100ºC, the $FeSO_4$ reacted with cordierite through Mg substitution with Fe as detected by XRD.

The WDS results for the Na, K and Zn doped cordierite substrate both show the migration and dispersion of Na and K after treating the substrates for 1 hour at 500ºC. The concentration of Na, K and Zn that migrate into the substrate increases with heat treatment temperature. As observed by WDS, the corrosive pathway of Na, K and Zn begins by attaching to the cordierite surface. The average zinc concentration increased from 0.71%, 0.977%, 1.022%, and 1.072% for 300ºC, 500ºC, 900ºC and 1100ºC respectively, which indicates that the zinc is melting into the cordierite, and this process is both time and temperature dependent. Additionally, the cross-sectional porosity of Zn-cordierite decreased with increasing temperature, due to the melting phenomena and comingling. Calcium-cordierite interaction is stable, even at temperatures as high as

www.manaraa.com

1100ºC. As evidence of this, the average cross-section concentration remained stable at: 0.246%, 0.26%, 0.24% and 0.298% for temperature ranging from 300ºC to 1100ºC.

XRD results show the Na_2CO_3 and K_3PO_4 possess similar corrosive mechanism as they substitute for the Mg or Al in cordierite to form sodium alumisilicate, spinel, nepheline, kaliophilite or potassium alumisilicate. The corrosive effects of Na and K begin at temperatures after the doped cordierite substrates were heat treated at 300ºC. Herein, the melting process of Na was detected after 900ºC exposure. The K induced melting appeared after exposure to only 500ºC, which was the lowest melt temperature of the ash components tested. In both sodium and potassium induced cases of melting, the melted area appears to have clear grain boundaries surrounded by intact cordierite. SEM results suggest that Na_2CO_3 produced the most cracks, when compared to cordierite substrates doped with $FeSO_4$ and K_3PO_4 exposure. Zinc reacted with cordierite by alter its crystalline phases and generate new crystalline phases including $MgAl_2O_4$ for 300ºC and Zn_2SiO_4 for 1100ºC. The crystallinity of zinc treated cordierite substrate decreased with increased temperature, indicating melting of the crystalline structure, yielding a more glass-like amorphous structure. The interaction of Calcium-corderite only yielding the trace crystalline phases of $CaMg_2$ and Ca_2SiO_4, formed at 1100ºC. Herein, under laboratory simulated conditions, the cordierite substrate crystallinity, ash component distribution

www.manaraa.com

throughout the cordierite, and substrate porosity were strongly influenced by the thermal-chemical conditions.

Acknowledgements

The authors would like to thank for the financial supported by both Lehigh University and Hunsicker Emissions Services LLC through Research for Advanced Manufacturing in Pennsylvania Program (RAMP) Project and Pennsylvania Infrastructure Technology Alliance (PITA).

3.5References

Bachiorrini A. (1996) "New hypothesis on the mechanism of the deterioration of cordierite diesel filters in the presence of metal oxides." Ceramic International. 22(1): 73-77.

Bunting B.G., et al. (2005) "Phosphorous poisoning and phosphorous exhaust chemistry with diesel oxidation catalysts." SAE International. No.: 2005-01-1758.

Bianco R., Jacobson N. (1989) "Corrosion of cordierite ceramics by sodium sulphate at 1000ºC." Journal of Material Science, 24:2903-2910.

Chen K., Martirosyan S., Luss D. (2010) "temperature excursions during soot combustion in a diesel particulate filter (DPF)." Ind. Eng. Chem. Res. 49:10358-10363.

www.manaraa.com

Dario M.T., Bachiorrini A. (1998) "Interaction of some pollutant oxides on durability of silicon carbide as a material for diesel vehicle filters." Journal of materials science. 33:139-145.

Donaldson. "Engine horsepower and exhaust flow guide." Donaldson, 2-8.

Eaton S.J. (2006). "Accelerated poisoning of diesel oxidation catalysts by zinc dialkyldithiophosphate derived phosphorus." Master's thesis. University of Tennessee.

Givens W.A., et al. (2003) "Lube formulation effects on transfer of elements to exhaust after treatment system components." SAE International. No.2003-01-3109.

Ibrahim N., et al. (2011). "Effect of CaO from different sources on the nanostructured cordierite." Advanced Materials Research, 364: 368-371.

Jesus Y.M.L.D., et al. (2012) "effect of coolant exposure on diesel exhaust after treatment performance." SAE International. No.:2012-01-1091.

Johnson R., et al. (2003). "Solid state reactions of cordierite precursor oxides and effect of CaO doping on the thermal expansion behavior of cordierite honeycomb structures." Journal of materials science. 38: 2953-2961.

Kimura K., et al. (2006) "Real world study of diesel particulate filter ash accumulation in heavy duty diesel trucks." SAE International. No.:2006-01-3257.

Law M.C., Clarke A., Garner C.P. (2004) "The effect of soot properties on the regeneration behavior of wall-flow diesel particulate filters." Proc. Inst. Mech. Eng. Part D J. Automob. Eng. 218(D12):1513-1524.

www.manaraa.com

Lachmann I.M., Bagley R.D., Lewis R.M. (1981) "Thermal expansion of extruded cordierite ceramics." JACS Bulletin, 60(2):202-205.

Maier N., et al. (2010) "Mechanisms and orientation dependence of the corrosion of single crystal cordierite by model diesel particulate ashes." Journal of European ceramic society. 30(7):1629-1640.

Montanaro L. and Bachiorrini A. (1994) "Influence of some pollutants on the durability of cordierite filters for diesel cars." Ceramic International. 20(3):169-174.

Merkel G.A., Cutler W.A., Warren C.J. (2001) "Thermal Durability of wall flow ceramic diesel particulate filters." SAE International. No.: 2001-01-0190

Negro A., et al. (1993) "Interaction between some oxides and cordierite." Journal of European Ceramic Society, 12:493-498.

Ogunwumi R.S., et al. (2007) "Performance evaluations of aluminum titanate diesel particulate filters." SAE International. No.: 2007-01-0656.

Pomeroy M.J., et al. (2012) "Degradation resistance of cordierite diesel particulate filters to diesel fuel ash deposits." Journal of American Ceramic Society, 95(2):746-753.

Perry D.L. (1995) "handbook of inorganic compounds." CRC press, Inc., New York, 1995, Pp. 206-207.

www.manaraa.com

Perry D.L. (1995) “handbook of inorganic compounds.” CRC press, Inc., New York, 1995, pp. 234-235.

Rohan P., et al. (2004) “Thermal and mechanical properties of cordierite, mullite and steatite produced by plasma spraying.” Ceramics International. 30:597-603.

Scardi P., Sarton N. (1994) “thermal stability of cordierite catalyst supports contaminated by Fe_2O_3, ZnO and V_2O_5.” Journal of European Ceramic Society. 13:273-282.

Sappok A., Wong V.W. (2011) “Lubricant derived ash properties and their effect on diesel particulate filter pressure drop performance.” Journal of Engineering for Gas turbo and power 133(3), No.:032805.

Takahashi J., Kawai Y., Shimada S. (1998) “Hot corrosion of cordierite ceramics by Na and K salts.” Journal of the European Ceramic Society. 18:1121-1129.

Williams A., et al. (2011) “Impact of biodiesel impurities on the performance and durability of DOC, DPF and SCR technologies.” SAE International. No. 2011-01-1136.

Yang K., Fox J.T., Hunsicker R. (2016) “characterizing diesel particulate filter failure during commercial fleet use due to pinholes, melting, cracking and fouling.” Emission Control Science and Technology. 2(3):145-155.

Supplemental information:

www.manaraa.com

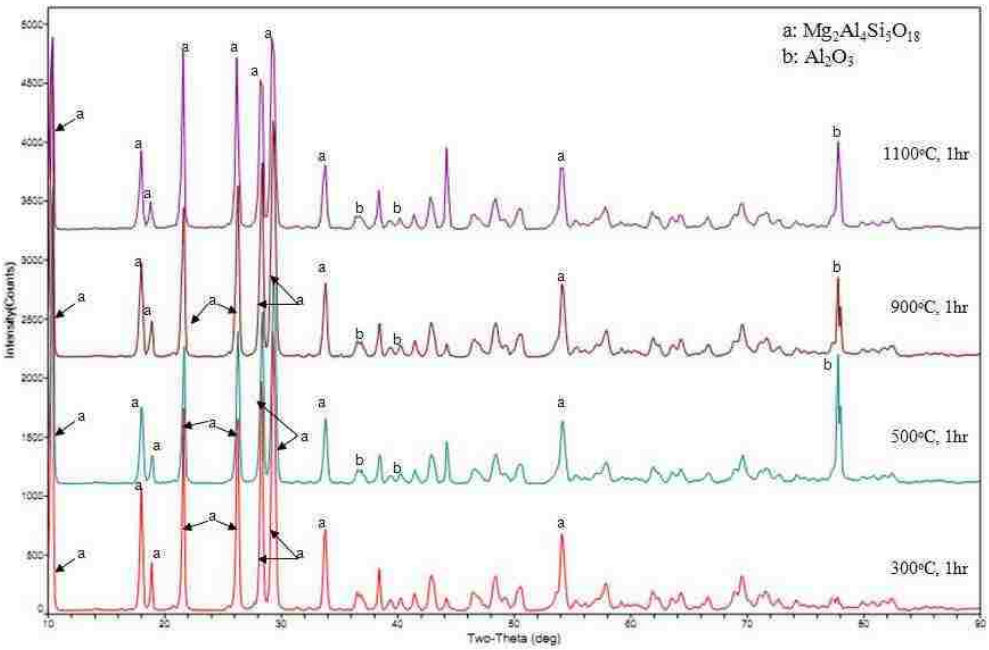

Figure 3.21s. X-Ray Diffraction pattern of pristine cordierite substrate heated for 1 hour with increasing temperature (300ºC, 500ºC, 900ºC and 1100ºC)

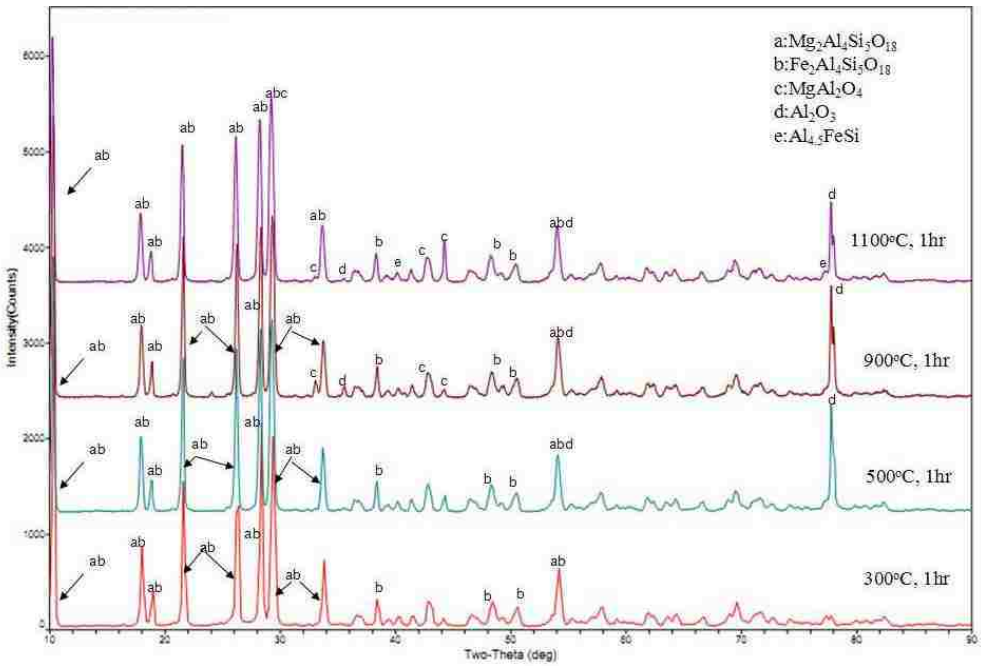

Figure 3.22s. X-Ray Diffraction pattern of Fe doped cordierite substrate heated for 1 hour with increasing temperature (300ºC, 500ºC, 900ºC and 1100ºC)

www.manaraa.com

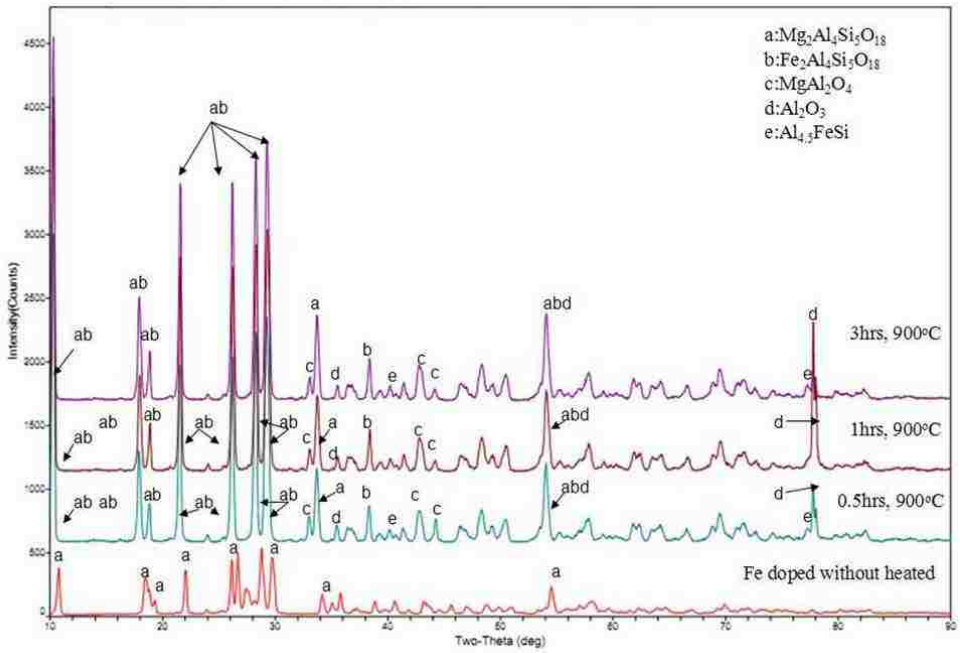

Figure 3.23s. X-Ray Diffraction pattern of Fe doped cordierite substrate, heated at 900°C with increasing aging time 0, 30 minutes, 1 hour, and 3 hours.

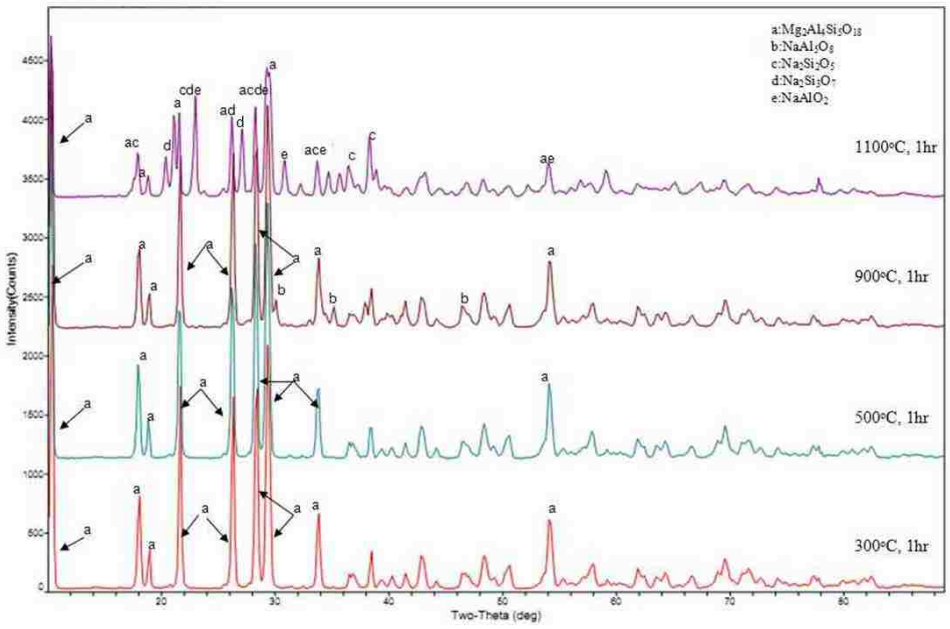

Figure 3.24s. X-Ray Diffraction pattern of Na doped cordierite substrate for 1 hour with increasing temperature (300°C, 500°C, 900°C and 1100°C)

www.manaraa.com

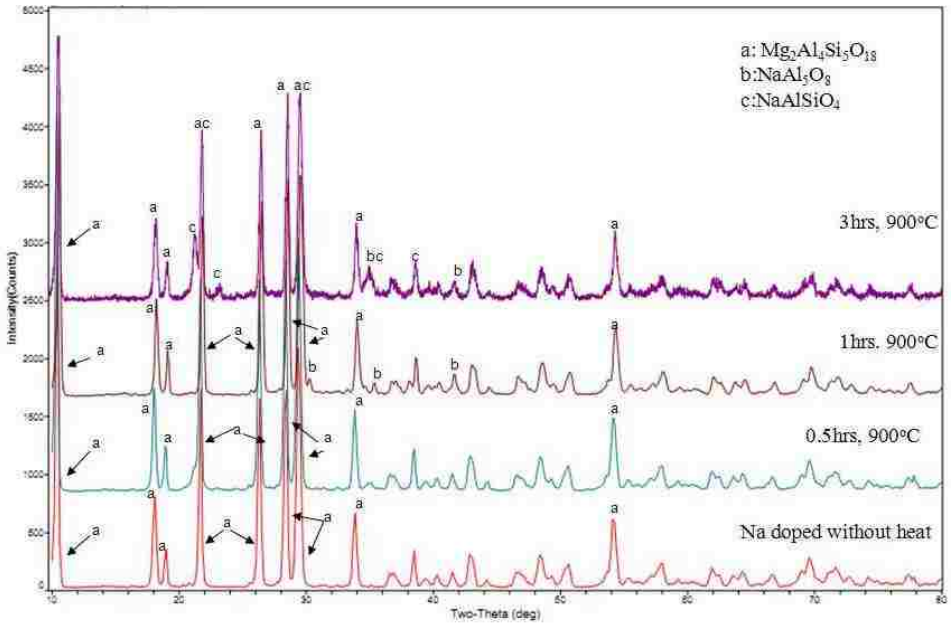

Figure 3.25s. X-Ray Diffraction pattern of Na doped cordierite substrate heated at 900ºC at increasing aging times (0, 30min, 1hr, 3hrs)

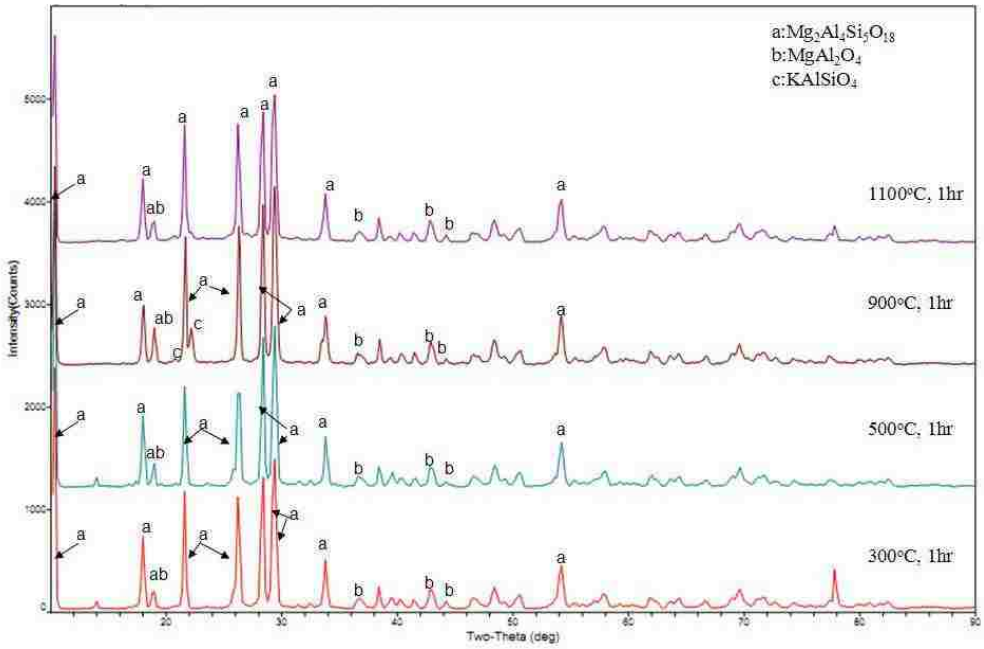

Figure 3.26s. X-Ray Diffraction pattern of K doped cordierite substrate heated for 1 hour with increasing temperatures (300ºC, 500ºC, 900ºC and 1100ºC).

www.manaraa.com

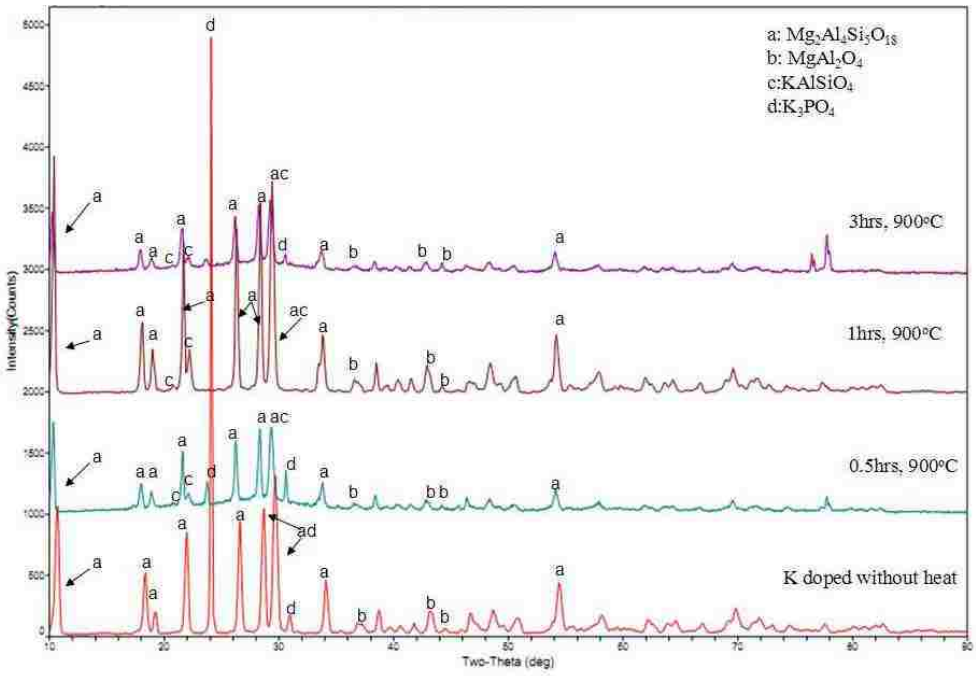

Figure 3.27s. X-Ray Diffraction pattern of K doped cordierite substrate heated at 900°C for increasing aging times.

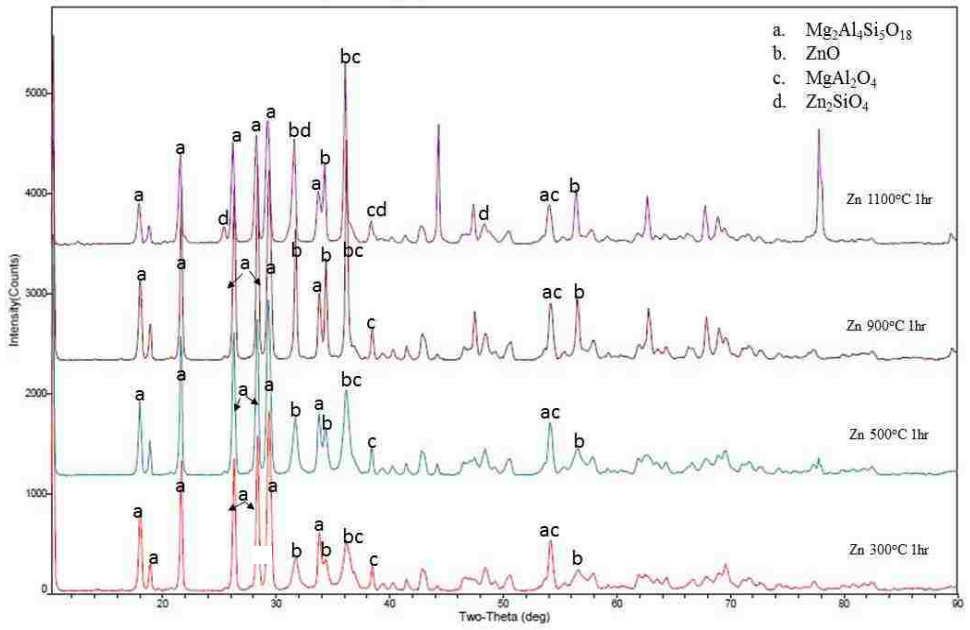

Figure 3.28s. X-ray Diffraction pattern of zinc doped cordierite substrate under different temperature (300°C, 500°C, 900°C and 1100°C).

www.manaraa.com

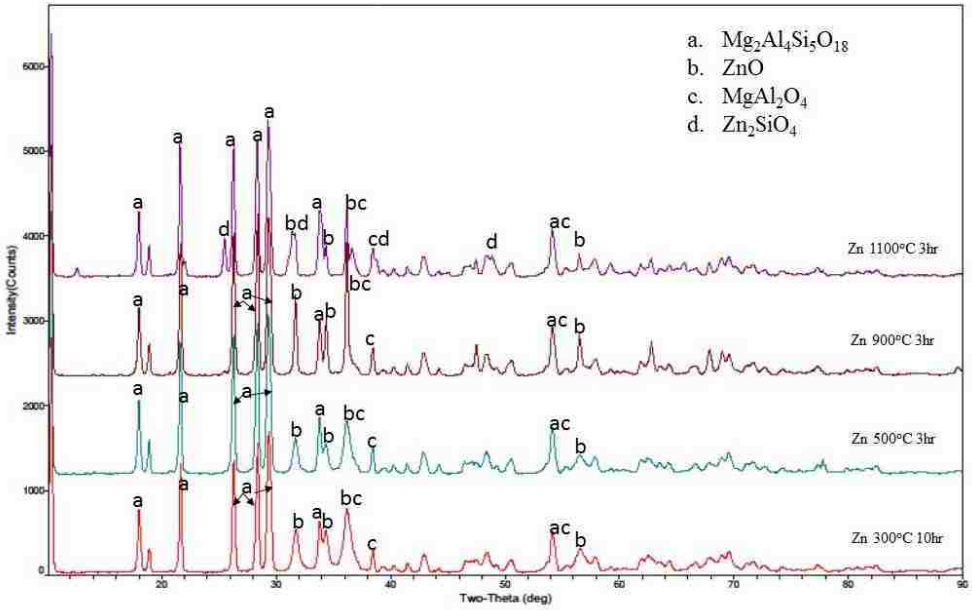

Figure 3.29s. X-ray diffraction pattern of Zn doped cordierite substrate under elevated time.

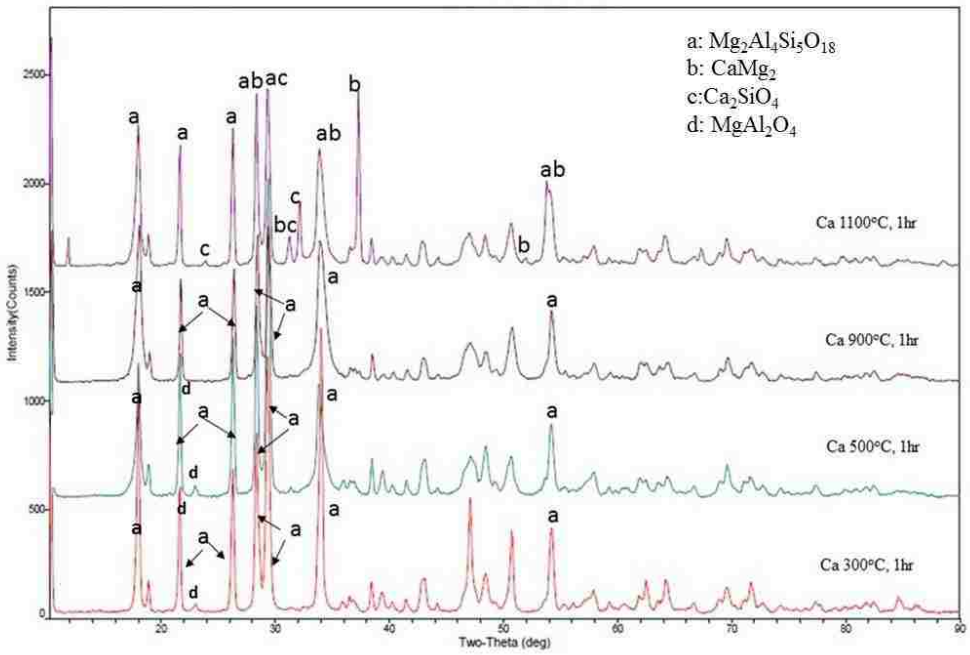

Figure 3.30s. X-ray diffraction pattern of Ca doped cordierite substrate under different temperatures (300ºC, 500ºC, 900ºC and 1100ºC).

www.manaraa.com

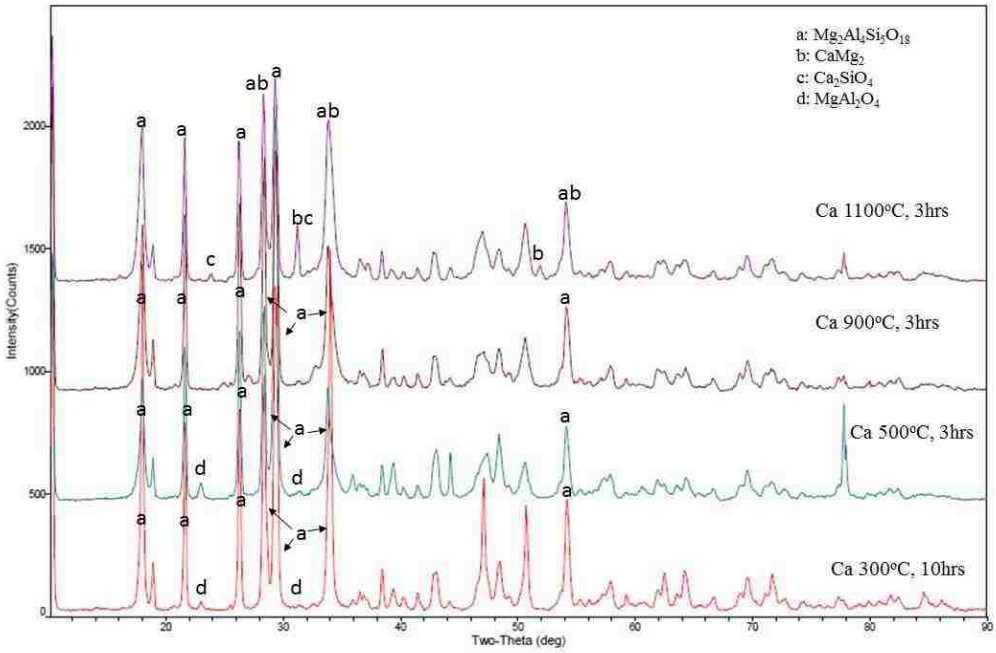

Figure 3.31s. X-ray diffraction pattern of Ca doped cordierite substrate held under elevated temperatures for 3 hours.

www.manaraa.com

Chapter 4

Water based DPF regeneration process: Methods, lab optimization results and full-scale demonstration

Abstract

A water based DPF regeneration technology was developed and optimized. The lab scale tests and full-scale demonstration indicate the water-based wash can remove DPF soot and ash with a concentration much higher than the conventional treatment method. Further the wash process can improve engine back pressure by more than 50% than the conventional treatment method.

4.1 Introduction

According to the CARB, DPF must be periodically removed to clean the soot and ash from the DPF, which results in lower engine back pressure. Despite on-board vehicle passive and active regeneration, DPFs and DOCs need to be removed from the vehicle for additional cleaning, which is called reclamation. The conventional reclamation method (designed by FSX) is based on utilizing pneumatic air to flush out ash, followed by high-temperature calcination to remove the soot. However, the embedded ash cannot be removed by this method and it stays in the DPF channel walls, leading to premature failures

www.manaraa.com

as previously discuss. Therefore, advanced technologies are needed in order to improve DPF reclamation efficiency. During the past 20 years, numerous reclamation methods have been developed by Corning, LLC., Cummins,LLC., General Motor Corporation, LLC., Carlson Gaskey & Oil, LLC., etc (Bardhan P. 2008, Ehlers M.S. 2010, Gregorie D.L. 2007). Most of these methods are based on compressed air to blow out the soot and ash in order to release the engine back pressure. In addition, General Motors Corporation (2007) applied microwave generated heat in order to burn out the soot embedded in the DPF. The DPF ash still remained in the DPF after the regeneration for all those methods since pneumatic air cannot blow out the DPF ash that attached to the substrate. In addition to the pneumatic air method, wet washing processes have already been developed and applied to regenerate the DPF by Corning (2008), who make use of inorganic and organic acid at pH=1.0 to remove the embedded ash. However, this process does not remove soot. And the potential corrosive acidic can be harmful to the Pt/Pd catalysts.

Herein, we engineered a water-based wash based on the physical-chemical property of the soot and ash components. The soot is composed of single carbon molecules which agglomerate to form large-sized carbon soot. Therefore, the soot surface is hydrophobic. During the incomplete combustion of diesel fuel, the soot that forms is comprised of approximately 75% to 90% in the C_{14}-C_{27} alkane, and 3%-20% as aromatic hydrocarbons

www.manaraa.com

compose the soluble organic fraction (SOF) hydrocarbons in the soot (Vojtisek-Lom. M., 2012, Liati A. 2013, Graskow B.R. 1998). Therefore, the soot particle surfaces are partially hydrophobic and hydrophilic which need to be characterized before designing the wash formulation.

In addition to the soot, the ash components are comprised of alkalis and metals, that have been through the combustion process. In order to remove these metallic ash and alkali components, chelating agents or acids must be selected that do not damage the Pt/Pd catalyst coating.

The author collaborated with Hunsicker Emission Service during the past four years to successfully develop an improved water based cleaning process that can remove both carbon soot and metallic ash. The wash formulation effectively removed both DPF soot and ash components. In addition, the effects on the Pd/Pt was evaluated and confirmed that it is safe. More than two hundred of DPFs, DOCs and SCRs have been regenerated with this water based method and wash efficiency was compared to the pneumatic air method.

4.2 Materials and Methods

A commercial exhausted DPF has been crashed into powder, 50g of DPF powder was added to 100ml of wash solution, agitate for 10 mins followed by analyzing the wash

www.manaraa.com

solution. The selected Ca, Mg, Na, K, Zn, Fe in the wash solution will be analyzed by Atomic Absorption Spectrometer (AAS). For the Pt/Pd corrosion test, 1g of pure Pt and Pd wire was added to 100ml of specific wash solution, and then react for 24hrs. After the reaction, Pd and Pt concentrations in the solution were analyzed by ICP-OES. The soot HLB value was first determined by adding 0.1g of the DPF soot into variable self-assembled surfactant solution with different HLB value. The HLB range is from 1.0 to 15.0. DPF soot removal lab scale experiments were carried out by first cutting the exhausted DPF into cubic slice with size of 1inch in width and 4inches in length, followed by rinse the DPF slice with certain wash solution for 10 minutes for each wash. Dried the DPF slices, weight it and took photograph of the inlet channel wall. Full-scale wash process was carried out by submerge the exhausted DPF into certain amount of wash solution which gives a weight ratio of 50g DPF/100ml wash solution. Agitation the DPF in the wash solution for 10minutes for each wash. Record the exhausted DPF weight and back pressure before and after the regeneration.

4.3 Results and Discussions

Figure 4.1 shows the washing performance of different acid combination. Different acid combinations have the different target ash compositions. Compared to deionized water, MAL acid has the highest removal efficiency for the metallic ash with typical removal rate

www.manaraa.com

of 13.37g/L-substrate. Combination acid[3] can selectively remove Calcium with the highest efficiency. Acid[6] has the highest iron removal efficiency but it is highly corrosive to the Pd/Pt catalyst coating. Considering the wash concentration in figure 4.2, there is only slightly increase in the ash removal efficiency from 3g/100ml wash to 6g/100ml wash. More specifically, 5g/100ml of wash gives the similar wash performance compared to 6g/100ml wash. There is a slightly increase in ash removal efficiency with temperature increased from 23ºC to 90ºC. Therefore, increasing temperature does not make a big difference for the ash removal efficiency as indicated by Figure 4.3.

Figure 4.4 and table 4.1 show the Pd/Pt solubility in different acid wash solutions under variable temperature. Results indicated the acid[3] has excellent Pd/Pt protection ability since the Pd/Pt concentration is lowest among all the wash solution even at temperature 90-100ºC. Acid[2] has the similar protection ability at 23ºC with citric acid, but the solubility increases rapidly when the temperature reaches 90ºC.

The hydrophile lipophile balance (HLB) value of the soot particle was determined by adding 0.5 g of soot into 50ml of surfactant solution with variable HLB value from 1.0 to 15.0. The surfactant HLB value was determined by the following equations:

$$\%(\mathrm{A}) = \frac{(X - HLB_B)X100}{HLB_A - HLB_B} \quad (1)$$

www.manaraa.com

$$\%(B) = 100 - \%(A) \quad (2)$$

In the equations, A and B stand for the emulsifier A and B respectively. X stands for the target HLB value.

The detailed experimental results are indicated in figure 4.5 which demonstrates the soot particle dispersion capacity for variable HLB value surfactant (Figure 4.5). Figure 4.6 shows the lab wash results based on the self-assembled surfactant and solvent, which majority of DPF soot and ash have been removed.

Figure 4.7 and table 4.2 shows the full scale DPF wash results. Those exhausted DPF were first washed followed by calcination to remove the remained soot and ash. Results indicated the DPF weight loss from wet wash are composed more than 80% of the total weight loss from wet wash and calcination. Although the exhausted DPFs have variable soot and ash loading depend on the vehicle running conditions, the wet wash process can reach an average soot and ash removal efficiency higher than 80% for those commercial exhausted DPFs.

Figure 4.8a,b indicate the back pressure reduction by FSX cleaning and wash process. Results indicated the FSX method cannot deeply remove the particulate matters that embedded in the channel walls since the wash process can release 10 to 15 % more back

www.manaraa.com

pressure. Weight loss results indicate that FSX cleaning can only remove 8.2g/L-DPF of DPF soot and ash, while the wash process can further remove 31.6 g/L-DPF of DPF soot and ash for DPF 03-102-1. For DPF 02-787-1, the FSX method can remove 6.2g/L-DPF of soot and ash, while chemical washing process could remove 8.7 g/L-DPF of soot and ash, respectively. Therefore, the back pressure sometimes cannot reflect the DPF soot and ash amount that has been removed. And soot contribute most of the backpressure compared to DPF ash but ash is more harmful to DPF substrate. In addition, although the FSX process can reduce the back pressure as indicated in Figure 4.8, it cannot fully represent the cleaning condition of the DPF. Therefore, further technologies are needed in order to measure the cleaning condition of the DPF. From the previous chapters, the author indicated the DPF metallic ash can attach to the DPF channel walls, react with the cordierite substrate during the DPF passive and active regeneration. The traditional FSX cleaning technology cannot remove those metallic ash that react with the substrate. Therefore, the wash process can deep clean the DPF by further remove those embedded metallic ash and soot. Till now, the Hunsicker Emission Service (HES) has applied the wash process to more than 200 commercial DPF and all of them show high soot and ash removal efficiency with good consistency.

www.manaraa.com

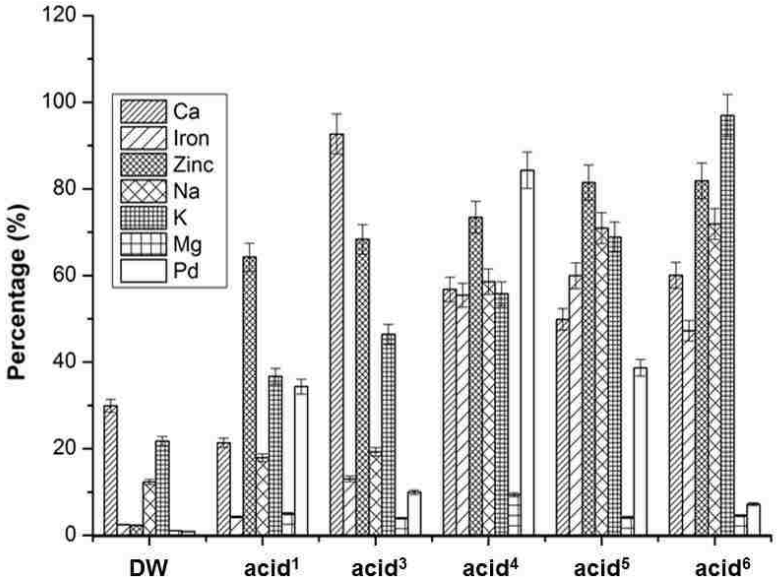

	DW (deionized water)	Acid[1]	Acid[3]	Acid[4]	Acid[5]	Acid[6]
Total Removal (mg/g)	3.1	6.3	8.3	15.6	12.8	13.4
Pd(%)	0.8	34.3	9.96	84.3	38.7	7.2

Figure 4.1 DPF metallic ash removal efficiency with different wash recipes

www.manaraa.com

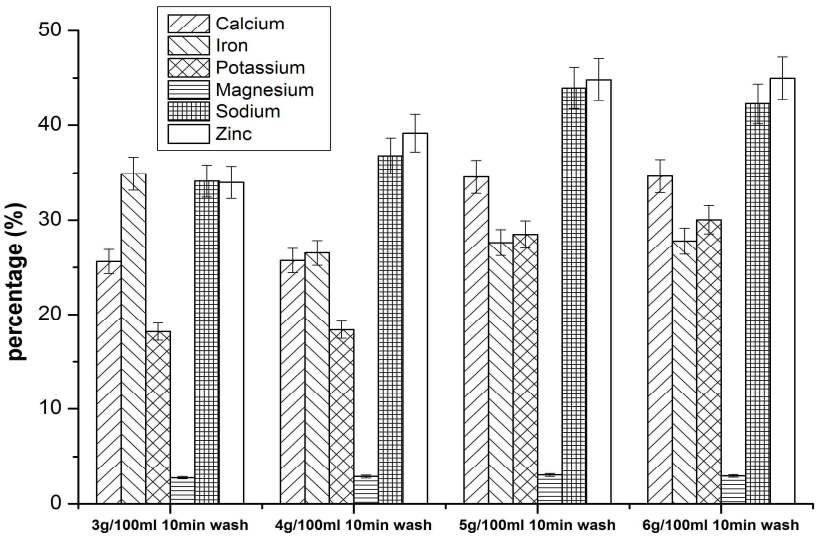

Figure 4.2 wash concentration on the removal of DPF metallic ash

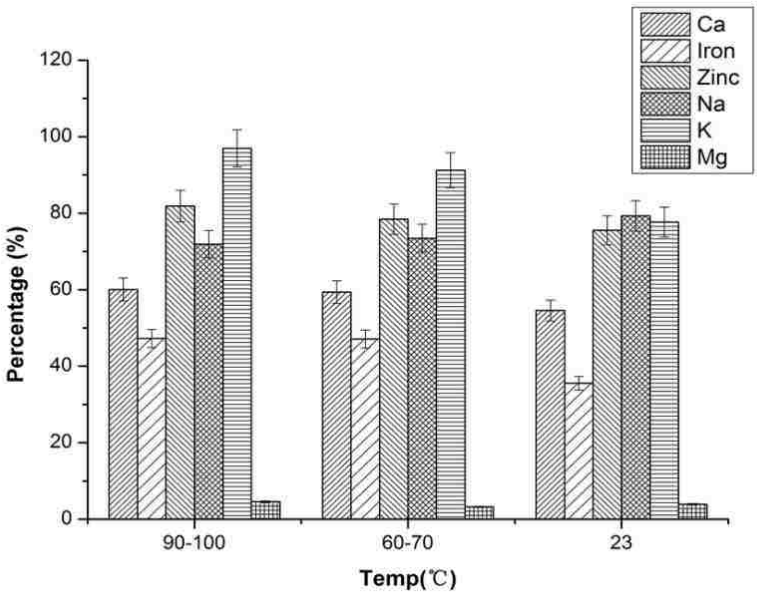

Figure 4.3 DPF metallic ash removal efficiency with different temperatures

www.manaraa.com

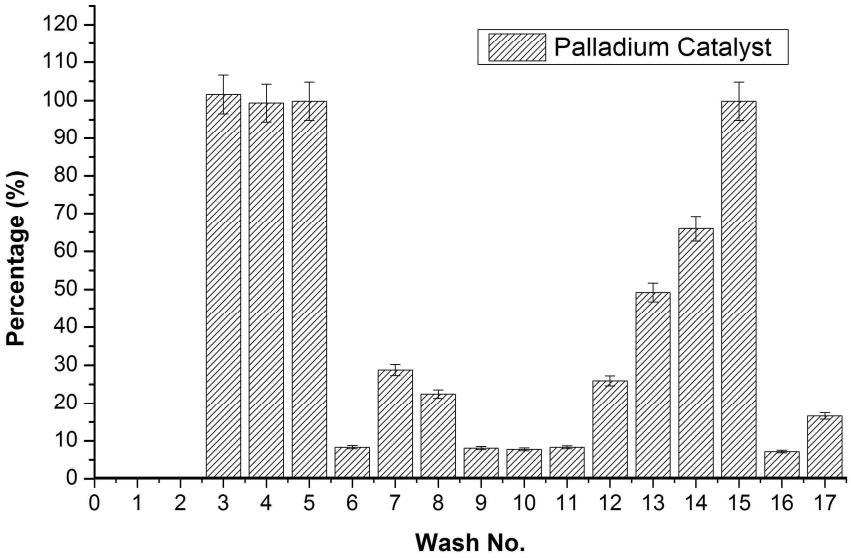

Figure 4.4 Pt/Pd solubility in different ash washing recipes

www.manaraa.com

Table 4.1 ash washing recipes and conditions

	Wash Description		Composition, Parts (mL)		Measured Properties	
Wash No.	**Additive**	**Level**	**D.I. H_2O**	**Additive**	**Temp., ^oC**	**pH**
1	None	one wash	100	0	*23°C*	3.5
2	None	one wash	100	0	*90-100*	4.215
3	acid [1]	one wash	90	10mL	*23°C*	0.445
4	acid [1]	one wash	70	30mL	*23°C*	0.01
5	acid [1]	one wash	90	10mL	*90-100°C*	0.05
6	acid [2]	one wash	90	10mL	*23°C*	1.995
7	acid [2]	one wash	90	10mL	*90-100°C*	2.87
8	acid [2]	one wash	70	30mL	*23°C*	3.5
9	acid[3]	one wash	100	6g	*23°C*	2.0-3.0
10	acid[3]	one wash	100	6g	*60 -70°C*	2.0-3.0
11	acid[3]	one wash	100	6g	*90 -100°C*	2.0-3.0
12	Acid[4]	one wash	100	5g	*23°C*	1.5-2.0
13	Acid[4]	one wash	100	5g	90-100*°C*	1.5-2.0
14	acid[5]	one wash	100	5mL	*23°C*	0.1
15	Acid[6]	one wash	100	15mL	*23°C*	0.1
16	Acid[7]	one wash	100	5g	*23°C*	1.5-2.0
17	Acid[7]	one wash	100	5g	90-100*°C*	1.5-2.0

www.manaraa.com

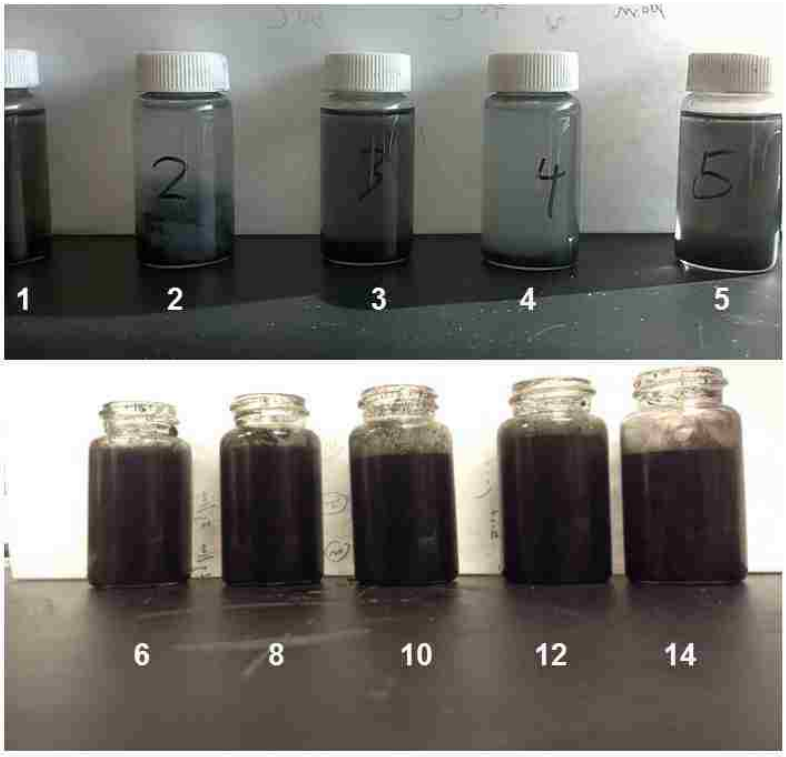

Figure 4.5 soot HLB testing results (corresponding to different HLB values)

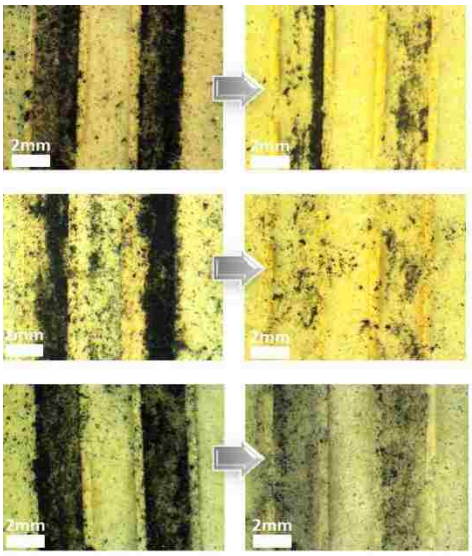

Figure 4.6 DPF channel wall before and after the optimized lab wash

www.manaraa.com

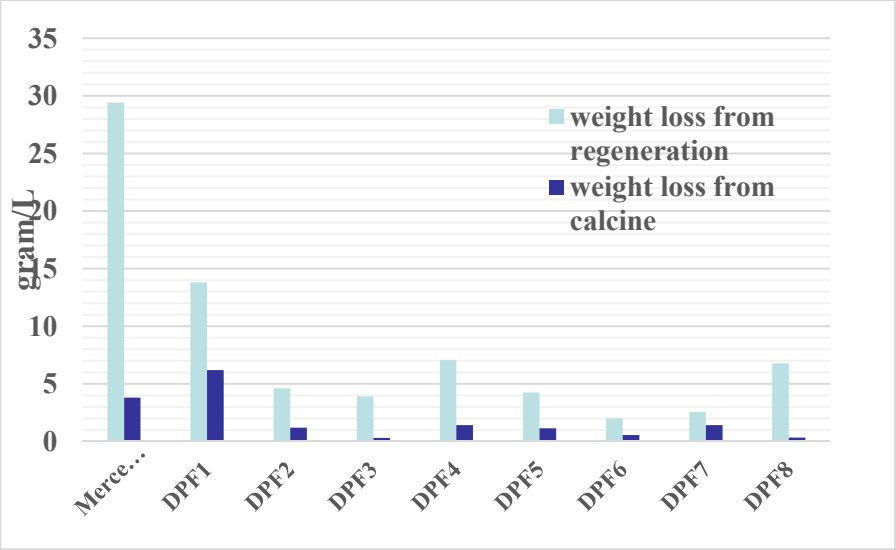

Figure 4.7 Full scale DPF wash performance: weight loss compared to calcine

Table 4.2 Full scale DPF wash performance table: weight loss compared to calcine

	DPF weight (lts)	Volume (L)	weight loss from H cleaning (g/L-substrate)	weight loss from calcine (g/L-substrate)
Mercedez DPF	18.92	2.5	28.5	3.6
DPF1	39.61	16.06	13	5.9
DPF2	39.41	16.06	4	1.7
DPF3	38.77	16.06	3.4	0.8
DPF4	38.2	16.06	7.06	1.41
DPF5	37.83	16.06	4.24	1.13
DPF6	37.82	16.06	2	0.56
DPF7	37.35	16.06	2.54	1.41
DPF8	38.13	16.06	6.78	0.33

www.manaraa.com

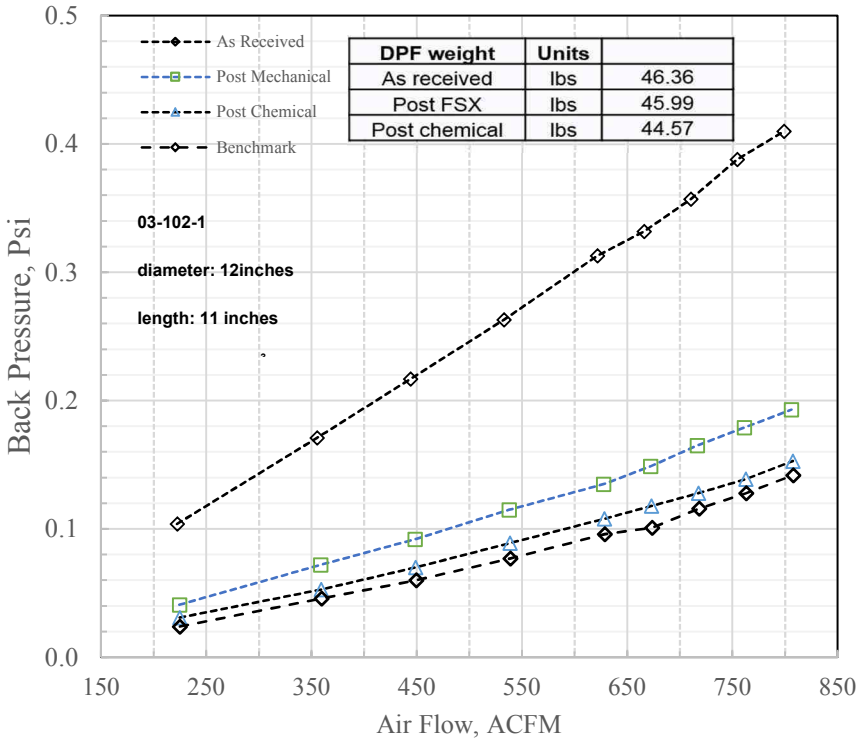

(a)

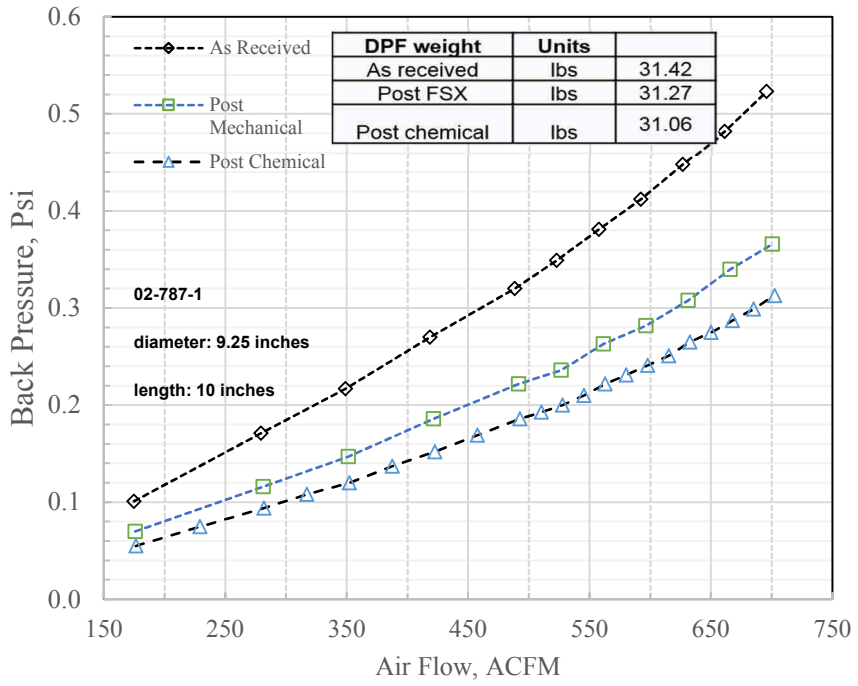

(b)

Figure 4.8 back pressure analysis of DPF post mechanic cleaning and post wash compared with benchmark DPF (a,b)

www.manaraa.com

4.4 Conclusion

This chapter gives a brief illustration of the lab-scale wash process development and full-scale DPF reclamation process. Results indicate certain kind of mixing wash can remove the metallic ash at high efficiency and protect the Pd/Pt at the same time. Self-assembled surfactant with a HLB value between 14-15 can remove the carbon soot that embedded in the DPF channel walls. Full-scale tests indicate the wash process can remove more than 80% of the DPF soot and ash, further reduce the back pressure by 15% than traditional FSX process. Moreover, although the back pressure can be reduced by FSX process, it cannot represent the cleaning condition of the exhausted DPF. Through two years of commercialized regeneration, the results show good consistency with high soot and ash removal efficiency.

Acknowledgement

This work herein was supported by PITA and cooperate with Hunsicker Emission Services, LLC. The data used in this chapter have been approved by the Hunsicker Emission Services, LLC in order to protect the PI's intellection.

4.5 References

Bardhan P., Mian WG., Angele JJS., Stevens A. (2008). "Method and system for removing ash from a filter." US Patent, No.: US 2008/0083334 A1.

www.manaraa.com

Ehlers M.S. (2010). “Diesel particulate filter (DPF) in chassis cleaning method.” US Patent: US7716922 B2.

Gregoire D.J., Colbura J.S. (2007). “Diesel particulate filter using microwave regeneration.” US Patent, No.: US7303602 B2.

Graskow B.R., Kittelson D.B., Abdul-khalek I.S., Ahmadi M.R., Morris J.E. (1998). “Characterization of exhaust particulate emissions from a spark ignition engine.” Fuel, 11-05.

Liati A., et al. (2013). “Metal particle emissions in the exhaust stream of diesel engines: an electron microscope study.” Environmental Science and Technology, 47(24): 14495-14501.

Vojtisek-Lom M., Czerwinski J., Lenicek J., Sekyra M., Topinka J. (2012). “Polycyclic aromatic hydrocarbons (PAHs) in exhaust emissions from diesel engines powdered by rapeseed oil methylester and heater nonesterified rapeseed oil.” Atmospheric Environment, 60: 253-261.

www.manaraa.com

Chapter 5

Improve DPF substrate materials by in-situ growth of SCNW matrix on porous SiC substrate

Abstract

An alternative SiC materials with SCNWs grown was developed from guar gum/silicon powder through Vapor-liquid-solid (VLS) method with Fe acted as catalyst. The mixing ratio, temperature which affect on the growth rate of SCNWs were investigated. Results indicated although anthracite and starchy can synthesized high purity SiC ceramics, these combinations did not transform the SiC into nanowires. SCNWs are being successfully grown from guar gum/silicon powder precursors at 1400ºC for 4hrs in an argon low rate of 1L/min, which produces a high purity product with about 100 nm to several micrometers in length. And the SCNWs has diameter around 40 nm. The iron catalyzed the grown by adsorbing the silicon and carbon vapor on the iron rich droplets on the tip. TEM analysis indicated the growth of SCNWs followed the [1,1,2] direction. And the synthesized SiC wafer has much higher hardness compared with commercialized cordierite substrate.

5.1 Introduction

This chapter the author successfully manufactured SCNWs through a novel organic precursor. In the previous chapter, the author illustrates details on both cordierite and SiC

www.manaraa.com

substrates and their advantages. Among these two substrate materials, cordierite is the preferred material as it offers ease of manufacture, low thermal expansion, and low cost. However, in the previous chapter, the author illustrated cordierite DPFs have been observed to fail pre-maturely during vehicle use; by pinholing, cracking, and melting when cordierite exposed to alkalis and metal components (CARB 2015, Yang K., 2016, Yang K., 2017).

Due to the early failure of common cordierite DPFs, SiC provides advantages of having a higher melting point, more favorable thermal conductivity, and is more chemically resistant to ash components under high temperatures (Miwa S., 2001, Adler J., 2005, Itoh A., 1993, Fukushima M., 2006). As a result, silicon carbide (SiC) diesel particulate filters (DPFs) offer superior chemical robustness compared to cordierite (Miwa S., 2001, Adler J., 2005, Itoh A., 1993, Fukushima M., 2006, Ohno K., 2000, Eom J.H. 2013). Besides to those advantages of porous SiC substrate, current SiC DPFs are more difficult, more expensive, and more energy intensive to manufacture than common cordierite which deter its commercial use (Warren Y.D., 2002; Miwa S., 2001, Adler J., 2005, Itoh A., 1993, Fukushima M., 2006, Ohno K., 2000, Eom J.H. 2013, Dey A., 2013). In addition, manufactured silicon carbide DPFs are limited in shapability and size, which require preformed modules to be cemented together (Adler J. 2005, Fukushima M., 2006,

www.manaraa.com

Dey A., 2013, Pomeroy M.J., 2012, Warren Y.D., 2002, Fredrich W.T., 2010, Guo W.M., 2012, Ohgushi S.T., 1999, Zhu S.M., 2007, Agrafiotis C.C., 2007). Due to the covalent nature of the SiC bond, the sintering of SiC ceramics requires very high temperatures, usually above 2000ºC, which makes it difficult to process the material compared to cordierite (Zhu S.M., 2007). Therefore, lowering the processing temperature to form porous SiC is a critical technological advancement which would further SiC material use in porous applications. When SiC is compared to cordierite which has an average density of 2.1 g/cm^3, the SiC is much heavier as the density is 3.1-3.2 g/cm^3, the higher density actually increases the cost to manufacture SiC DPFs because it requires more material to produce, which further deters the use of SiC (Adler J., 2005). The porosity and mean pore size of recrystallized SiC is also substantially lower than cordierite (Miwa S., 2001), commercialized silicon carbide substrate yields porosity less than 40% (Miwa S., 2001, Adler J., 2005, Itoh A., 1993, Fukushima M., 2006, Ohno K., 2000, Eom J.H. 2013). In addition to lowered porosity hindering overall filtration capacity, this low porosity also lowers thermal shock resistance.

Conventional SCNW Synthesis Methods

Conventional SCNW synthesis methods are presented as a mean to contrast the onerous nature or use of expensive precursors of most SCNW manufacturing methods. The most

www.manaraa.com

commonly methods are Vapor-solid (VS) and Vapor-liquid-solid (VLS). The silicon and carbon precursors first being vaporized at certain temperature, followed by deposit the vaporized molecules on the metal catalysts. The SCNWs finally grow with the leading of catalyst.

In this chapter, the author aims to present a new simple but effective in-situ synthesis route to prepare well-crystallized SCNW matrix acted as a potential DPF material. Compared to widely used cordierite substrate, the SCNW matrix studied here requires a relative short time (4 hours), simple equipment and cost-effective precursors (guar gum/silicon). The precursors, synthesis temperature was investigated during the current study. the SCNW matrix synthesized herein has networking structure, improved mechanical hardness, enhanced crystallinity, and favorable economics to advance the state of knowledge for diesel particulate matter filtration.

5.2 Material and Methods

(a) Materials

Silicon powder with purity of 99% were used as silicon raw material during the experiment. The silicon powder was purchased from Sigma Aldrich with particle size passed through US mesh # 300. Three different kind of carbon content materials were tested during the study. Guar gum powder (amorphous C^{-4}) used in this research were obtained from Sigma

www.manaraa.com

Aldrich with particle size passed through US mesh # 300 mesh in diameter. Anthracite fine (elemental C) with obtained from crushed anthracite coal and passed through US mesh # 300. Corn Starchy powder (amorphous C-4) used herein was purchased from Fisher Scientific with diameter of US mesh # 300. The collagen based binder was provided by Entelechy, All the samples made from the materials listed above were mixed with deionized water.

(b) Precursor material preparation

The silicon powder was first mixed with the carbon containing materials, namely anthracite fine, starchy powder and guar gum powder separately. For anthracite-silicon mixture, collagen was used as binder. The collagen was first dissolved into warm deionized water and then add to the anthracite-silicon mixture. For starchy-silicon, guar gum-silicon mixture, no binding materials is needed as starchy and guar gum itself can act as binder when dissolved in deionized water. So simply add the deionized water to starchy-silicon and guar gum-silicon mixture will form a gelation like slurry. The detail recipes are indicated in Table 5.1. The slurry then packed as a piece of wafer and cured under 105^{o}C for 48hrs. different water level were tested for guar gum-silicon mixtures. Materials that contain three different ratios of anthracite: silicon were tested during the experiment.

www.manaraa.com

Table 5.1 sample description and recipes

sample No.	carbon source	silicon source	other additives
1	3g of guar gum	3g silicon powder	10 ml deionized water+0.05% $FeSO_4$
2	5g of guar gum	3g silicon powder	10 ml deionized water+0.05% $FeSO_4$
3	10g of guar gum	3g silicon powder	10 ml deionized water+0.05% $FeSO_4$
4	10g of starchy	3g silicon powder	10ml deionized water+0.05% $FeSO_4$
5	2g of anthracite fine	3g silicon powder	2.5ml 10% collagen+0.05% $FeSO_4$
6	1.5g of anthracite fine	3.5g silicon powder	2.5ml 10% collagen+0.05% $FeSO_4$
7	2g of anthracite fine	1g silicon powder	2.5ml 10% collagen+0.05% $FeSO_4$

(c) Pyrolysis

Cured samples were pyrolyzed in a MTI tube furnace with maximum temperature of 1400ºC (MTI GSL 1500X). after evacuation of the alumina chamber to about 0.1 Torr, the samples were inserted into an alumina oxide tube with a slow argon gas flow 1L/min used to prevent the material from burning. First the furnace was ramped up to 1400ºC with a rate of 5ºC/min, followed a thermal stable state. The thermal stable state takes 4 hrs under 1400ºC and then cool down at the same cooling rate of 5ºC/min. Both the ramping and cooling down steps take 280 minutes each. After the thermal treatment, samples were

www.manaraa.com

removed from the furnace for further analysis. The rate was kept under 10°C/min in order to reduce the thermal shock to both the furnace and the alumina oxide tube.

(d) Characterization

SEM – EDS

The morphology of samples before and after pyrolysis were performed on Scanning Electron Microscopy (SEM) equipped with an Electron Dispersive Spectroscopy (EDS) (HITACHI 4300). The instrument was operated under high vacuum with a secondary electron detector. The accelerating voltage was set as 15 KeV throughout the analysis.

XRD analysis

Phase identification of various samples were analyzed by an ambient X-Ray Diffractometry (XRD) (XRD, Rigaku, D/max-2C, Japan) using Cu Ka1 radiation, operating voltage of 30 KeV and current of 15 mA. The diffraction patterns were collected for 2ɵ between 10^{o} to 80^{o} with a step of 0.01^{o}. The XRD results were then analyzed by MDI Jade 6.5. The samples were first crushed into powders by a mortar and pestle and then the powders were placed into an aluminum sample holder. Thus, the powder XRD pattern offered a bulk measurement and represented the average situation in the samples.

TEM

www.manaraa.com

The detailed structural feature and chemical composition of the SiC nanowires were further characterized using transmission electron microscopy (TEM) operated at 300 KeV (Model JEOL 1200). The samples for TEM analysis were prepared by first ultrasound dispersed the SiC nanowire sample into pure ethanol. Then drop a suspension of the sample onto a Cu grid. The Cu grid then dried under temperature of 50^{o}C for 24hrs before went to test.

Micro hardness

Micro hardness as reported here in Vickers hardness (HV) was measured by an Leco micro hardness tester (LM 110). The indented loading is 1 kg. Each sample was prepared via embedded into an epoxy resin. The epoxy resin was allowed to cure for 24 hrs. Then the sample was ground and polish with 6 and 3 um diamond paste coated polishing pads. Select a rectangular area on the samples followed by indent and mapping the micro hardness throughout the area.

5.3 Results and Discussions

(I) Effect of different precursor

Effect of different precursor compositions on the growth of SCNW was shown in Figure 5.1. Figure 5.1(a, b) shows the wafer sample structures of optimized Silicon/guar gum composition (10g guar gum/3g silicon powder). Figure 5.1(c ,d) and Figure 5.1(e, f) shows

www.manaraa.com

the starchy/silicon combination (10g/3g) and anthracite fine/silicon composition (2g/1g), respectively. Figure 5.1a provides an overview of the SiC wafer, it is manifest that the SiC wafer was encapsulated by the cotton-like SCNWs in the low magnification SEM image. These nanowires grew on the wafer with length range from 10 to several hundred micrometers and altered the color of the wafer from black to light grey (Figure 5.1b). The similar structure does not show up for starchy and anthracite fine as indicated in both low magnification and high magnification SEM images. For all the three kinds of precursors, the small particles were sintered into large piece of ceramics with highly porous structure. However, when zoom in and focused on a small scale on the wafers, it is obviously that guar gum/silicon compositions create a labyrinth of SCNWs compared with other samples. For the anthracite fine/silicon sample, less amount of SCNWs are found and growth on the big chuck of anthracite particles. And instead, least amount of SCNWs are observed and partial of the wafer surface was vitrified as indicated in Figure 5.1c, d.

www.manaraa.com

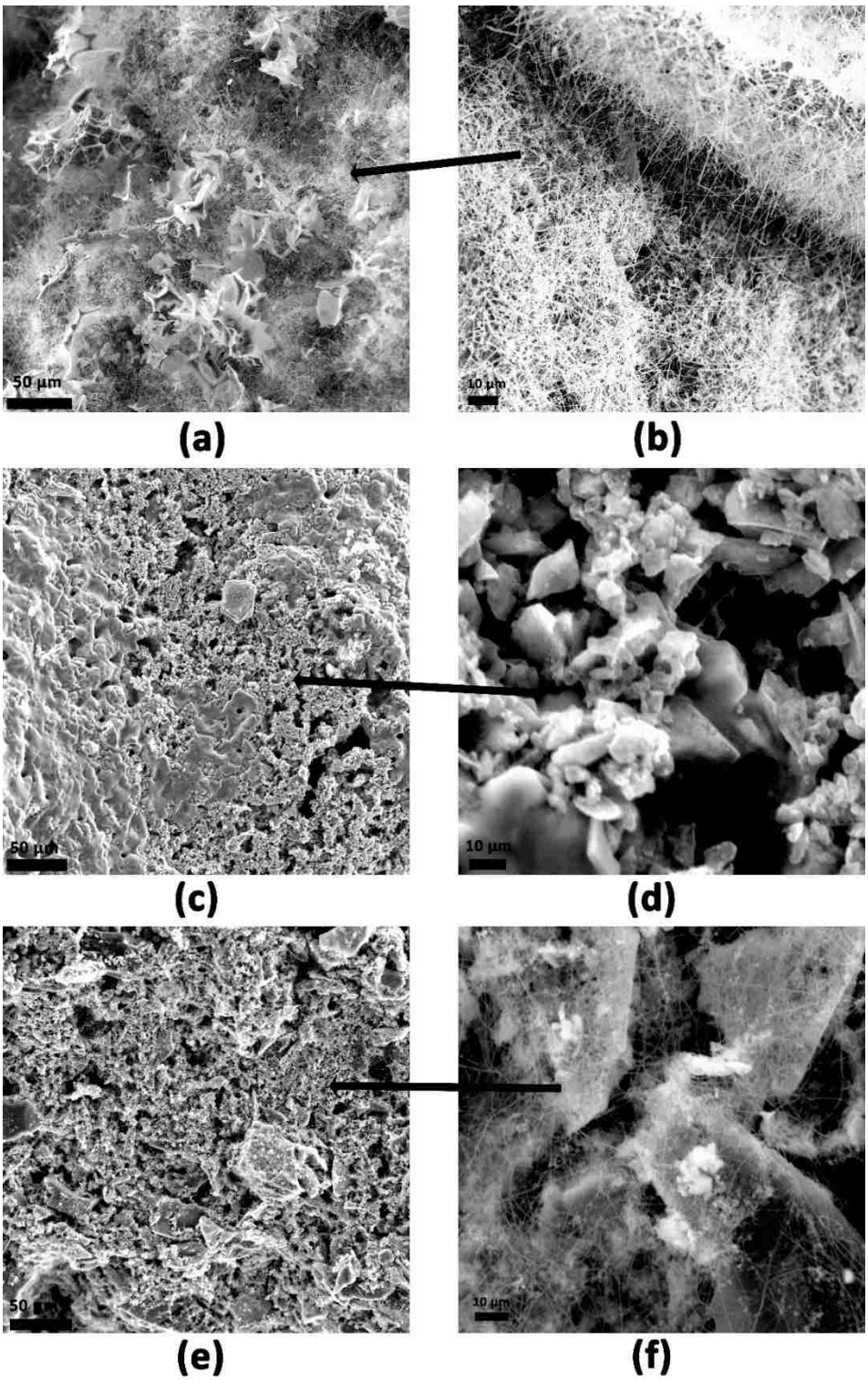

Figure 5.1 SCNWs matrix wafer produced from different precursors: (a, b) guar gum/silicon powder 10:3 ratio; (c, d) starchy/silicon powder 10:3 ratio; (e, f) anthracite fine/silicon powder, 2:1 ratio.

www.manaraa.com

(II) Surface morphology changes of optimized SiC wafer

Figure 5.2 indicated the optimized surface microstructure of SiC wafer from low magnification to high magnification. The images magnification increases from left to right. After pyrolysis, the surface is highly porous with sphere structure pores covered on the surface. Obviously SCNWs were grown from the inner and outside of the pore structures (Figure 5.2a). Numerous SCNWs cross-linked and twisted together to form a networking structures as indicated in Figure 5.2c. The grown SCNWs significantly increases the surface area which further facilitate the soot and ash capture capacity if used in diesel after treatment system.

The only crystalline phase indicated in the XRD analysis before pyrolysis is Si since guar gum is organic polymer with amorphous structure (Figure 5.3). The main crystalline phase is SiC after pyrolysis, followed by minor crystalline phases of FeSi and untreated Si. The FeSi is an intermediate state produced from the catalyzed reaction involving iron. Therefore, the existence of FeSi confirmed the iron catalyzed reaction. This was further confirmed by Vakifahmetoglu (2010), who also found the iron silicide, especially FeSi, Fe_3Si are the predominant phase in the temperature of 1400^{o}C in the iron catalyzed SCNW growing reaction (Vakifahmetoglu 2010).

www.manaraa.com

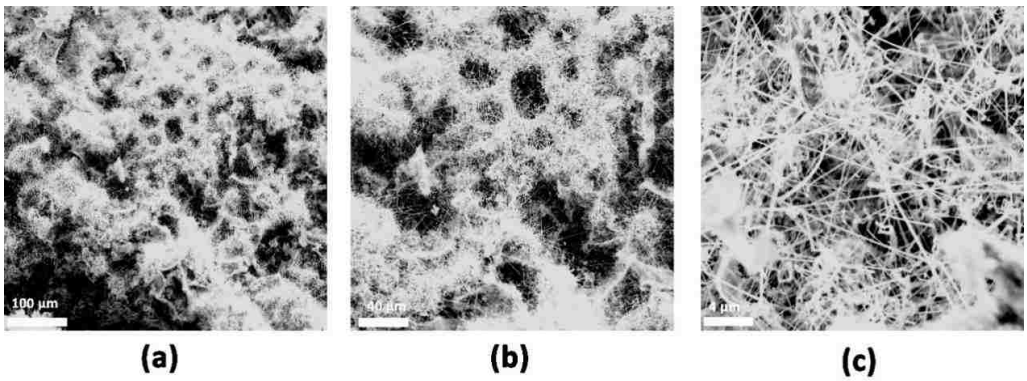

Figure 5.2 SCNW matrix growth from guar gum/silicon combination at a ratio of 10:3 after the pyrolysis

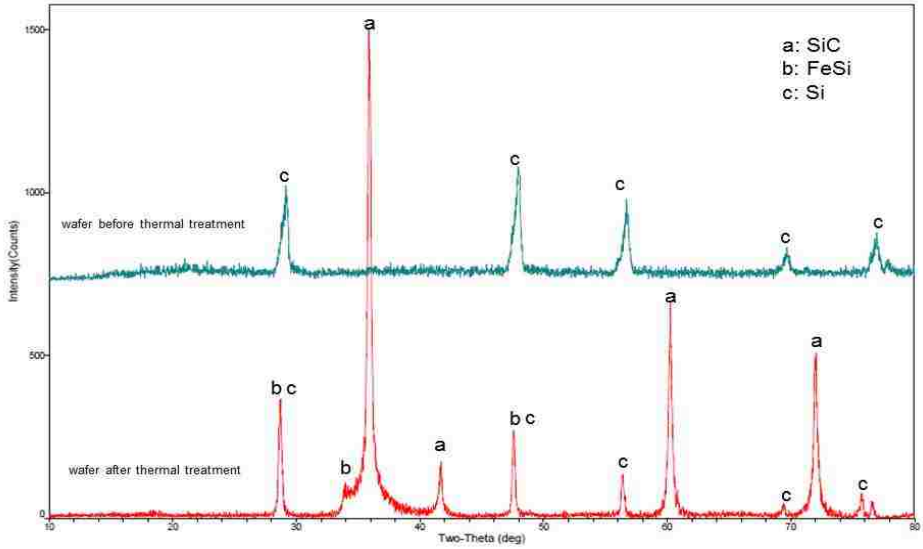

Figure 5.3 XRD profiles of guar gum/silicon combination before and after pyrolysis.

(III) Effect of Si-guar gum ratio on the growth of SiC nanowire

Figure 5.4 indicated that the increasing ratio of guar gum to Silicon would facilitate the growth of SCNWs. For the ratio of 3g:3g, the carbon source is not enough to create carbon vapor to deposit on silicon particle and there is only tiny amount of

www.manaraa.com

SCNWs growth from the surface (Figure 5.4a). With increasing the guar gum partition, the SCNWs start to grow from the silicon particle surface, continuously grow to longer nanowire and finally twisted together to form matrix structures as indicated in Figure 5.4c. Since the guar gum has lower melting and vaporize temperature compare to silicon powder, the guar gum first creates carbon vapor at low temperature then deposit on the melted silicon particle to produce SCNWs. Therefore, the increasing in guar gum partition would facilitate the formation of SCNWs and reducing the silicon particle size as indicated in Figure 5.4. The XRD results shown for all three-different guar gum/silicon ratio, the main crystalline phases are SiC, followed by minor crystalline phase of FeSi. The Si crystalline phase reduced by increasing the guar gum/silicon ratio, and finally disappeared when the ratio reaches 10 to 3 (Figure 5.5 and table 5.2). Therefore, for both ratios of 3:3 and 5:3, there are unreacted Silicon existed (Figure 5.5 and table 5.2). As the climbing up of the temperature, the melting point of Silicon is much higher than guar gum, so partial guar gum is wasted during this step, which results in the unsaturated reaction of silicon in both ratio of 3:3 and 3:5.

www.manaraa.com

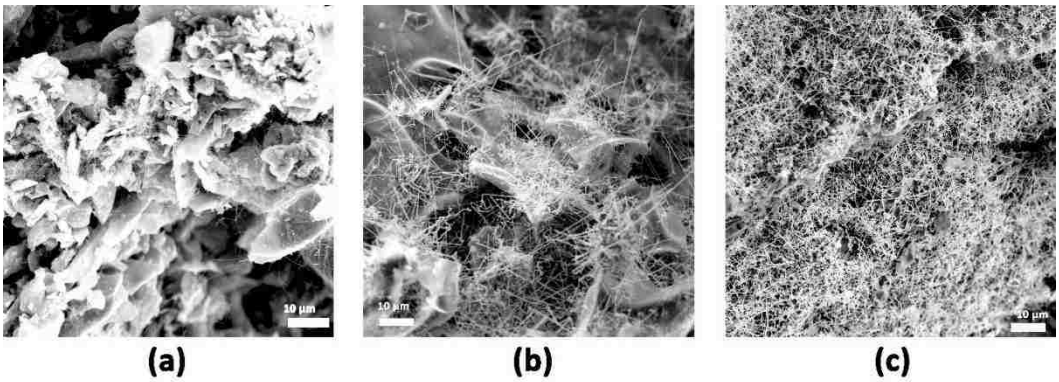

Figure 5.4 SEM images of SCNWs from variable guar gum/silicon powder ratio. (a)3g:3g (b) 5g:3g (c) 10g:3g.

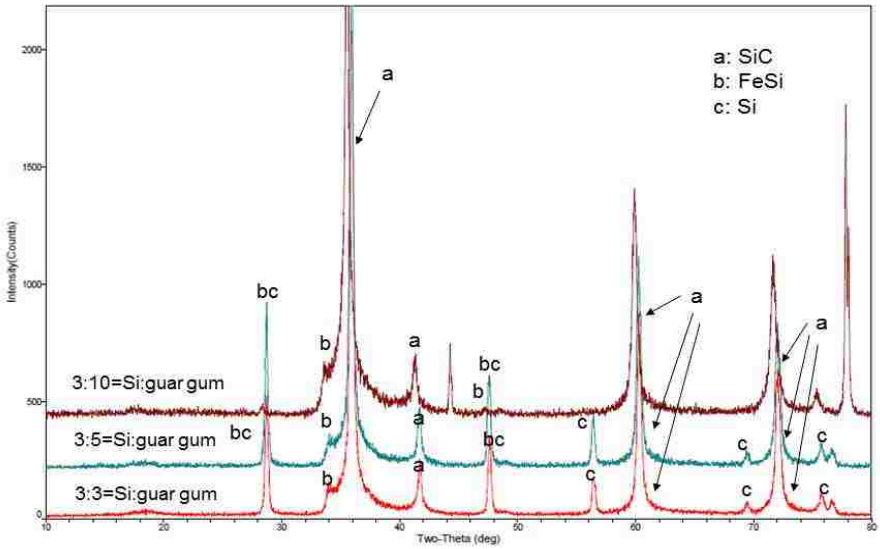

Figure 5.5 XRD profiles of pyrolyzed wafers with different guar gum/silicon powder ratio.

Table 5.2 XRD results: Principles crystalline phases of SiC wafers with different guar gum:silicon ratio.

guar gum:silicon	crystalline phase		
3:10	SiC (h)	FeSi (m)	
3:5	SiC (h)	FeSi (m)	Si (m)
3:3	SiC (h)	FeSi (m)	Si (m)

www.manaraa.com

(IV) Effect of temperature on the growth of SCNW

According to Figure 5.6, as the temperature increases from 900ºC to 1400ºC, the amount of SCNWs growth on the guar gum/silicon wafer increases significantly. And the guar gum particles and silicon particles were sintered into larger ceramic features that crosslinked the neighboring particle together when temperature increases from 900ºC to 1400ºC. The SCNWs grow to be longer and thick as the temperature increased as indicated in Figure 5.6d. The shinning spots on the tip of SCNWs as shown in Figure 5.7b acted as the "seeds" to leading the nanorod grows. Figure 5.7b demonstrated a typical microstructure of growing seed and its EDS spectra. It is manifest that the tip of the nanorod shown a spherical structure with diameter around 1μm, much larger than the thickness of the nanorod connected with it. EDS analysis indicate higher concentration of iron (35-40 % in weight concentration) and the iron tend to accumulate in the tip compared to the rest area of the SCNWs (Figure 5.7b). For reference, the main body of the SCNW has no iron detected in the nanowire, as shown in Figure 5.7a. similar to the growing mechanism of carbon nanotube which proposed by Helveg (2004). The SCNW growth mechanism can be explained by a VLS reaction. The guar gum and silicon

www.manaraa.com

powder pyrolysis will produce supersaturated CO and silicon vapor, the top and bottom of melted iron particle have different temperature and accommodation coefficient for CO/silicon vapor, which drive the growth of SCNWs (Zhu 2005). This can further explain why the iron was only detected on the tip of the nanowires. The reaction proposed is as follows:

$$3Si\ (Vapor)+2CO\ (vapor) \xrightarrow{FeSO4} 2SiC\ (solid)+SiO_2(solid)$$

The iron catalyzed reaction was confirmed by the previous researches by Vakifahtoglu (2010), who used $FeCl_2$ as catalyst. $FeCl_2$ was first reduced to metallic Fe nanoparticles, then react with Silicon to yield iron silicide including FeSi, Fe_3Si. And the iron silicide was not disappeared during the formation of SiC nanowire (Vakifahtoglu 2010), which was indeed consensus to the XRD profiles indicated in Figure 5.9 and table 5.3, that FeSi peaks first shown up when temperature reaches 1200ºC, and further increasing at temperature 1400ºC. Carbon was dissolved in the FeSi flux due to the FeSi has large accommodation coefficient, which acted as a preferred site for Si and CO vapor to deposit.

Figure 5.8a and b shows the TEM images of the SCNWs with low magnification. Figure 5.8a shows the SCNWs with different morphologies, some

www.manaraa.com

are straight line, other thinner nanowires are bended and twisted with other nanowires nearby. The stacking fault was found in the SiC nanowire as indicated in the TEM results (Figure 5.8c). And the stacking fault was perpendicular to the growing direction of SiC nanowire as indicated in figure 5.8c. The presence of stalking fault further confirmed that the growth of SiC nanowire is leading by FeSi and accumulated through a layer structure. The selected area electron diffraction pattern (SADP) as shown in figure 5.9d confirmed the grow of SiC nanowire followed the [1,1,2] direction. From the TEM image, it is clearly that the SCNW possessed a core/shell structure, with SiO_2 encapsulate the SiC core. Further, the XRD profile confirmed the SiO_2 was in amorphous structure (Figure 5.8). The average diameter of the SCNW is around 50 nm which is in agreement with Li (2010) research. There was not any branching phenomena shown in the growth of SCNW, each SCNW grows separately towards different directions and twisted together to form a cotton-like structures (Figure 5.8).

Considering the temperature effect, the SiC peaks in the XRD profile increased significantly from 900^{o}C to 1400^{o}C (Figure 5.9). The increasing in SiC peaks indicated the continuously reaction between Silicon and guar gum and higher

www.manaraa.com

crystallinity by increasing temperature. At 1400ºC, the high and sharp SiC peaks indicated the high purity of SiC crystalline phase produced by silicon and guar gum.

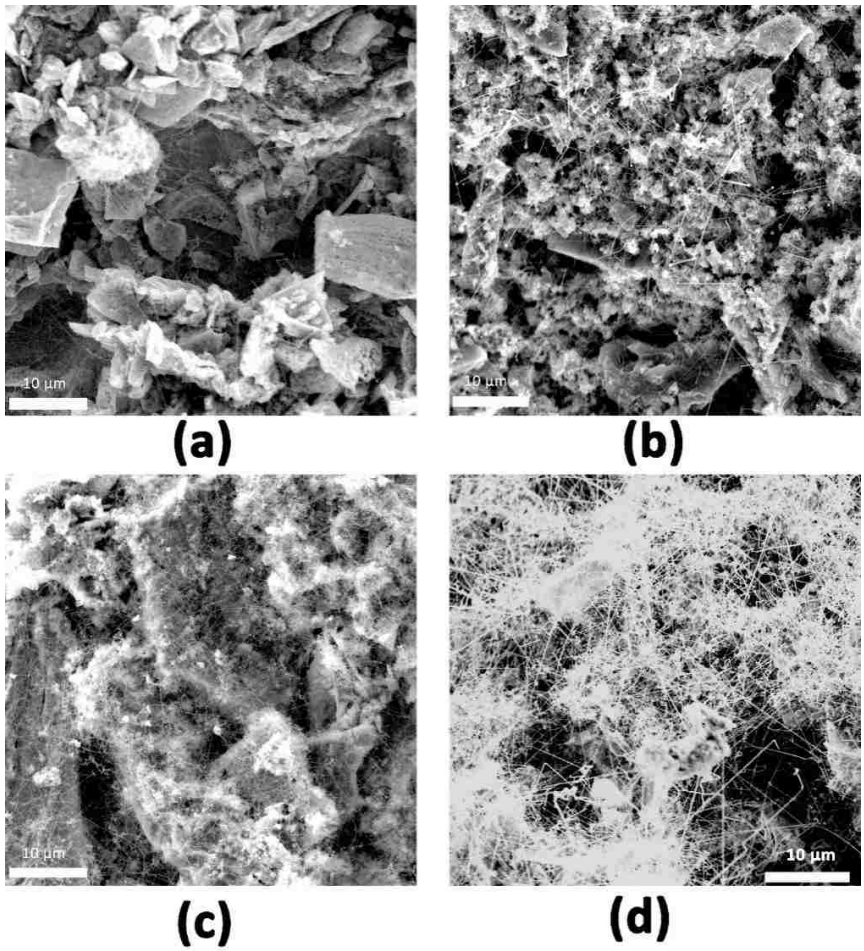

Figure 5.6 Different morphologies of pyrolyzed SiC wafers under different temperature. (a) 900ºC; (b) 1100ºC; (c) 1200ºC; (d) 1400ºC for 4hrs. (guar gum/silicon powder=10g:3g)

www.manaraa.com

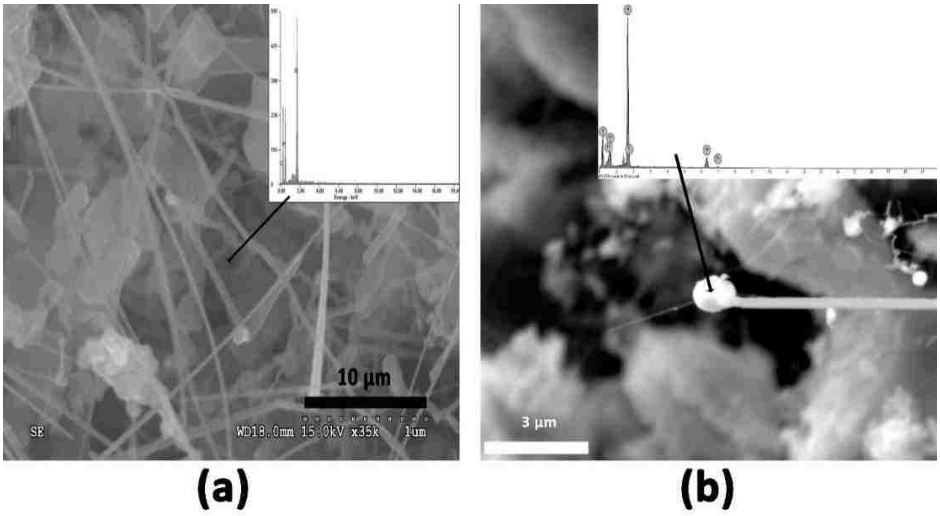

Figure 5.7 EDS spectra of the SCNW tip (growing seed).

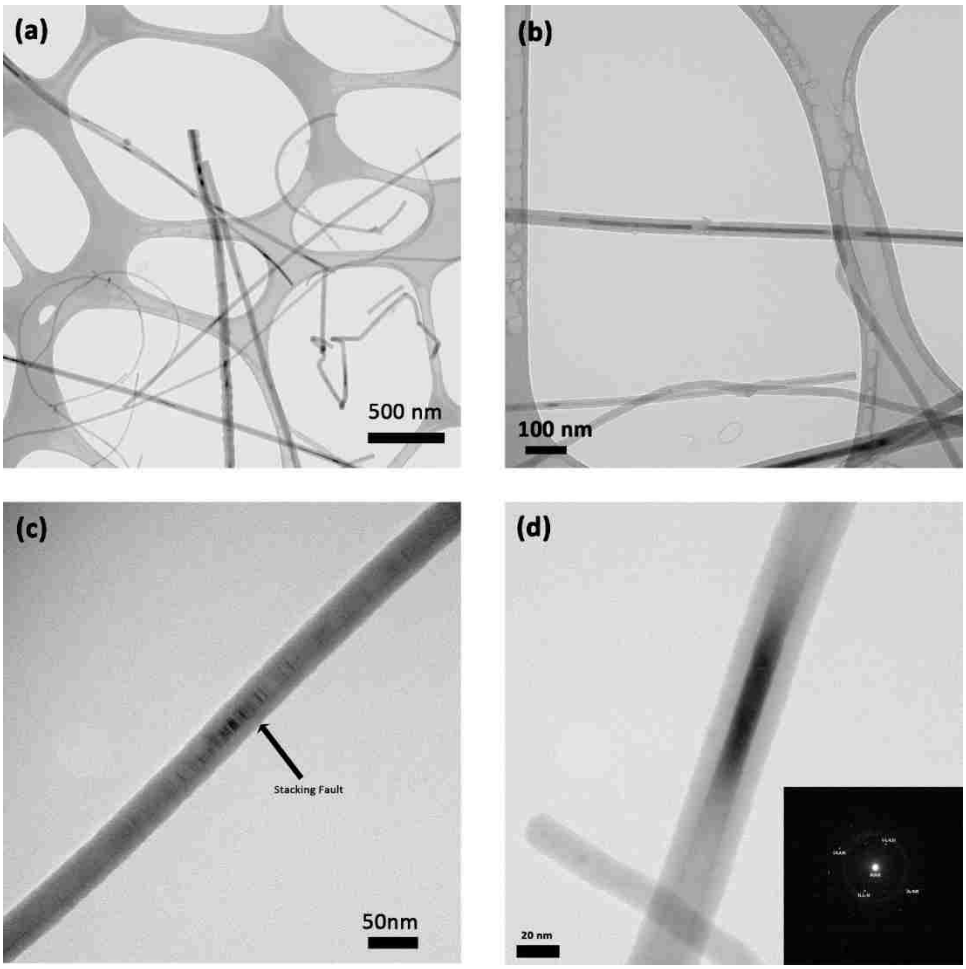

Figure 5.8 EDS line scan of SCNW (a); TEM image of multiple SCNWs (b), single SCNW (c), and its corresponding SAPD pattern.

www.manaraa.com

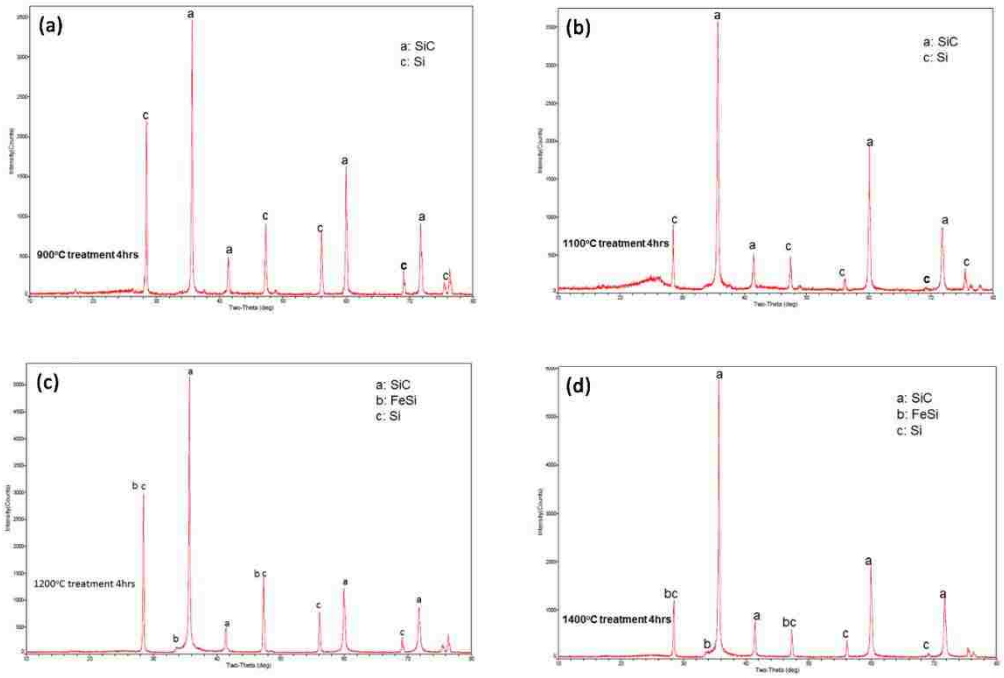

Figure 5.9 XRD profiles of SiC wafers (guar gum/silicon=10g:3g) under elevated temperatures: a. 900°C, b. 1100°C, c. 1200°C, d. 1400°C

Table 5.3 XRD results: Principle crystalline phases of SiC wafers under elevated temperatures

Temp. (°C)	crystalline phase		
900	SiC (h)	Si (h)	
1100	SiC (h)	Si (m)	
1200	SiC (h)	FeSi (m)	Si (m)
1400	SiC (h)	FeSi (m)	Si (m)

(V) Hardness

www.manaraa.com

The material hardness is very important for ceramics in order to be used commercialized. Figure 5.10 shows the hardness mapping of guar gum derived SiC (b) and commercial DPF made by cordierite (a). Results indicated the average hardness for cordierite substrate is obviously lower than SiC wafer as majority of the cordierite surface hardness is located in the "red zone". As a comparison, most of the SiC wafer hardness is located in the "green zone". The average Vickers hardness as shown in the mappings are 428 HV/1kg for SiC wafer and 219 HV/1kg for commercial cordierite substrate. Therefore, the guar gum However, it is necessary to mention that the commercial made cordierite substrate is more homogeneous compared to SiC wafer. This problem should be solved in our future research.

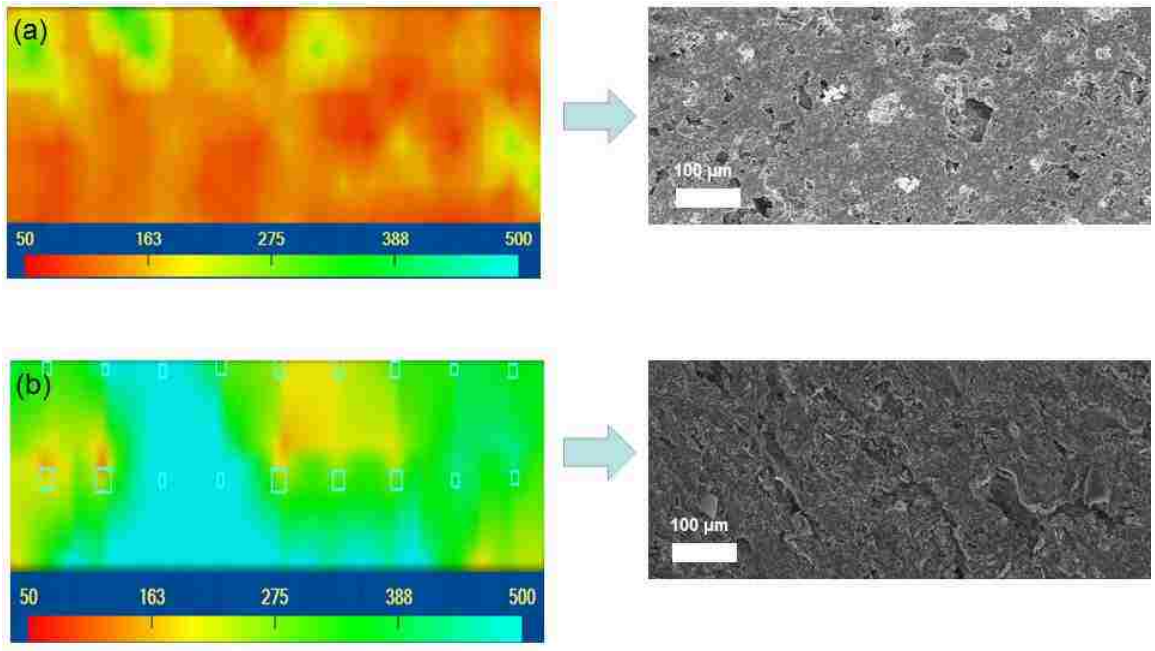

Figure 5.10 micro hardness mappings of SiC wafer manufacture by guar gum/silicon powder=10g: 3g (b) compared to cordierite substrate (a)

www.manaraa.com

5.5 Conclusion

In the current study, a novel method was developed based on low cost precursor to grow SCNWs matrix on SiC wafer. Easily accessible guar gum and silicon powder was acted as precursor and catalyzed by iron via VLS method at 1400^{o}C. The manufactured SiC wafer has porous structures which facilitate its application in vehicle emission after treatment system. Compare with other low-cost precursors, the guar gum/silicon combination provide the best growth of SCNW matrix. And further, the guar gum acted as both carbon source and binding material during this process. The guar gum offers a convenient way to shaping the SCNW material into any kinds of structures including monolith structure, honeycomb structure, etc. The growth rate of SiC nanowires increases with increasing temperature from 900^{o}C to 1400^{o}C. The XRD results indicated the optimized temperature is 1400^{o}C and the iron catalyzed the reaction by forming an intermediate product FeSi. This iron catalyzed reaction was further confirmed by the SEM image as the growing tip contain higher concentration of iron compared to the rest area. The silicon and carbon vapor is tending to deposit on the liquidified iron ball and leading the growth of SCNWs. The manufactured SCNWs has average diameter around 20 to 100 nm with length of several tens micrometers. The

www.manaraa.com

single crystal SiC nanowires growth along the [1,1,2] direction. The high purity SiC nanowires with an amorphous SiO_2 layer on their surface were synthesized through the VLS reaction. The synthesized SCNW wafer has much higher hardness compared to commercialized cordierite substrate. Overall, This novel SCNW matrix provides a potential low-cost and easy accessible way to substitute the currently used cordierite substrate in the field of emission after treatment system.

5.6 References

Adler J. (2005) "Ceramic diesel particulate filters. International applied ceramic technology," International journal of applied ceramic technology, 2:429-439.

Agrafiotis C.C., Mavroidis, I., Konstandopoulos, A., Hoffschmidt, B., Stobbe, P., Romero, M. (2007) "Evaluation of porous silicon carbide monolithic honeycombs as volumetric receivers/collectors of concentrated solar radiation." Solar energy materials and solar cells. 91:474-484.

California Air Resource Board. Evaluation of Particulate Matter Filters in On-Road Heavy-Duty Diesel Vehicle Applications. May, 2015. http://www.arb.ca.gov/msprog/onrdiesel/documents/DPFEval.pdf

Dey A., Kayal, N., Chakrabarti, O., Caldato, R., Andre, C., Innocentini, D. (2013) "Permeability and nanoparticle filtration assessment of cordierite bonded porous SiC ceramics." Industrial and Engineering chemistry research. 52:18362-18372.

Eom J.H., KIM Y.W., Raju S. (2013) "Processing and properties of macroporous silicon carbide ceramics: A review." Journal of Asian ceramic societies. 1:220-242.

www.manaraa.com

Fredrich W.T., Wolff, T., Johannesen, L., Hajireza, S. (2010) “A new approach to design high porosity silicon carbide substrates.” SAE International. 2010-01-0539.

Fukushima M., Zhou, Y., Yoshizawa, Y., Hirao, K. (2006) “Preparation of mesoporous silicon carbide from Nano-sized SiC particle and polycarbosilane.” Journal of the Ceramic society of Japan. 114:571-574.

Guo W.M., Xiao, H., Xie, W., Hu, J., Li, Q., Goa, P. (2012) “A new design for preparation of high performance recrystallized silicon carbide.” Ceramic International. 38:2475-2481.

Helveg S., Cartes C.L., Sehested J., Hansen P.L., Clauson B.J., Nielsen J.R.R., Pedersen F.A., Nerskov J.K. (2004) “Atomic scale imaging of carbon nanofiber growth.” Nature. 427:426-429.

Itoh, A., Shimato, K., Komori, T., Okazoe, H., Yamada, T., Nimura, K., Watanabe, Y. (1993) “Study of SiC application to diesel particulate filter (part 1): material development.” SAE International, No.: 930360.

Miwa S., Abe, F., Hamanaka, T., Yamada, T., Miyairi, Y. (2001) “Diesel particulate Filters made of newly developed SiC.” SAE International. 2001-01-0192

Ohgushi S.T., Sakaguchi, S., Suzuki, S., Kita, H., Ohsumi, K., Suzuki, T., Kawarmura, H. (1999) “Development of high durability diesel particulate filter by use SiC fiber.” SAE International, 1999-01-0463.

Ohno K., Shimato, K., Taoka, N., Santae, H., Ninomiya, T., Komori, T., Salvat, O. (2000) “Characterization of SiC-DPF for passenger car.” SAE-International. 2000-01-0185.

www.manaraa.com

Vakifahmetoglu C., Pippel E.H., Woltersdorf J., Colombo P. (2010) "Growth of one dimensional nanostructures in porous polymer derived ceramics by catalyst assisted pyrolysis. Part 1: iron catalyst." Journal of American ceramic society. 93:959-968.

Warren Y.D., Gadkaree C., Johannesen L. (2002) "Silicon carbide for Diesel particulate filter applications: material development and thermal design." SAE International. 2002-01-0324.

Yang K., Hunsicker R., Fox J. T. (2016) "Characterizing Diesel Particulate Filter Failure due to Pinholes, Melting, Cracking, and Fouling." Emission Control Science and Technology. 2:145-155.

Yang K., Fox J.T., Hunsicker R. (2017) "Interaction of Fe, Na and K with porous cordierite at elevated temperature," journal of materials science. 52:4025-4041.

Zhu S.M., Ding, S., Xi, H., Li, Q., Wang, R. (2007) "Preparation and characterization of SiC/Cordierite composite porous ceramics." Ceramic International. 33:115-120.

www.manaraa.com

Chapter 6

Reclamation of DPF soot used as adsorbent for Cu, Cd and Cr compared with commercial activated carbon

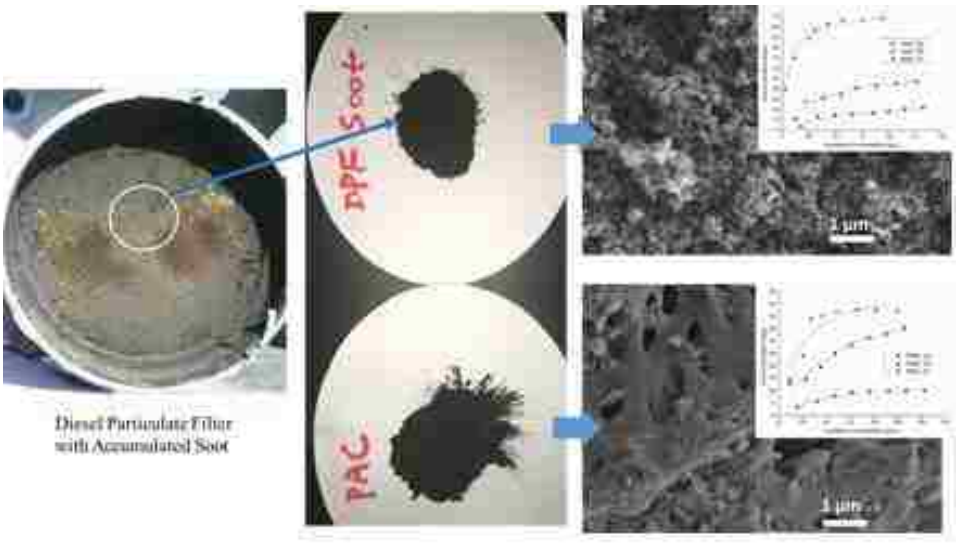

Abstract

The use of carbon soot recovered from Diesel Particulate Filters (DPF) has been investigated as a potential adsorbent for heavy metals including cadmium, chromium and copper from wastewater. Results were compared with the adsorption performance of powder activated carbon (PAC). The uptake capacity of heavy metals for soot were found to be higher than PAC. And the thermodynamic study result for both soot and PAC indicated the adsorption procedures are exothermic. The adsorption studies were carried out for both single and binary systems. The data are best modeled by the monolayer model

www.manaraa.com

and Langmuir isotherm model for single systems. The adsorption mechanisms are more complex for binary systems. The kinetic studies indicated the adsorption happens rapidly within the first 1 hour and the results can be best modeled by pseudo-second-order model. The SEM-EDS analysis revealed the soot possesses higher porosity and surface area. Carboxylic and hydroxyl functional groups are the predominant surface functional group on both soot and PAC as revealed by FTIR and IEP values. The adsorption can be explained by both Van Der Waals force and electrostatic force.

6.1 Introduction

Mining, electroplating, metal processing, power generation, textile and battery manufacturing are the predominant industrial sources of heavy metals, which include Pd, Cd, Cu, Cr, Hg, As, Mg, and Zn, among others (Amarasinghe B.M.W.P.K. 2007;Wang X.S., et al. 2011; Zhou D.M., et al. 2010; Mishra P.C. 2009). Once these heavy metals are released into the environment, they can accumulate in plants, animals or drinking water and have the potential to negatively affect the blood system, lungs, kidneys and the central nervous system in humans (Amarasinghe B.M.W.P.K. 2007; Zhou D.M., et al. 2010). Due to the fact that heavy metals can produce both mutagenic and carcinogenic outcomes to

www.manaraa.com

humans and aquatic organisms, the United States Environmental Protection Agency (USEPA) has strict regulation controls heavy metal water pollution (Mohan D. 2002; Cho D.W., et al. 2011). For example, the maximum contaminant level (MCL) for drinking water enforced by the USEPA is 0.005 mg/L for Cd, 0.1 mg/L for Cr, 1.3 mg/L for Cu (USEPA. 2009).

Due to the human health risk, numerous technologies have been developed and applied to eliminate heavy metals from aqueous systems. Chemical precipitation followed by coagulation has been employed for the removal of heavy metals at water and wastewater treatment plants, but is not practical for point-of-use application. Ion exchange resin and membrane filtration are both efficient ways to remove heavy metals but ion exchange resin requires complicated water pretreatment and the fouling problem associated with membranes discourages the use of these technologies (Amarasinghe B.M.W.P.K. 2007; Wang X.S., et al. 2011). Other treatment technologies include: oxidation/reduction, dialysis/electrodialysis, electrolytic extraction are also applied to remove heavy metal or reduce its toxicity (Mohan D. 2002). However, those treatment technologies suffer the problem of high cost (Mohan D. 2002). Adsorption is a non-selective way to remove organic pollutants and trace amount of heavy metals from water with low cost. The

www.manaraa.com

adsorption process is generally considered highly effective, easy to operate and easy to access (Mohan D.2002).

Over the past century numerous adsorbents have been developed in order to treat heavy metals in water. Activated carbon is created by carbonizing organic materials including coconut shells, anthracite coal, bituminous coal, nut shells, and wood. The resultant activated adsorbent is the most widely used due to large surface area, microporous structure, and affordability (Mohan D. 2002). Activated carbon can be widely used in odor removal, de-coloration, gold recovery, mercury removal at coal power plants, and solution purification (Mohan D. 2002). However, with regard to heavy metals, commercial activated carbon suffers the problem of low adsorption capacity and selectivity for the heavy metals (Mahvi A.H., et al. 2005). For those reasons, many studies have been carried out to develop effective substitutes and low cost adsorbents (Srivastava S.K., et al. 1989; Mellah A. 1997; Jiang M.Q., et al. 2010; Rao R.A.K. 2016; Okiemen F.E., et al. 1991; Cheung C.W., et al. 2000). The activated carbon substitute should be easily accessible, economically feasible and highly effective. Therefore, many naturally occurring materials have been tested for their affinity to remove heavy metals from aqueous systems.

Natural montmorillonite clay was used to remove Pd and Cd from water, with adsorption capacities of 0.68mg/g for Pb and 0.72 mg/g for Cd (Srivastava S.K., et al.

www.manaraa.com

1989). Natural bentonite was found to remove zinc from water with an adsorption capacity of 52.91 mg/g (Mellah A. 1997). One study conducted by Jiang MQ (2010) revealed that the adsorption capacity for Pb, Cd, Ni and Cu from water, on natural kaolinite was 4 mg/g for Pb, 2.4 mg/g for Ni, 3 mg/g for Cd and 1.8 mg/g for Cu (Jiang M.Q., et al. 2010). The adsorption capacity of Cd contaminated water was quantified as 27.27 mg/g according to the study using clay balls by Ali Khan Rao (2016) (Rao R.A.K. 2016). Natural peanut husks were appraised to possess Cd adsorption capacity of 0.36mmol/g and Pb capacity of 0.19 mmol/g (Okieimen F.E., et al. 1991). Bone char was applied to remove Cd from water with a maximum adsorption capacity of 0.534 mmol/g as reported by Cheung C.W (2000) (Cheung C.W., et al. 2000).

Carbon black is a commercially significant carbonaceous component intentionally produced by the incomplete combustion of an organic precursor such as coal or other fossil fuel (Street D.G., et al. 2001). Carbon black is also created as an undesirable by-product of the combustion of coal and fossil fuels, which is a main component of $PM_{2.5}$ (Hamilton R.S. 1991). In the previous chapter, the author demonstrates that more than 90% of the carbon black can be classified as PM2.5 and the main source of carbon black is diesel vehicles (Viidanoja J., et al. 2002). Since more than 90% of carbon black or soot as well as the ash can be captured by the DPF (Sappok A., et al. 2009), the DPF need to be

www.manaraa.com

periodically removed the carbon black and ash from the DPFs. The loading of soot in a DPF removed for cleaning was measured as 4.5 g of soot per liter of DPF substrate (Yang K., et al. 2016). The plenty amount of carbon soot embedded in the DPF provide a potential way to manufacture absorbents from it. And in recent years, researchers have applied carbon black as an adsorbent to remove heavy metals from aqueous solution (Wang X.S., et al. 2011; Zhou D.M., et al. 2010; Sappok A., et al. 2009). The adsorption capacity of commercial carbon black for Cd from water is over 250 mmol/kg and for Cu from water is 400mmol/kg (Zhou D.M., et al. 2010). The Cu, Pb, and Cd maximum adsorption capacity of wheat-residue derived carbon black is higher than 200mmol/kg (Qiu Y.P., et al. 2008). Therefore, it is highly desirable to identify alternative sources and alternative generation methods for high efficiency carbon black for heavy metal removal. Among these alternatives, DPF soot was appraised herein as compared to commercially available powdered activated carbon (PAC).

In this chapter, soot collected from a commercially used DPF was collected and appraised as a potential adsorbent. The heavy metal adsorption capacity for both DPF soot and PAC were evaluated by bench scale isotherm and kinetic tests. The target pollutants were selected as Cu(II), Cd(II) and Cr(VI). The overall objective of the study was to investigate the adsorption of three heavy metals Cd(II), Cu(II), and Cr(VI) onto DPF soot

www.manaraa.com

in a single and binary system. The first objective of the study determined the adsorption capacity of Cd(II), Cu(II), and Cr(VI) when comparing DPF soot to commercially available activated carbon. The second objective determined the adsorption mechanisms through surface characterization, EDS mapping, and FTIR.

6.2 Material and methods

6.2.1 Preparation of the adsorbents

Soot collected from a diesel particulate filter (DPF) was provided by Hunsicker Emission Services, LLC, whom specializes in DPF regeneration and cleaning. Hunsicker Emission Services, LLC provided soot which was used for the experiments herein. DPF soot as received contained impurities from lubricating oil additives and metallic ash particles. In order to prepare and purify the soot, 10 grams of soot was added to 100 mL of nitric acid (1 M). The slurry of soot and nitric acid was thermally treated under 80^{o}C for 24 hours to remove the diesel ash impurities from the soot. The soot and acid slurry was then passed through a 0.45 μm glass fiber filter and the soot retained on the filter paper was rinsed with distilled water several times until the solution pH reached 5.0. The soot was dried for 24 hours at 105^{o}C, then was sieved through a No. 200 U.S. Mesh sieve and soot was retained on No. 325 U.S. Mesh sieve, yielding a purified 200 x 325 DPF soot sample. The soot was rinsed on the No. 325 U.S. Mesh sieve and dried at 105^{o}C prior to use.

www.manaraa.com

Coconut shell based, unmodified, activated carbon was provide by Evoqua, LLC. The provided granular activated carbon was ground with a Breville coffee grinder (BCG800XL). The ground activated carbon was sieved through a No. 200 U.S. Mesh sieve and was retained on No. 325 U.S. Mesh sieve, yielding a 200 x 325 PAC sample. The PAC was rinsed by distilled water on the No. 325 U.S. Mesh sieve. The PAC was then dried at 105^{o}C prior to use.

6.2.2 Fourier transform infrared spectroscopy (FTIR)

Infrared spectra (IR) of the DPF soot and powder activated carbon (PAC) were analyzed using a Thermo-Scientific FTIR spectrometer with a deuterated triglycine sulfate detector frequency range of 500-4000 cm^{-1}. Samples were totally dried under oven at 105^{o}C and prepared as powder to use. Results spectra were compared to the standard FTIR peak table to determine the functional groups detected on the DPF soot and PAC surface.

6.2.3 Measurement of surface zeta potential

The surface zeta potential of DPF soot and PAC under a range of pH conditions were determined by a Malvern Zeta-Sizer. The suspensions were prepared by adding 0.05g of soot or PAC into 50 ml of deionized water and adjusting the pH to set-points in the range of 1.0 to 10.0. The isoelectric point (IEP) was then determined by plotting the line chart

www.manaraa.com

of pH versus zeta potential. The pKa value equals to the isoelectric point (IEP). The surface functional groups determined by finding out the pKa value of the soot and PAC.

6.2.4 Surface characterization of DPF soot and PAC by SEM-EDS

The soot and PAC particles before and after adsorption were dried in an oven for 24 hours at 105^{o}C. The surface microstructure of DPF soot and PAC particles before and after adsorption were analyzed by Scanning Electron Microscopy (SEM) with an accelerating voltage of 15keV. The elemental map of the DPF soot particles after adsorption of Cr(VI), Cu(II) and Cd(II) were analyzed by Electron Dispersive Spectroscope (EDS).

6.2.5 Synthetic wastewater preparation

Water solutions were prepared by dissolving analytical grade copper nitrate, Cadmium acetate and potassium dichromate in distilled water separately to obtain Cd(II), Cu(II) and Cr(VI) concentrations of 1000 mg/L. During the experiments, the stock solution was diluted to the desired concentration and the pH of the solution was adjusted to 4.5±0.5 by nitric acid and ammonia solution to prevent the precipitation of the target chemicals.

6.2.6 Batch experiments

Batch tests appraising the adsorption isotherms were performed by adding 0.1 gram of soot or PAC to 200 mL of prepared solutions to maintain metal concentrations from 20-200 mg/L. The mixtures were shaken in a thermostatic shaker (New Brunswick Scientific, Co.

www.manaraa.com

Inc.) with a stirring rate of 200 rpm and temperature maintained at 25°C. The samples were shaken for 24 hours, and then removed. The sample was filtered with a 0.45 μm glass fiber filter. The filtrate was analyzed for metal concentration with Atomic Absorption Spectrometry (AAS) (Perkin Elmer AAnalyst 200). In order to determine the effect of temperature and competitive adsorption, the same procedure as described was utilized, but temperature was adjusted from 25°C and 40°C, and dosage concentrations became binary instead of unary. The single compound tests were performed for the three different heavy metals, namely Cd(II), Cu(II) and Cr(VI) with concentrations from 20 mg/L to 200 mg/L at 25°C and 40°C. The binary tests were performed by adding Cr(VI) or Cu(II) to Cd(II) or Cr(VI),and Cd(II) to Cr(VI). The experiments were performed with both DPF soot and PAC. The detailed testing matrix is summarized in Table 6.1:

Table 6.1. summary of adsorption isotherms performed during the experiment

single system			binary system		
	25°C	40°C		25°C	
	20-200 mg/L			20-200 mg/L	20 mg/L
Cd(II)	√	√	Cd(II)/Cr(VI)	Cd(II)	Cr(VI)
Cr(VI)	√	√	Cr(VI)/Cu(II)	Cr(VI)	Cu(II)
Cu(II)	√	√	Cd(II)/Cu(II)	Cd(II)	Cu(II)

www.manaraa.com

In order to determine the influence of pH on Cd(II), Cr(VI) and Cu(II) adsorption, tests were performed at a pH of 2.0, 3.0 and 4.0. Specifically, 0.1 gram of adsorbent was added to 200 ml of solution with a metal concentration of 160 mg/L. The adsorption capacity (q_e) was compared with respect to pH.

The kinetic studies were carried out by preparing 1.0 L of target solution with a concentration of 100 mg/L of the desired heavy metal. At time zero, 0.5 grams of soot or PAC was added to the solution. The mixture was shaken at 25°C for 24 hours with a speed of 200 rpm. At predetermined time intervals 5mL samples of solution were withdrawn from the 1.0 L solution. The samples were then filtered with a 0.45 µm glass fiber filter and the metal concentration was analyzed by atomic absorption spectroscopy (AAS) (Perkin Elmer AAnalyst 200).

6.2.6.1 Adsorption isotherms

Several equilibrium models have been developed to describe adsorption isotherms. The Langmuir model and Freundlich model are the two most widely used models. The Langmuir isotherm is used to describe the saturated monolayer adsorption over a heterogeneous adsorbent surface and Freundlich isotherm is applied as an empirical, heterogeneous surface adsorption (Mohan D. M. 2002). Additionally, the Langmuir isotherm assumes the adsorption of each molecule onto the surface has the same activation

www.manaraa.com

energy while the Freundlich isotherm also suggests that adsorption energy decreases exponentially on completion of the adsorption centers of an adsorbent (Kyzas G.Z., et al. 2014). In addition to Freundlich and Langmuir, a monolayer model developed by Sellaoui L. (2017) was also applied during the analysis, it is theoretically based on how a receptor site can accept numerous metal ions which is different from the Langmuir model.

The amount of metal adsorbed by the adsorbents in the system was calculate by the mass balance equation 1:

$$q_e = \frac{V(C_0 - C_e)}{m} \quad (1)$$

The Langmuir model, Freundlich model, and monolayer model are described in equation 2, 3 and 4, respectively:

$$q_e = \frac{q_{max} b C_e}{1 + b C_e} \quad (2)$$

$$q_e = K_F C_e^{1/n} \quad (3)$$

$$q_e = \frac{Q_0}{1 + (\frac{C_{0.5}}{C_e})^n} \quad (4)$$

Where q_e (mg/g) represents the metal concentration retained on the adsorbents, C_0 and C_e are the initial and equilibrium metal concentrations. With regard to the monolayer model; Q_0 is the adsorbed quantity obtained at saturation and n is the number of ions per adsorption site. $C_{0.5}$ stands for the concentration at half saturation. V is the volume of the solution

www.manaraa.com

which is 200ml in the present study and m is the weight of the adsorbent, which is 0.1 gram herein.

6.2.6.2 Adsorption kinetics

Batch tests were performed to determine the kinetics of adsorption. Adsorption kinetics may be controlled by several theories: (1) bulk diffusion, (2) film diffusion, (3) chemisorption, and (4) intra-particle diffusion. (Kyzas G.Z., et al. 2014). Two commonly applied kinetic models include pseudo-first-order and pseudo-second-order; both were used to analyze the kinetic results herein. The pseudo-first-order model was applied when the initial solution concentration is very high and one adsorbate only occupied one binding site (Kyzas G.Z., et al. 2014; Azizian S. 2004). Additionally, pseudo-second-order model implies that one adsorbate species occupied two binding sites due to the chemisorption and when the initial solution concentration is not very high (Kyzas G.Z., et al. 2014; Azizian S. 2004). These kinetic rate equations can be written as follows:

$$\ln(q_e - q_t) = lnq_e - k_1 t \quad (5)$$

$$\frac{t}{q_t} = \frac{1}{k_2 q_e^2} + \frac{t}{q_e} \quad (6)$$

Where q_t (mg/g) is the amount of sorbate adsorbed at time t and q_e (mg/g) is the amount adsorbed at time of equilibrium. The k_1 (min) and k_2 (g/mg min) are the rate constants of the pseudo-first-order and pseudo-second-order equation, respectively.

www.manaraa.com

6.3.0 Results and Discussions

6.3.1 Fourier Transform Infrared Spectroscopy (FTIR) results

The FTIR spectra in Figure 6.1 depicts the DPF soot and PAC response. Compared with PAC, the DPF soot particles exhibits the same characteristic peaks. However, the peak position at 1730.09 cm^{-1} and 1516.62 cm^{-1}, which stands for C=O stretch in carboxylic acid, are sharper compared to PAC. The peaks at 3035.21 cm^{-1}, 2950.98 cm^{-1}, 2916.77 cm^{-1} represent hydroxyl stretch (-OH) which are very plentiful on the surface of both PAC and soot (Larkin P. 2011). The plentiful amount of hydroxyl and carboxyl functional groups could interact with the heavy metal cationic ions through electrostatic force. In addition, the soot surface maintains higher concentration of carboxylic functional groups than PAC as the peaks are sharper (Figure 6.1).

www.manaraa.com

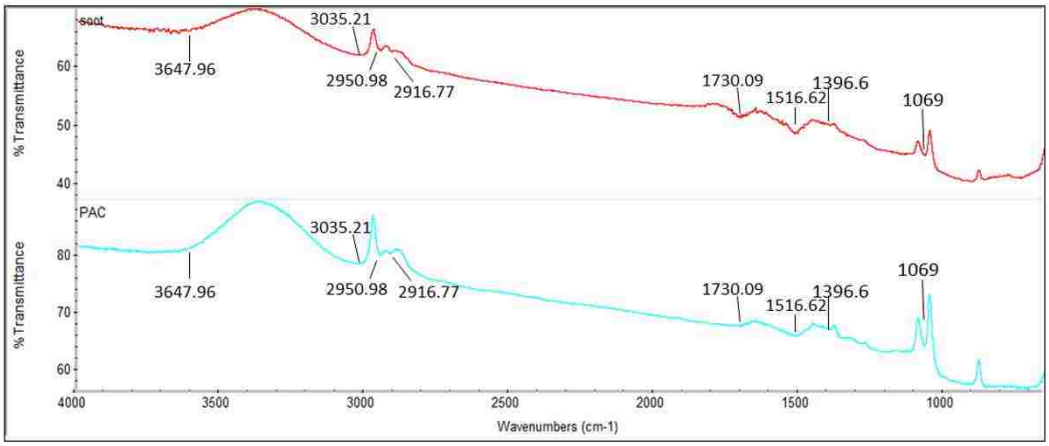

Figure 6.1. The Fourier transformed infrared spectra (FTIR) of DPF soot (top) and PAC (bottom).

6.3.2 Surface characterization of soot and PAC by SEM-EDS

The surface microstructure of DPF soot and PAC before and after the heavy metal adsorption was characterized by SEM and the surface elemental distribution was analyzed by EDS. The results are shown in Figures 6.2 to 6.6. When compared to PAC, which shows a very smooth surface with some pores evenly distributed throughout, the DPF soot particle surface shows a high degree of roughness as the single carbon black nucleus agglomerate together to form the relatively complicated structures (Figure 6.2). The higher surface roughness, provides support that the soot obtains larger external surface area and suggests that more adsorption sites are readily available.

www.manaraa.com

The EDS spectra of the DPF soot particle before adsorption demonstrated that the majority of the soot particle is composed of carbon (the highest peak) and oxygen, with trace levels of silicon (Figure 6.2). The trace level of silicon might be derived from additives used in lubricating oil in diesel engines (Sappok A., et al. 2009).

Figures 6.3 to 6.6 show the microstructure and elemental distribution of soot particles after adsorption of Cu(II), Cd(II) and Cr(VI) for both single and binary adsorbate systems. The green, red and yellow represent the concentration of Cd(II), Cr(VI) and Cu(II), respectively. For all three EDS figures, the soot surface demonstrates much higher Cu(II), Cd(II) and Cr(VI) concentrations compared to the background image. The metals adsorbed on the soot and PAC covered the adsorbent surface as shown in the EDS mapping (Figure 6.3-6.6). The EDS mapping of the binary adsorbate systems in Figure 6.5 and 6.6 show that the competitive adsorption for both soot and PAC lessens the intensity of the single adsorbate adsorption on the surface. Therefore, in the binary system, the existence of two heavy metals reduce the adsorption capacity of the competing heavy metal. The results of the binary system isotherms in Figure 6.11 confirmed the EDS mapping results and is in consistence with Sellaoui L. (2017) that suggests competitive adsorption reduces both Zn and Cd adsorption efficiency (Sellaoui L., et al. 2017).

www.manaraa.com

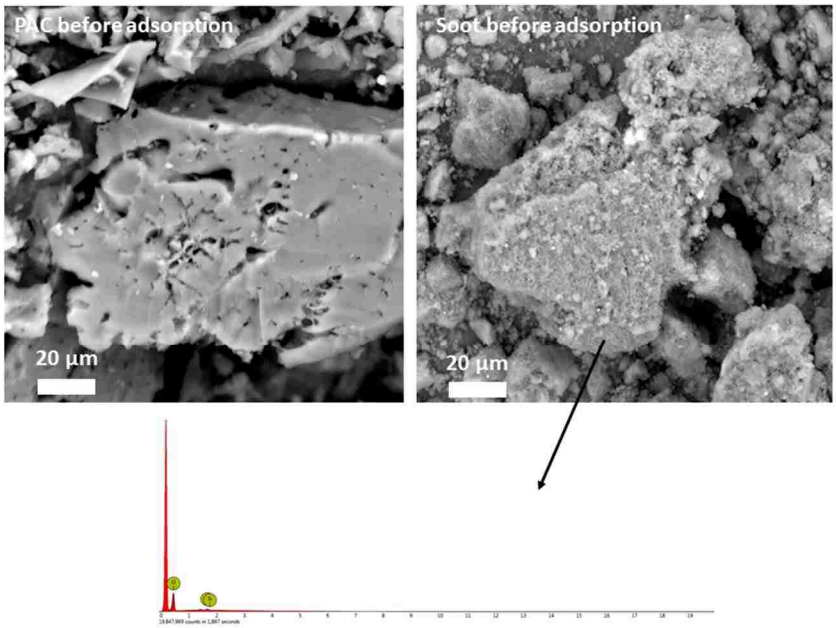

Figure 6.2. Surface microstructure of untreated coconut shell PAC before adsorption (left) and soot before adsorption (right), the bottom EDS mapping of soot.

www.manaraa.com

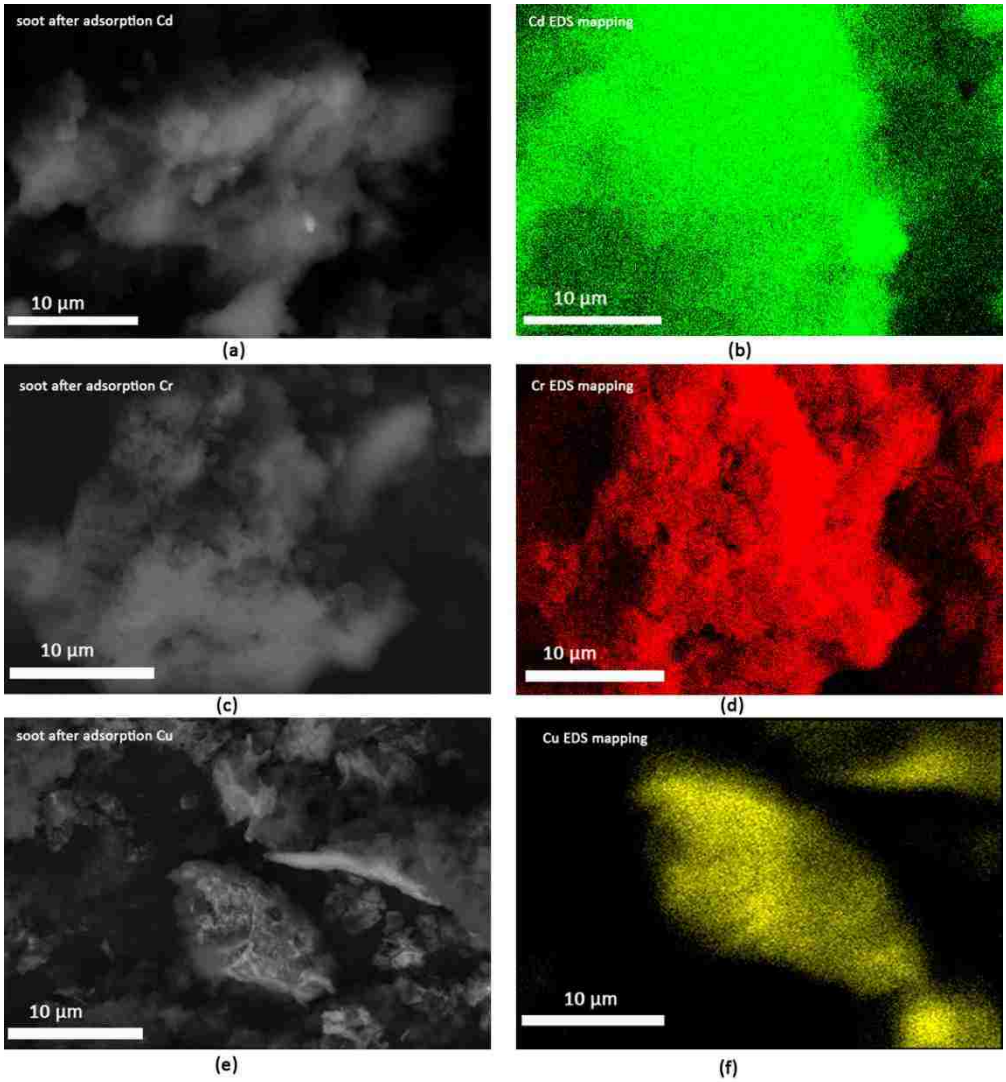

Figure 6.3. Elemental mapping of Cd(II), Cr(VI) and Cu(II) on soot (single system at 25°C): SEM soot (a, c, e), elemental mapping Cd (b), Cr (d), Cu (f).

www.manaraa.com

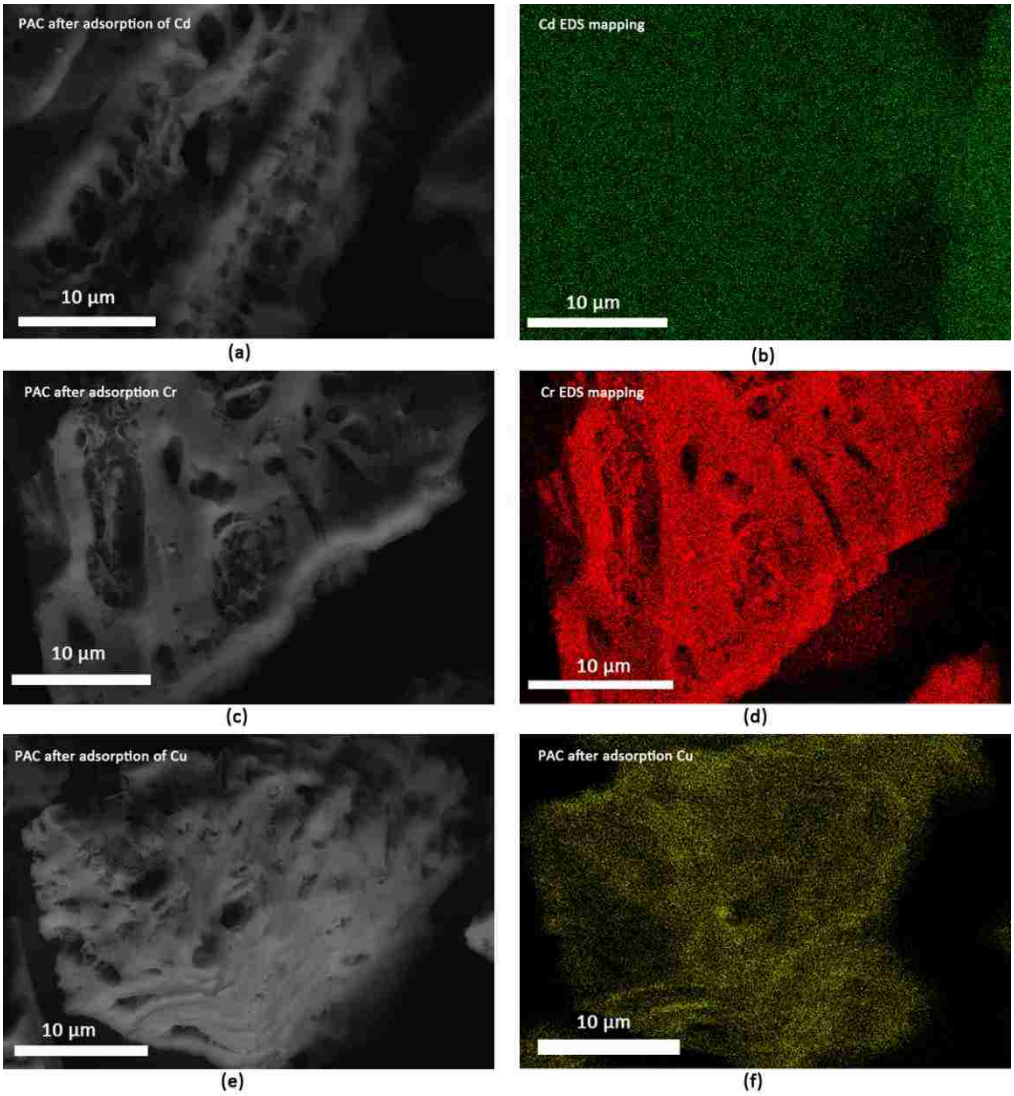

Figure 6.4. Elemental mapping of Cd(II), Cr(VI) and Cu(II) on PAC (single system at 25°C): SEM PAC (a, c, e), elemental mapping of Cd (b), Cr (d), and Cu (f).

www.manaraa.com

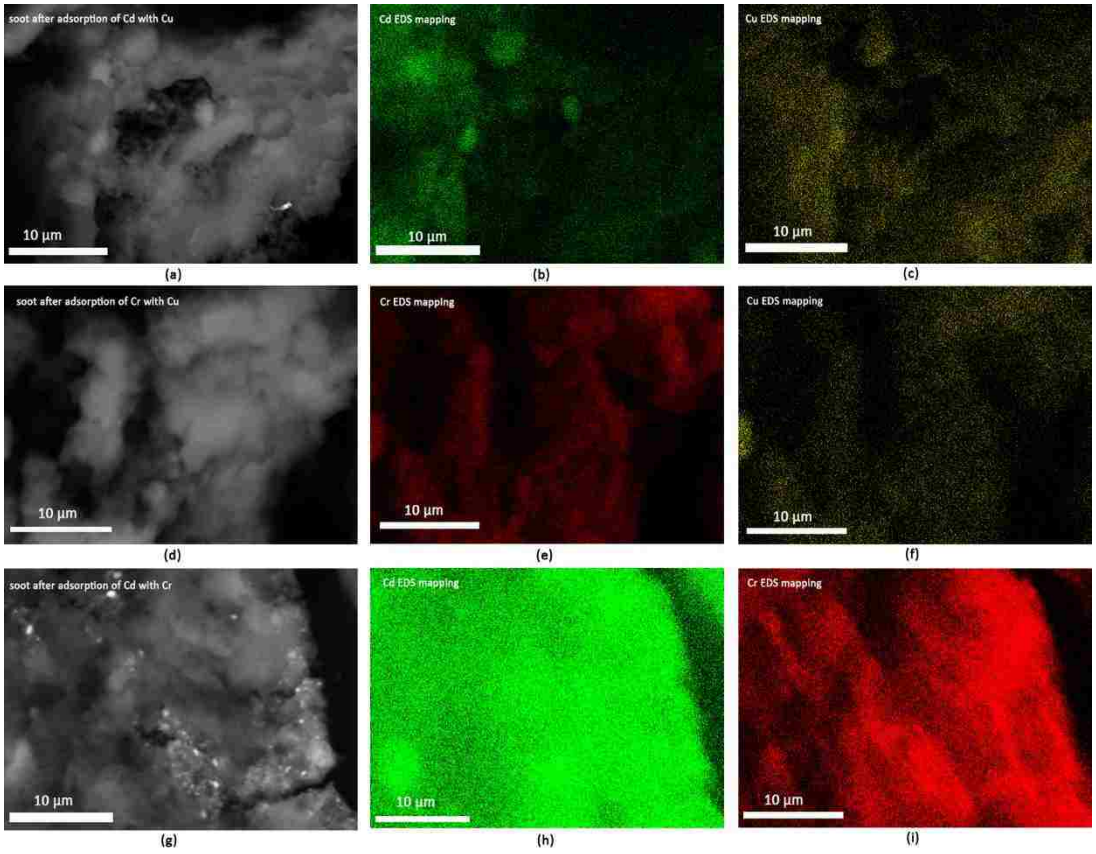

Figure 6.5. Elemental mapping of Cd(II)/Cu(II), Cr(VI)/Cu(II) and Cd(II)/Cr(VI) on soot (binary system at 25°C): SEM soot (a, d, g), elemental mapping of Cd (b, h), Cu (c ,f), Cr (e, i)

www.manaraa.com

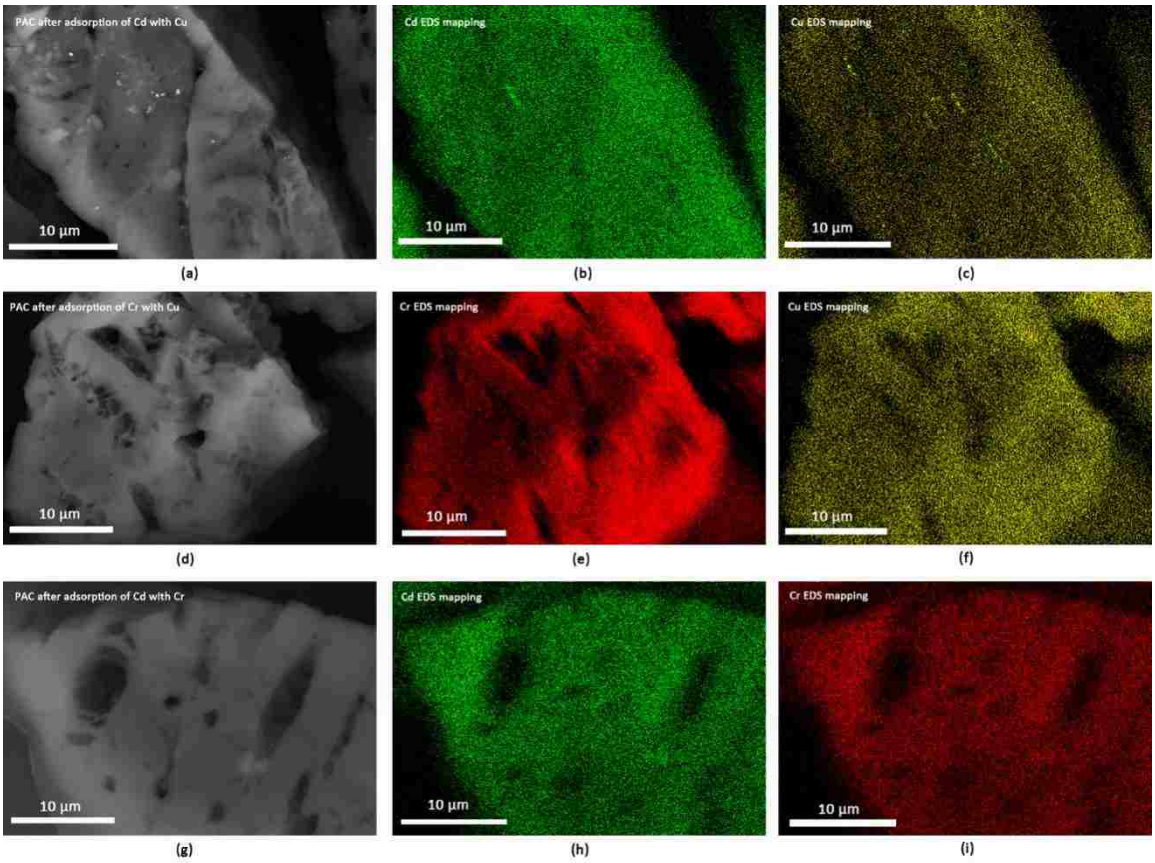

Figure 6.6. Elemental mapping of Cd(II)/Cu(II), Cr(VI)/Cu(II) and Cd(II)/Cr(VI) on PAC (binary system at 25°C): SEM PAC (a, d, g), elemental mapping of Cd (b, h), Cu (c ,f), Cr (e, i)

6.3.3 Surface zeta potential analysis

Figure 6.7 depicts the effect of pH on the zeta potential of DPF soot and PAC. The zeta potential of both adsorbents became more negative with increasing pH. The isoelectric point (IEP) is defined as the point when the positive zeta potential shifts to negative and is

www.manaraa.com

often used to characterize the electro-kinetic behavior of solid surfaces (Strelko V., et al. 2002). The IEP point can be used to determine the pKa value of surface functional groups. As shown in Figure 6.7, the IEP value is between 2 and 3, which corresponds to the pKa value of carboxylic acid. The IEP value for the DPF soot particle is lower, which indicates the degree of surface oxidation increases. Therefore, both the DPF soot and PAC surface shows ample carboxylic functional groups, as confirmed by the FTIR results. As the adsorption solution pH is in the range of 4 to 5, the carboxylic and hydroxyl functional groups loses one hydrogen ion so therefore exhibits a negative charge. The strong carboxylic surface groups are likely responsible for the steep fall in zeta potential (Strelko V., et al. 2002). According to the following mechanism shown in Figure 8, the negative charged carboxylic and hydroxyl functional groups have an extremely high affinity for Cd(II) and Cu(II). However, for chromate, the negatively charged functional groups will likely repel each other. Therefore, the chromate adsorption is more likely a result of physical adsorption or can be explained by redox reaction created by the interaction between DPF soot and Cr(VI) (Wang X.S., et al. 2010).

www.manaraa.com

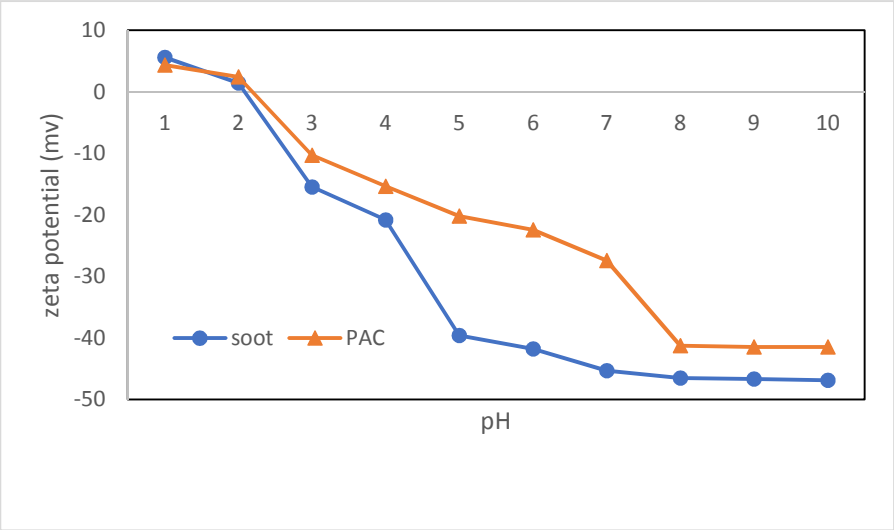

Figure 6.7. The surface zeta potential of DPF soot and PAC with variable pH.

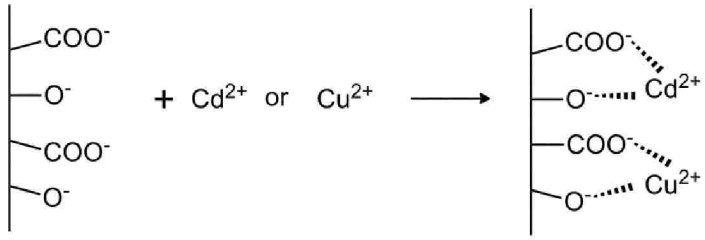

Figure 6.8. The adsorption mechanism of Cd(II) and Cu(II).

6.3.4 Adsorption Isotherms

6.3.4.1 Adsorption isotherm at 25°C

The adsorption isotherms of Cd(II), Cr(VI) and Cu(II) for soot and PAC at 25°C, are provided in Figure 6.9. The results indicate that both DPF soot and PAC have much higher affinity for Cr(VI), followed by Cd(II) and Cu(II). Compared with Cu(II) and Cd(II), the Cr(VI) adsorption behavior is more likely attributed to physical adsorption including Van Der Waals force. Work performed by Wang (2010) suggests that the Cr(VI) can be reduced

www.manaraa.com

to Cr(III) by the interaction between carboxylic or hydroxyl acid functional groups on carbon black and the Cr(III) with three positive charges has extremely high affinity for carbon black (Wang X.S., et al. 2010). Since the DPF soot possesses the same surface functional groups as PAC, the interaction between Cr(III) and DPF soot might also induce a similar mechanism. Considering the adsorption of Cd(II) and Cu(II), despite the Van Der Waals force, the electrostatic interaction between surface functional groups and cationic ions would facilitate the adsorption as indicated in Figure 6.8. In order to figure out the contribution of the electrostatic and non-electrostatic adsorption, adsorption capacity at 160±20 mg/L under elevated pH was presented in Table 6.2. The degree of dissociation of carboxylic and hydroxyl functional groups increases with increasing system pH, so that pH will impact the surface charge of soot and PAC particles (Zhou Q., et al. 2016). As the pH increased from 2.0 to 4.0, the adsorption capacity increased by almost half for both DPF soot and PAC. According to the zeta potential results, the pH increase from 2.0 to 4.0 results in a deprotonation of carboxylic and hydroxyl functional groups, further facilitating the electrostatic interaction.

The equilibrium adsorption data were modeled with Langmuir, Freundlich and monolayer isotherms, and the corresponding isotherm constants are in Table 6.3. It is readily apparent that both Langmuir and monolayer isotherm possesses a higher regression

www.manaraa.com

coefficient than the Freundlich isotherm for all the three metals tested herein. These results suggest that the adsorption occurs at discrete adsorption sites on the surface and the maximum adsorption occurs when the surface is covered by a monolayer of adsorbate (Amarasinghe B.M.W.P.K. 2007; Veli S. 2007). Furthermore, the monolayer model provides the best fit to the data compared with Langmuir model for all metals tested. The monolayer model was developed based on the Langmuir model but it assumes the single adsorption site can accommodate multiple ions, which is shown as n in the model (Sellaoui L. 2017). From Table 6.3, we observe that n(Cr)>n(Cu) and n(Cd), which means that both the DPF soot and PAC are more selective for Cr(VI) than Cu(II) and Cd(II). Therefore, the sorption of Cd(II), Cu(II) and Cr(VI) is most likely occurring at functional groups/binding sites on the surface of the DPF soot and PAC. Therefore, the monolayer model offers better modeling of the adsorption mechanism (Sari A. 2009, Sellaoui L. 2017).

When comparing the ultimate loading of the results in Table 6.6 for both DPF soot and PAC, it is apparent that the DPF soot possesses higher capacity for Cr (IV) than PAC. Specifically, the DPF soot adsorbed 105 mg Cr (IV) per gram of DPF soot, compared to the 42 mg Cr (IV) per gram of PAC. The ultimate loading for Cd (II) is similar for both

www.manaraa.com

DPF soot and PAC. The ultimate loading for Cu (II) is the lowest of all metals tested herein, but is nearly double for DPF soot than that of PAC.

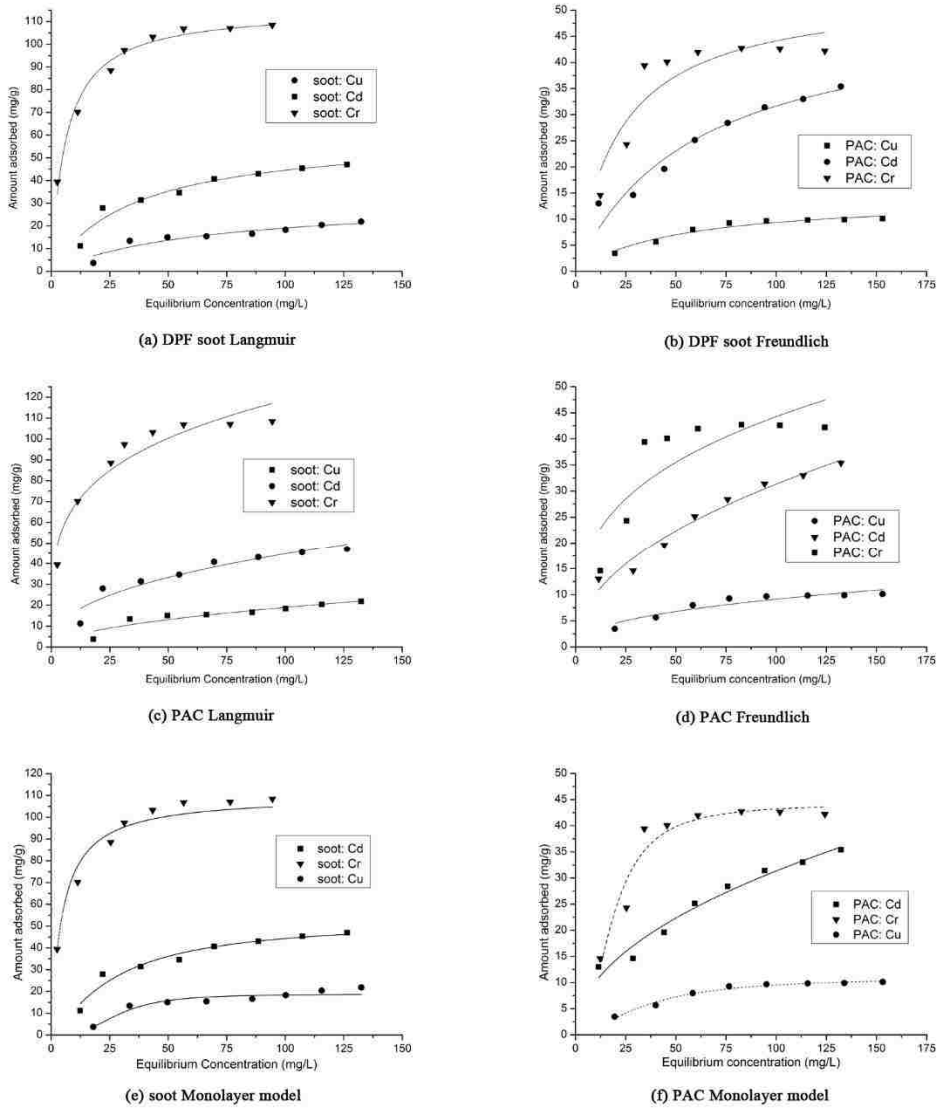

Figure 6.9. Adsorption isotherms of Cd, Cr and Cu at 25°C: a, DPF soot Langmuir; b, DPF soot Freundlich; c, PAC Langmuir; d, PAC Freundlich; e, DPF soot monolayer model; f, PAC monolayer model

www.manaraa.com

Table 6.2. Cd(II), Cu(II) adsorption capacity (mg/g) under variable pH at 25°C corresponding to initial concentration of 160±20 mg/L

DPF soot			PAC		
pH	**Cd**	**Cu**	**pH**	**Cd**	**Cu**
2	22.4	12.1	2	12.4	5.9
3	35.2	13	3	15.7	10.1
4	51.1	25	4	33.1	13

Table 6.3. Cd(II), Cu(II), Cr(VI) 25°C isotherm parameters

	Langmuir			Freundlich			monolayer model			
soot	**q**	**b**	**R^2**	**k**	**n**	**R^2**	**Q_0**	**n**	**$C_{0.5}$**	**R^2**
Cd	86.95	0.0132	0.913	3.92	1.8597	0.857	52.93	2.256	27.2	0.98
Cr	109.89	0.2106	0.987	32.9	3.4722	0.944	126.4	3	7.634	0.987
Cu	82.43	0.0002	0.873	1.5	1.364	0.794	22	2.77	33.524	0.99
PAC	**q**	**b**	**R^2**	**k**	**n**	**R^2**	**Q_0**	**n**	**$C_{0.5}$**	**R^2**
Cd	32.89	0.051	0.942	3.78	2.1939	0.911	36.8	1.888	21.3	0.945
Cr	69.44	0.0225	0.941	6.11	2.2614	0.767	64.25	2.19	18.46	0.92
Cu	16.42	0.0137	0.986	0.81	1.8903	0.916	16.7	1.86	34.256	0.98

6.3.4.2 Effect of adsorption temperature

www.manaraa.com

The effect of temperature on the adsorption capacity was studied at 25°C and 40°C, and the results are presented in Figure 6.10 and Table 6.5. The adsorption capacity decreased as the temperature increased from 25°C to 40°C for all three metals. As previously reported, the Langmuir isotherm provides the best fit for both 25°C and 40°C, which means that the temperature change does not alter the adsorption mechanism and adsorption sites on the DPF soot and PAC (Table 6.5). In order to confirm the results that the adsorption process is an exothermic reaction, the Gibbs' free energy (ΔG) and enthalphy (ΔH) were calculated using equations 7 and 8:

$$\Delta G^0 = -RTln(K_1) \quad (7)$$

$$\Delta H^0 = -R\left(\frac{T_2T_1}{T_2-T_1}\right)\ln(\frac{K_2}{K_1}) \quad (8)$$

Where K_1, K_2 are the Langmuir constants, b, from Table 6.3 multiplied by 1000, corresponding to the b values at both 25°C and 40°C.

The calculated thermodynamic parameters for DPF soot and PAC are presented in Table 6.4. The Gibbs' Free Energy for all three metals are negative which confirms the feasibility and spontaneous nature of the adsorption (Mohan D. 2002). Further, the negative values of enthalphy (H) indicate the exothermic nature of the adsorption process for both DPF soot and PAC. Therefore, adsorption of Cd(II), Cu(II) and Cr(VI) will be inhibited by increased temperatures. This was confirmed by Sari A. (2009), who demonstrated the same

www.manaraa.com

phenomena for the inhibition of adsorption with increased temperatures for Cd(II) and Pb(II) onto biomass (Sari A. 2009).

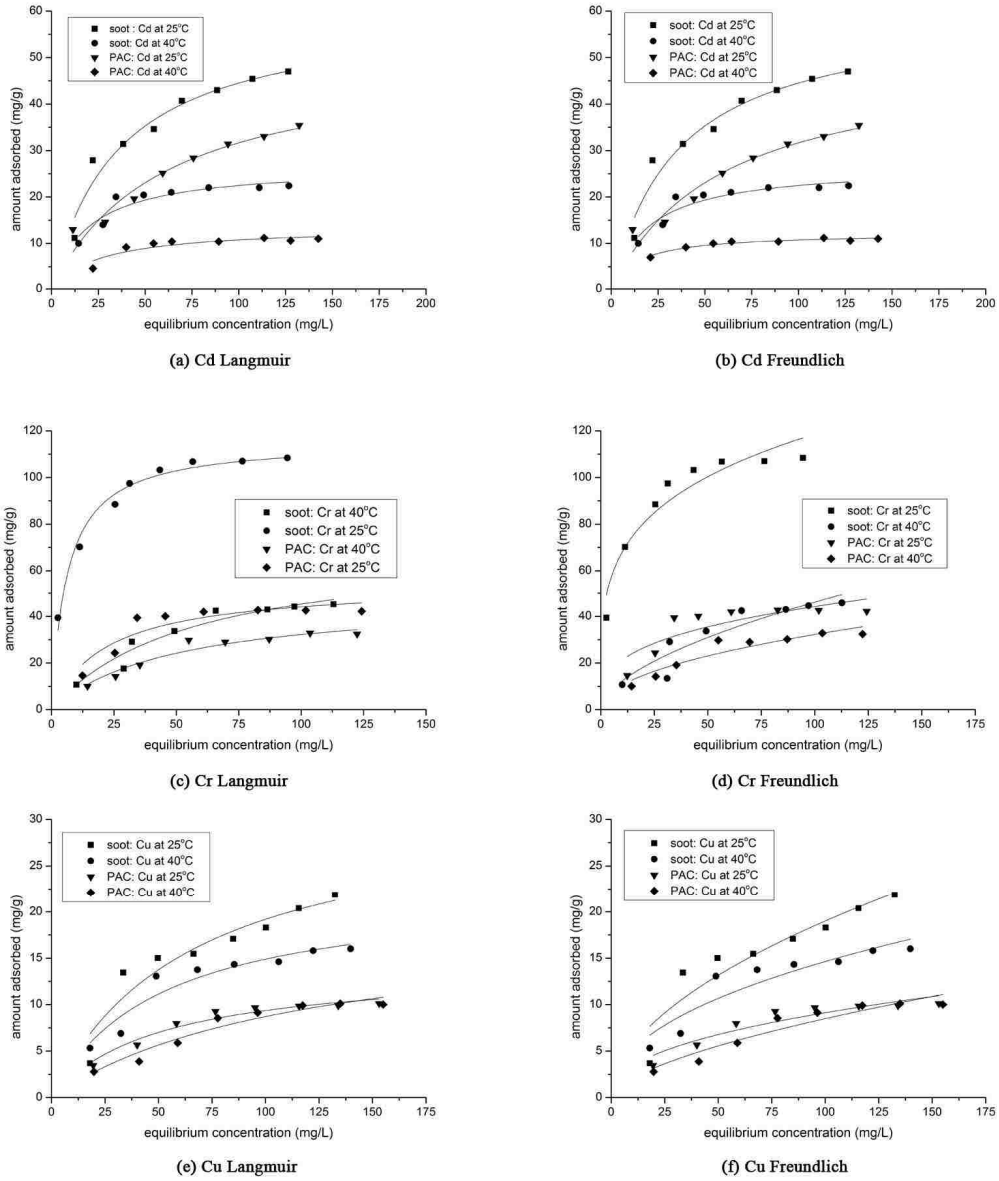

Figure 6.10. Effect of temperature on the adsorption isotherms of Cd(II), Cr(VI) and Cu(II): a, Cd Langmuir; b, Cd Freundlich; c, Cr Langmuir; d, Cr Freundlich; e, Cu Langmuir; f, Cu Freundlich.

www.manaraa.com

Table 6.4. Thermodynamic parameters for the adsorption of Cd(II), Cu(II) and Cr(VI) on DPF soot and PAC

soot	ΔG(KJ/mol)		ΔH(kJ/mol)	PAC	ΔG(KJ/mol)		ΔH(kJ/mol)
	25°C	40°C			25°C	40°C	
Cd(II)	-6.4	-9.33	-52.01	Cd(II)	-9.54	-10.78	-10.92
Cu(II)	3.98	-3.6	-156.15	Cu(II)	-5.24	-5.6	-3.43
Cr(VI)	-13.25	-7.9	-2.41	Cr(VI)	-7.71	-7.15	-2.29

Table 6.5. Langmuir and Freundlich isotherm constants for Cd(II), Cu(II), Cr(VI) adsorption at 40°C

	Langmuir			Freundlich		
Soot	q	b	R2	k	n	R2
Cd	29.76	0.0361	0.936	4.67	2.8802	0.794
Cr	58.82	0.0210	0.872	2.27	1.5221	0.842
Cu	51.28	0.0041	0.979	0.41	1.2822	0.891
PAC	q	b	R2	k	n	R2
Cd	12.50	0.0630	0.967	3.99	4.6838	0.846
Cr	53.76	0.0156	0.981	2.32	1.7271	0.932
Cu	18.15	0.0086	0.949	0.340	1.4314	0.946

6.3.4.3 Binary adsorption isotherms

www.manaraa.com

Adsorption in multi-component systems is more complicated than single compound systems due to competitive adsorption. The adsorption isotherms of binary contaminant systems of Cd(II)/Cr(VI), Cr(VI)/Cu(II), Cd(II)/Cu(II) are presented in Figure 6.11. The adsorption isotherms were obtained at 25°C. For each binary system, 20 mg/L of Cr(VI) or Cu(II) was added to each solution ranging from 20-200 mg/L of Cd(II) or Cr(VI). For both DPF soot and PAC, the presence of 20 mg/L Cr(VI) or Cu(II) in the solution adversely affects the adsorption of Cd(II) and Cr(VI).

As reported in Table 6.6, the binary adsorption results are adequately fit by both Langmuir and Freundlich Models. For Cd(II)/Cr(VI) and Cr(VI)/Cu(II), the Langmuir model fit the result slightly better than Freundlich model as shown in Table 6.6. According to Table 6.7, the ultimate loadings for the single compound system is lower for Cd(II) and Cr(VI) compared to binary system, specifically, the Cd(II) adsorption capacity reduced by almost half. And this data was slightly lower for Cr (VI), which means Cu(II) has weaker impaction on Cr(VI).

www.manaraa.com

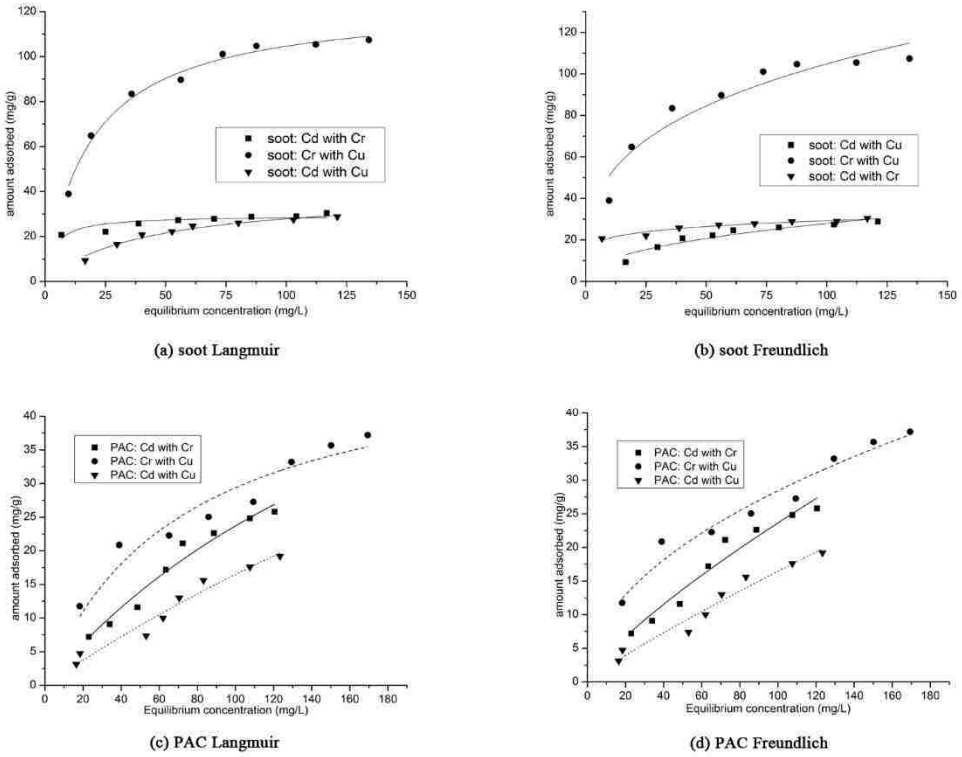

Figure 6.11. Binary adsorption of Cd(II), Cr(VI) at 25°C: a, soot Langmuir; b, soot Freundlich; c, PAC Langmuir; d, PAC Freundlich.

www.manaraa.com

Table 6.6. Langmuir and Freundlich isotherm constants for binary adsorption at 25°C

	Langmuir			freundlich		
soot	**q**	**b**	**R^2**	**k**	**n**	**R^2**
Cd, Cr	51.02	0.0141	0.972	2.51	1.8786	0.903
Cr,Cu	88.91	0.0206	0.999	19.86	2.7285	0.918
Cd,Cu	28.65	0.3431	0.737	15.22	7.0921	0.931
PAC	**q**	**b**	**R^2**	**k**	**n**	**R^2**
Cd, Cr	54.05	0.006	0.907	0.56	1.243	0.900
Cr,Cu	48.70	0.0186	0.939	2.07	2.0631	0.927
Cd,Cu	32.05	0.0075	0.906	0.35	1.2310	0.922

Table 6.7. Ultimate loading of single and binary system under 25°C.

soot	**ultimate loading (mg/g)**	**soot**	**ultimate loading (mg/g)**
Cd	47.0	Cd/Cr	28.8
Cr	108.0	Cr/Cu	107.4
-	-	Cd/Cu	30.4
PAC	**ultimate loading (mg/g)**	**PAC**	**ultimate loading (mg/g)**
Cd	35.4	Cd/Cr	25.8
Cr	42.2	Cr/Cu	37.2
-	-	Cd/Cu	19.2

www.manaraa.com

6.3.5 Adsorption Kinetics

In order to understand the controlling mechanisms of the adsorption process such as mass transfer or chemical reactions, two kinetic models were tested, which were pseudo-first-order and pseudo-second-order. Based on the results presented in Figure 6.12, the adsorption kinetics of Cd(II), Cu(II) and Cr(VI) is best modeled by pseudo-second-order. The regression coefficients for all metals tested herein support pseudo-second-order, as presented in Table 6.8. The pseudo-second-order model assumes that the initial adsorption rate is rapid followed by a slower adsorption rate, due to chemisorption mechanisms (Wang X.S., et al. 2011). Therefore, during the beginning of adsorption, the adsorption sites are open and metal ions interact rapidly with adsorbents due to high diffusion rates of metal ions attributed to the much higher concentration gradient between bulk solution and adsorbent surface. However, the adsorption rate decreases sharply as diffusion slows due to lower concentration gradients across the adsorbent surface area (Amarasinghe B.M.W.P.K. 2007).

www.manaraa.com

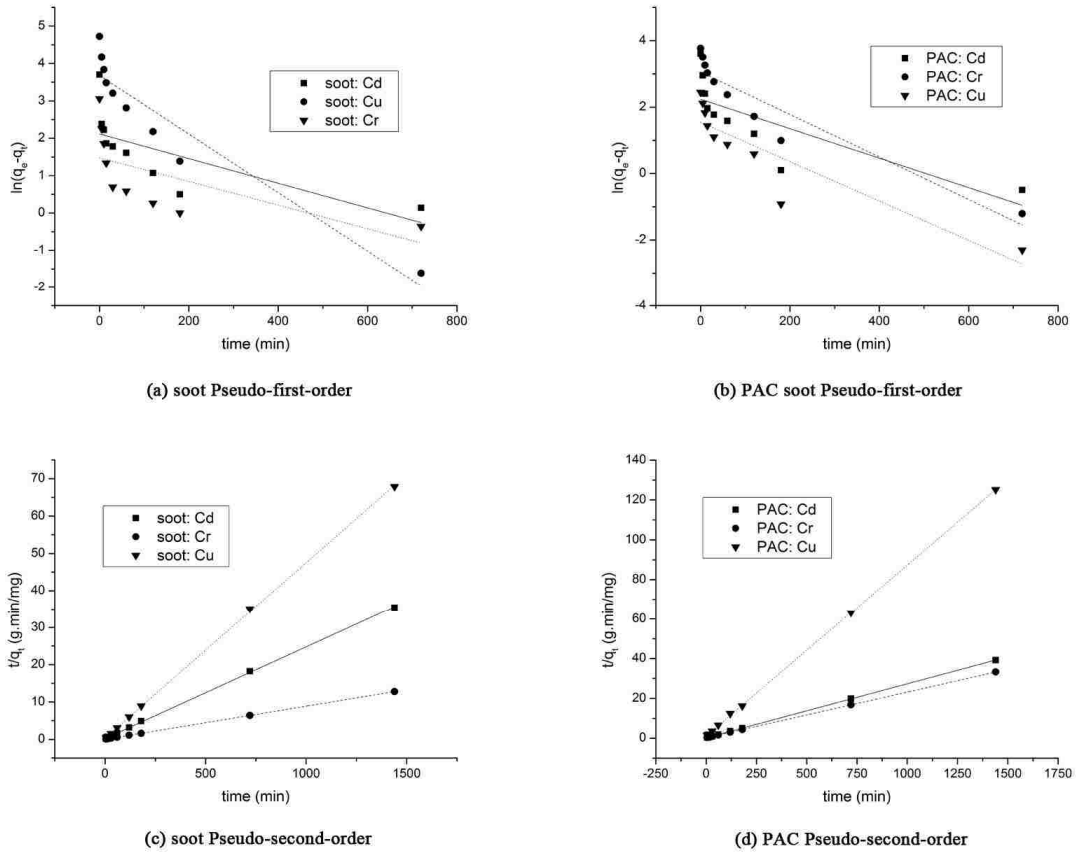

Figure 6.12. Adsorption Kinetics at 25°C: a and b corresponding to pseudo-first-order model; c and d corresponding to pseudo-second-order model.

www.manaraa.com

Table 6.8. kinetic constants for adsorption of Cd(II), Cu(II) and Cr(VI)

	Soot				PAC			
	Pseudo-first-order		Pseudo-Second-order		Pseudo-first-order		Pseudo-Second-order	
	K_1	R^2	K_2	R^2	K_1	R^2	K_2	R^2
Cd(II)	0.0032	0.5627	0.004	0.998	0.0044	0.625	0.004	0.999
Cr(VI)	0.0078	0.9010	0.001	1.000	0.0064	0.888	0.001	1.000
Cu(II)	0.0032	0.4160	0.007	0.999	0.0059	0.805	0.005	0.999

6.4 Conclusion

Porous carbon-based soot samples were recovered from a DPF and were utilized as an adsorbent in the present study. The equilibrium sorption of three metal ions, Cd(II), Cu(II) and Cr(VI) were appraised for both DPF soot and PAC. Herein, the authors appraised all three metals as single compound systems and as binary systems. The adsorption performance was appraised at both 25°C and 40°C. The surface microstructures of the DPF soot and PAC was characterized by SEM-EDS. The surface functional groups of both adsorbents were appraised by FTIR. The surface zeta potential of the carbon soot was studied to determine the isoelectric point.

www.manaraa.com

Compared with activated carbon, DPF soot appears to possess more surface roughness and surface area as observed during SEM analysis. The EDS spectra revealed that the DPF soot possesses a similar chemical composition with commercial activated carbon. The FTIR results indicate that both the DPF soot and PAC are dominated by hydroxyl and carboxylic functional groups. Interestingly, the surface density of these functional groups appears higher for soot. Herein, both adsorbents possess a high surface acidity and low isoelectric point.

Results indicate that the adsorption of heavy metals by DPF soot and PAC occur through both electrostatic interaction and physical adsorption. The Gibb's free energies of adsorption were calculated to confirm the adsorption is exothermic and spontaneous for all three metals. The isotherm results for both single and binary systems were best fit by the monolayer model and Langmuir isotherm. The kinetic study demonstrated that pseudo-second-order kinetic model best fits all three metal ions.

In sum, DPF soot is a viable adsorbent for the elimination of heavy metal pollution from aqueous systems. DPF soot could be a very low-cost adsorbent applied in this capacity; however adoption requires overcoming the technical challenges of efficient recovery and purification.

Acknowledgements

www.manaraa.com

The authors would like to thank Hunsicker Emission Service, LLC for providing the DPF soot for this work, which was recovered from a commercial vehicle's diesel particulate filter (DPF).

6.5 References

Amarasinghe B.M.W.P.K., Williams R.A. (2007) Tea waste as a low cost adsorbent for the removal of Cu and Pb from wastewater. Chemical Engineering Journal 132: 299-309.

Azizian S. (2004) Kinetic models of sorption: a theoretical analysis. Journal of colloid and interface science 276: 47-52.

Cho D.W., Chon C.M., Kim Y.J., Jeon B.H., Schwartz F.W. (2011) Adsorption of nitrate and Cr(VI) by cationic polymer modified granular activated carbon. Chemical Engineering Journal 175: 298-305.

Cheung C.W., Porter J.F., Mckay G. (2000) Elovich equation and modified second order equation for sorption of cadmium ions onto bone char. Journal of Chemical technology and biotechnology 75: 963-970.

Hamilton R.S., Mansfield T.A. (1991) Airborne particulate elemental carbon: its sources, transport and contribution to dark smoke and soiling. Atmospheric Environment 25A: 715-723.

Jiang M.Q., Jin X.Y., Lu X.Q., Chen Z.L. (2010) Adsorption of Pb(II), Cd(II), Ni(II) and Cu(II) onto natural kaolinite clay. Desalination 252: 33-39.

www.manaraa.com

Kyzas G.Z., Deliyanni E.A., Matis K.A. (2014) Graphene oxide and its application as an adsorbent for wastewater treatment. Journal of Chemical technology and biotechnology 89: 196-205.

Mellah A., Chegrouche S. (1997) The removal of zinc from aqueous solution by natural bentonite. Water research 31: 621-629.

Mahvi A.H., Naghipour D., Vaezi F., Nazmara S. (2005) Teawaste as an adsorbent for heavy metal removal from industrial wastewaters. American journal of applied sciences 2(1): 372-375.

Mohan D., Singh K.P. (2002) single and multi-component adsorption of cadmium and zinc using activated carbon derived from bagasse an agricultural waste. Water research 36: 2304-2318.

Okieimen F.E., Okundia E.U., Ogbeifun D.E. (1991) Sorption of cadmium and lead ions on modified groundnut (Arachis hypogea) husks. Journal of Chemical technology and biotechnology 51: 97-103.

Qiu Y.P., Cheng H.Y., Xu C., Sheng G.D. (2008) Surface characteristics of crop residue derived black carbon and lead(II) adsorption. Water Research, 42: 567-574.

Rao R.A.K., Kashifuddin M. (2016) Adsorption studies of Cd(II) on ball clay: comparison with other natural clays. Arabian journal of chemistry 9: 1233-1241.

Street D.G., Gupta S., Waldhoff S.T., Wang M.Q., Bond T.C., Bo Y.J. (2001) Black carbon emissions in China. Atmospheric Environment 35: 4281-4296.

www.manaraa.com

Strelko V., Malik D.J., Streat M. (2002) Characterization of the surface of oxidized carbon adsorbents. Carbon 40: 95-104.

Sappok A., Santiago M., Vianna T., Wong V. (2009) Characteristics and effects of ash accumulation on diesel particulate filter performance: rapidly aged and field aged results. SAE International Paper No.:2009-01-1086.

Srivastava S.K., Tyagi R., Pant N., Pal N. (1989) Studies on the removal of some toxic metal ions. Part II Removal of lead and cadmium by montmorillonite and kaolinite. Environmental Technology Letters 10: 275-282.

Sari A., Tuzen M. (2009) Kinetic and equilibrium studies of biosorption of Pb(II) and Cd(II) from aqueous solution by macrofungus (Amanita rubescens) biomass. Journal of Hazardous materials 164: 1004-1011.

Sari A., Tuzen M., Uluozlu O.D., Soylak M. (2007) biosorption of Pb(II) and Ni(II) from aqueous solution by lichen (Cladonia furcata) biomass. Biochemical Engineering Journal 37: 151-158.

Sellaoui L., Dotto G.L., Lamine A.B., Erto A. (2017) Interpretation of single and competitive adsorption of cadmium and zinc on activated carbon using monolayer and exclusive extended monolayer models. Environmental Science and Pollution Research 24: 19902-19908.

United States Environmental Protection Agency (USEPA) (2009) National primary drinking water regulations.

www.manaraa.com

Veli S., Alyuz B. (2007) Adsorption of copper and zinc from aqueous solutions by using natural clay. Journal of hazardous materials 149: 226-233.

Viidanoja J., Sillanpaa M., Laakia J., Kerminen V.M., Hillamo R., Aarnio P., Koskentalo T. (2002) Organic and black carbon in PM2.5 and PM10: 1 year of data from an urban site in Helsinki, Finland. Atmospheric Environment 36: 3183-3193.

Wang X.S., Chen L.F., Li F.Y., Chen K.L., Wan W.Y., Tang Y.J. (2010) Removal of Cr(VI) with wheat residue derived black carbon: reaction mechanism and adsorption performance. Journal of hazardous materials 175: 816-822.

Wang X.S., Miao H.H., He W., Shen H.L. (2011) Competitive adsorption of Pb(II), Cu(II), and Cd(II) ions on wheat residue derived black carbon. Journal of chemical and engineering data 56: 444-449.

Yang K., Fox J.T., Hunsicker R. (2016) Characterizing diesel particulate filter failure during commercial fleet use due to pinholes, melting, cracking and fouling. Emission Control Science and Technology 2(3): 145-155.

Zhou Q., Liu Z.D., Liu Y., Jiang J., Xu R.K. (2016) Relative abundance of chemical forms of Cu(II) and Cd(II) on soybean roots as influenced by pH, cations and organic acids. Scientific Reports 6(36373): 1-9.

Zhou D.M., Wang Y.J., Wang H.W., Wang S.Q., Cheng J.M. (2010) surface modified nanoscale carbon black used as sorbents for Cu(II) and Cd(II). Journal of hazardous materials 174: 34-39.

www.manaraa.com

Chapter 7

Conclusions：Understanding DPF failure, Improving DPF maintenance technologies, and advancing particulate filter materials

7.1 conclusions

Premature failures including melting, pinholes and cracking are observed frequently during the commercial application of Diesel Particulate Filter (DPF) for both cordierite and silicon carbide substrate. Further, traditional DPF regeneration and reclamation process has major disadvantage via accelerating the premature failures. One scientific mechanism was revealed and two engineering solutions were proposed and tested to prolong the DPF life-cycle, increasing the DPF filtration efficiency.

Firstly, fundamentally revealed the underlying mechanisms that lead to DPF premature failures by understanding the thermal, chemical conditions that cause the failures. Then developing water based DPF reclamation process that can have higher DPF soot and ash removal efficiency, release backpressure and prolong the DPF substrate lifetime. Finally, manufacturing the silicon carbide nanowire matrices (SCNWs) which has higher porosity, surface area and higher mechanical strength. The SCNWs can be potential

www.manaraa.com

substitution material for DPF. Results from this research also made many new original contributions to science and engineering as listed in the following section.

Original contributions to science and engineering:

1. **Classification of the DPF premature failure as pinhole, melting, cracking failure.** Results by analyzing the element distribution around the pinhole, melting and cracking area from commercial exhausted DPF indicated several kinds of ash components, specifically, S, P, Zn and K tend to penetrate deep inside the cordierite substrate instead of staying on the 20nm deep surface, which was confirmed from SEM-EDS and XPS.
2. **The DPF ash components have significantly affection on the cordierite substrate, especially during the passive and active regeneration, which leads to the premature failures. Despite the relative concentrations, Na and K are the leading contaminants that react with cordierite started at temperature around 500ºC.** The reactions altered the crystalline phases, leading to the melting of the substrate. The grain boundaries formed during the reaction further result in cracking failures.
3. **K and Zn have the similar corrosion pathway by first spreading on the cross section of the substrate, followed by react with it.** It was confirmed that Zn and

www.manaraa.com

K can penetrate inside the cordierite substrate at faster rate compared with other chemicals. However, the Na and Fe tend to first attach to the surface, and penetrate inside by reacting with it. Despite the highest concentration of calcium, it was not the leading contaminant because the reaction need higher temperature and longer time.

4. **Water-based DPF reclamation process can remove both DPF soot and ash at the same time.** A water based chemical including self-assembled surfactant, solvents and organic acid can remove more than 80% of the DPF soot and ash than traditional pneumatic air method. The wash process was carried out under room temperature which avoid the corrosion effect of DPF metallic ash.

5. **The chemical formulation of the water-based wash recipe can protect the catalyst Pt/Pd which coated on the DOC and SCR.** Compared with other washing process developed by Corning, Cummins, the wash processes we used herein can selectively remove the ash components with less affection on the catalyst coated.

6. **Backpressure cannot reflect the cleaning condition of the DPF.** The full-scale demonstration of the wash process indicated that although the wash process can remove four times higher of the DPF soot and ash, the back pressure was not

www.manaraa.com

reduced at the same rate. Therefore, other characterizing method is needed to substitute the widely used backpressure method.

7. **Guar gum can act both precursor material and binder material at the same time.** Guar gum has large saccharine molecules that cross-linked together which can encapsulate the silicon particle. Guar gum react with water to form gelation structure which is easy to shape based on the requirement. Compared to zero valent carbon source, for example, anthracite fine could not form tremendous of silicon carbide nanowires.

8. **Iron act as catalyst to foster the in-situ growth of Silicon carbide nanowire from the SiC ceramic.** At high temperature, the melted iron particle can dissolve the silicon and carbon monoxide vapor, leading the grow of the SCNW, results in a cotton-like structure. This was confirmed by SEM-EDS which show the SCNW tip has spherical structure with 30% of iron. XRD indicated the intermediate crystalline phase is FeSi, which corresponding to the iron catalysis mechanism. The resulted ceramic wafer has very strong mechanical property of 325 HV/kg compared to cordierite, which has 200 HV/kg.

9. **The resulted SCNWs first occurred at temperature as low as 1100ºC, resulted SCNW has core/shell structure.** SEM-EDS and XRD confirmed the SCNWs first

www.manaraa.com

occurred at temperature around 1100°C, and optimized temperature around 1400°C. The SCNW followed the growing direction of [112]. The resulted ceramic wafer is highly porous with SCNW grow on it.

The impacts on sustainability beyond the DPF industry

Although the engineering solutions presented in this thesis focused mainly on addressing the sustainability issues in the diesel after treatment system, these approaches also benefit the society and other industries in the following areas:

1. by reclaiming the DPF soot from the DPF regeneration and reuse it as porous carbon adsorbent, the usage of commercial activated carbon can be reduced. Results indicated the DPF soot has higher surface area, plenty of functional groups which facilitate the adsorption of Cd(II), Cr(VI) and Cu(II).
2. By replacing these expensive precursor materials, the use of organic precursor guar gum provides more revenue by reducing the material cost.

7.2 recommendation for future studies

In the current thesis, the author has already revealed the underlying mechanism that leads to the DPF substrate material premature failures. And a water based wash process has also been developed. However, there are some questions remain to be solved which should be focused on during the future researches.

www.manaraa.com

1. the water based wash process generate tons of industrial wastewater that contains high concentration of heavy metals, COD, and suspended solid that need to be treated.
2. The manufactured porous SiC ceramics has random number of porosity. So future researches are needed to control the pore size and porosity of the substrate. The author has some preliminary data which shows control the pH and temperature in the precursor materials during curing process can control the pore size of the ceramics. But further researches are needed to advance this technology.
3. Some preliminary data indicated the particle size of the guar gum, silicon powder can greatly impact on the growth of silicon carbide nanowires through reducing the melting point of the precursor materials. Therefore, further researches are needed to optimize the SCNW growth.
4. The underlying mechanism of iron catalyzing growth of SCNW is still remaining to be unsolved, especially the chemical bonding situation during the catalysis reaction. Therefore, in-situ analysis the chemical formulation in the growing tip by Raman, IR or other method are needed.

www.manaraa.com

5. Since the SCNW has large surface area and high porosity, it is promising to coat the SCNW matrices with certain kinds of catalyst that can be used in water treatment or VOC reduction.

www.manaraa.com

Kun Yang

Bethlehem, Pennsylvania 18015 • 484.557.8641 • kuy313@lehigh.edu

Environmental Engineering

Recent graduated with a doctorate in Environmental Engineering and experience researching and developing technology aimed at having a positive impact on the environment. Consulting experience on a major development effort funded by government grants. Recognized leader, capable of guiding teams and operations to ensure optimal processes. Adept at designing various technologies and completing research to understand mechanisms.

Areas of Expertise

- Drainage system design
- TCLP test
- Groundwater remediation
- Industrial Wastewater Pretreatment
- Hazardous waste stabilization
- Storm water modelling
- Vehicle Emission Particle monitoring and Analysis
- Wetland Assessment, GIS
- Material Science Technologies
- Water, soil and air quality sampling and monitoring

EXPERIENCE HIGHLIGHTS

LEHIGH UNIVERSITY, Bethlehem, PA, 2013 - Present

Research Assistant

Completed research on novel water-based chemicals, and premature failure mechanisms of the DPF regeneration process. Hazardous waste stabilization development through cooperate with Materials Solution Service, llc. Research to in situ synthesis of SiC nanowire and characterize the thermos chemical resistance of the SiC nanowire as a potential substitute of cordierite for DPFs.

Key Accomplishments:

- Developed novel water-based chemicals based on Surface Chemistry, as well as novel surfactants and wetting agents to regenerate DPF, DOC, SCR to remove embedded soot and metallic ash to reduce engine backpressure.

www.manaraa.com

- Completed research to understand underlying DPF cordierite substrate premature failure mechanisms with material science technologies. Research included fouling mechanism of Pinholing, sintering and cracking, and the simulation of the thermos-fouling procedure.
- Completed research to develop highly efficiency carbon black adsorbents to remove heavy metals including Cu, Cd and Cr from industrial wastewater.
- Development of hazardous waste stabilization method by cement.

HUNSICKER EMISSION SERVICE, Allentown, PA, 2013 - 2017

Consultant

Consulted on engineering design projects for industrial wastewater pretreatment and diesel engine exhaust solutions.

Key Accomplishments:

- Designed novel Diesel Particulate Filter (DPF) regeneration technologies through a government funded project between Lehigh University and Hunsicker Emission Services.
- Developed a solution to recover high performance carbon black from the DPF process and remove heavy metals and natural organic matters.
- Monitoring the aerosol particle size and chemical compositions from Commercial Vehicle Emissions.
- Designed and tested an industrial wastewater pretreatment process to meet the Allentown Authority industrial wastewater discharge standards; reduced high concentration of COD and toxicity utilizing an Advanced Oxidation Process and removed heavy metal with activated carbon.

ENTERPRISE SYSTEM CENTER – LEHIGH UNIVERSITY, Bethlehem, PA, 2013 – 2014

Project Investigator

- Assisted local small businesses **Hunsicker Emission Services, LLC** with preparation for Beta test evaluation of the Diesel Particulate Filter regeneration process. Led weekly group meetings with industrial cooperator to share information and results.

Key Accomplishments:

- Prepared and presented a report on the findings to local business owners.

Additional experience as a Teaching Assistant at Lehigh University for multiple science lab sections.

www.manaraa.com

STREAM WATER QUALITY MONITORING, GOVERNMENT PROJECT, China, 2012 – 2013

Project Investigator

Monitoring stream water quality including BOD, oxidation reduction potential (ORP), dissolved oxygen (DO) with an one-year round in order to building up a database for local government. GIS is used.

EDUCATION

Ph.D. in Environmental Engineering | Lehigh University, Bethlehem, PA, 2017

Dissertation: Diesel Particulate Filters: Understanding Failure, Advancing Regeneration Technologies, and Development of Advanced Porous Ceramics

Master of Science in Environmental Engineering | Lehigh University, Bethlehem, PA, 2015

Bachelor of Science in Environmental Engineering | Southwest University, China, 2013

Publications:

1. **Kun Yang,** John Fox, Robert Hunsicker. Interaction of Fe, Na and K with porous cordierite at elevated temperature. *Journal of Material science*，*DOI: 10.1007/s10853-016-0665-2.*

2. **Kun Yang,** John Fox, Robert Hunsicker. Interaction between Ca, Zn and porous cordierite substrate at elevated temperatures. *Journal of Porous Materials*, *doi:10.1007/s10934-017-0458-2*
3. **Kun YANG**, John Fox, Robert Hunsicker. Diesel Particulate Filter (DPF) Failure due to Pinholes, Melting and Cracking. *Emission control science and technology*, 2016,4. ***DOI:*** *10.1007/s40825-016-0036-0*

4. **Kun Yang,** John Fox. Adsorption of humic acid by acid modified Granular Activated Carbon (GAC) and Powder Activated Carbon (PAC). ***EEENG-4090R1*** *DOI.*: 10.1061/(ASCE)EE.1943-7870.0001390. *Journal of Environmental Engineering-ASCE.*
5. **Kun Yang,** John Fox. DPF soot as an adsorbent for Cu(II), Cd(II) and Cr(VI) compared with commercial activated carbon. DOI.: 10.1007/s11356-017-1122-8 ESPR-D-17-04070.1 Environmental Science and Pollution Research.

www.manaraa.com

6. **Kun Yang,** John Fox. In-situ growth of SiC nanowire matrix (SCNWs) by organic precursor-guar gum and silicon powder. Materials & Design, (in preparation).

Presentations:

1. **Kun Yang.** Removal of Oil and Cr(VI) by using modified pectin flocculants. 246th ACS National meeting in Indianapolis, US. Division of Environmental Chemistry (Oral Presentation).
2. **Kun Yang.** (Oral Presentation) Diesel Particulate Filters: Understanding Thermal Chemical Conditions Lead to Early Failures. the 41th International Conference & Expo on Advanced Ceramics, Florida, US. Division of Mechanical Behavior and Performance of Ceramics & Composites.
3. **Kun Yang**. (Oral presentation). Diesel particulate filters: Interaction between Lube Ash and Cordierite Substrate, which Leads to the DPF Premature Failure. Materials Science & Technology 17, Pittsburg, PA. Division of Synthesis, Characterization, Properties and Applications of Functional Porous Materials: Porous Material Applications in Environmental and Sustainable Fields.

CERTIFICATIONS

Engineering in training (EIT), New Hampshire Board No. 6749

AFFILIATIONS

American Chemistry Society (ACS)
American Society of Civil and Engineering (ASCE)
American Ceramic Society (ACerS)

www.manaraa.com